# ResearchOnline@JCU



This file is part of the following work:

Bathgate, Jonathan Stacy (2005) *Extensions to the COSRAD HF ocean surface* radar: extraction of swell wave parameters. PhD Thesis, James Cook University.

Access to this file is available from:

https://doi.org/10.25903/npt0%2De082

Copyright © 2005 Jonathan Stacy Bathgate

The author has certified to JCU that they have made a reasonable effort to gain permission and acknowledge the owners of any third party copyright material included in this document. If you believe that this is not the case, please email <a href="mailto:researchonline@jcu.edu.au">researchonline@jcu.edu.au</a>

# Extraction of Swell Wave Parameters

Thesis submitted by

Jonathan Stacy BATHGATE BSc(Hons)

in March 2005

for the degree of Doctor of Philosophy
in the School of Mathematical and Physical Sciences
James Cook University
North Queensland

# STATEMENT OF ACCESS

I, the undersigned, author of this work, understand that James Cook this thesis available for use within the University Library and, via	-
Theses network, for use elsewhere.  I understand that, as an unpublished work, a thesis has significant	nt protection under the
Copyright Act and;	
I do not wish to place any further restriction on access to this work.	
Signature E	Date

# STATEMENT OF SOURCES

# **DECLARATION**

i deciare that this thesis is my own work and	nas not been	submitted in any	y form for
another degree or diploma at any university	or other institu	ution tertiary of	education.
Information derived from the published or	unpublished v	work of others	has been
acknowledged in the text and a list of references	is given.		
Signature		Date	

# **ELECTRONIC COPY**

submitted, within the limits of the technology available.	

#### STATEMENT OF CONTRIBUTIONS

Stipend support: ARC Industry Linkage (C00002491) with Telstra Applied Technology.

Supervision: Professor Mal Heron

Editorial assistance: Professor Mal Heron and Arnstein Prytz

Research assistance: Mal Heron, Arnstein Prytz, Ray Casey and Scott Heron

Use of Infrastructure external to JCU: Kingscliff Coast Guard facilities, Victorian National Parks.

Access to data: Queensland Beach Protection Authority and Tweed River Entrance Sand

By-passing Project (TRESBP) for access to the directional wave buoy

data. Victoria Channels Authority (VCA) and Port of Melbourne

Corporation for access to directional wave buoy data.

The innovative development of the automated swell extraction algorithm relies on the frequency modulation of the radar echo by swell waves (Chapter 5 and 6). This technique is unique to this thesis and publications arising from this thesis.

#### **Publications arising from this thesis:**

- M. L. Heron, A. Prytz and J. S. Bathgate, 2001. Currents off Tweed Heads Monitored by Coastal Ocean Surface Radar. *Coasts and Ports 2001, The Institution of Engineers, Australia, Barton*, ACT:49-54.
- J. S. Bathgate, M. L. Heron and A. Prytz, 2003. Swell Wave Direction off Tweed Heads Monitored by HF Ocean Surface Radar. *Coasts and Ports Australasian Conference* 2003, Paper No. 8.
- J. S. Bathgate, M. L. Heron and A. Prytz, 2004. A Method of Swell Wave Parameter Extraction from HF Ocean Surface Radar Spectra. (*In Review*) *IEEE Journal of Oceanographic Engineering*.
- J. S. Bathgate and M. L. Heron, 2005. Swell Waves Monitored by HF Ocean Surface Radar at Tweed Heads and Bass Strait. 17<sup>th</sup> Australasian Coastal and Ocean Engineering Conference: 191-196.
- J. S. Bathgate and M. L. Heron, 2005. Swell data measured by HF radar in Bass Strait (*In Preparation*)
- J. S. Bathgate and M. L. Heron, 2005. Measurement of wind direction and evaluation of the spreading function at Tweed Heads. (*In Preparation*)

# Acknowledgements

I gratefully acknowledge the guidance and assistance of my supervisor Prof. Mal Heron throughout the degree. A special thanks to Arnstein Prytz for his continued help and patience with my frequent visits and interruptions.

Thanks also to Ray Casey and Scott Heron for their help during the Tweed Heads deployment of the radar.

For providing me with field work and tutoring experience during my years at JCU I again thank Mal but also Peter Ridd and Russel Jaycock. These occasions often provided a pleasant break from my own work, particularly during writing, and were valuable experiences that will surely come in useful.

I would also like to thank my parents for their support throughout my student life at university. This includes the early morning breakfasts to get me to maths lectures on time and for providing me with somewhere to live while I finished this thesis.

Lastly, it would be remiss of me not to acknowledge Bec's patience and encouragement during the writing of this thesis and making my life outside the physics department far more enjoyable. Maybe one day I'll be able to return the favour.

#### Abstract

Routine extraction of ocean surface information from HF radar spectra has, to this point, been predominantly limited to surface currents and wind parameters which rely on the analysis of the first-order spectral lines. Recently, wind wave parameters are also being supplied in a routine manner. Their calculation involves the ratio of first and second-order spectral energies to produce significant wave heights and direction. Parameter extraction from portions of the long ocean wave spectrum has proven difficult. The derivation of the second-order cross-section by Barrick (1972b) led to solutions for the extraction of swell wave information (Lipa and Barrick, 1980). However, this still did not lead to a reliable supply of long wave information. Only recently has there been some success with full directional spectrum analysis under certain conditions, (Wyatt, 1999). The solutions provided by Lipa and Barrick (1980) are evaluated in this thesis on data collected by the coastal ocean surface radar (COSRAD). The results proved unsatisfactory due to the high sensitivity required by the solutions.

To develop an original method of extraction for swell wave information, two sets of data were acquired using a pair of COSRAD systems overlooking Tweed Heads and Bass Strait in 2001. At Bass Strait the radar was configured to cover a sweep (approximately 60 degrees) every 60 minutes with spatial resolution of the order of 3km. Spectral preprocessing procedures included frequency and power level normalization prior to incoherent averaging. We average 8 adjacent pixels over a 2-hour period to improve the signal to noise ratio and aid in the identification and manipulation of the second-order swell peaks that lie about the strong first-order Bragg lines in the spectrum.

A new method for the extraction of swell wave parameters from HF radar spectra is presented along with results and comparisons to a directional wave buoy which lies in the coverage zone. The method of extraction of the parameters, period, direction and height, relies on a frequency modulation approach that describes the hydrodynamic interaction of

the swell waves with the resonant, shorter, Bragg waves. The analysis process minimises the electromagnetic second-order interaction and a simulation model was used to validate the approach. This simplified method provides a fast means of examining swell conditions over large areas of the ocean surface. The automated algorithm returned results that compared favourably with the wave buoy at both deployment locations. The best results were achieved during periods of swell activity that exceeded 0.3 m in height, below this value the second-order sidebands became noisy and unreliable. During these periods the swell height was measured to within  $\pm 0.1$  m of the wave buoy. The swell direction was measured to accuracies of  $\pm 10$  degrees and the swell period to  $\pm 1$  second. The results support the use of the COSRAD HF ocean surface radar for mapping swell in the near-shore zone and shows potential for the routine extraction of parameters in near real-time.

A routine for the extraction of wind direction was also developed and tested on data collected during the deployment at Tweed Heads. A comparison of pairs methodology for the resolution of the inherent ambiguity in wind direction about the radar beam is presented. The determination of an appropriate spreading parameter is demonstrated, as carried out previously by Heron and Prytz (2002), to refine the directional results in comparison with wind wave data from the wave buoy.

# **Table of Contents**

Chapter 1: Introduction, Aims and Objectives		1
1.1	Introduction	1
1.2	Aims and Objectives	2
Chapter 2: R	Radio Oceanography – Theory and Previous Work	5
2.1	Evolution of HF Radar	5
2.2	HF Radar – Technical Information	11
	2.2.1 Ground Wave Attenuation	12
	2.2.2 Spatial Resolution	12
2.3	Data Collection and COSRAD Specifications	14
	2.3.1 The Tweed Heads Deployment	15
	2.3.2 The Bass Strait Deployment	19
Chapter 3: P	Pre-processing COSRAD Spectra	22
3.1	Frequency Normalization	22
3.2	Power Level Normalization	23
3.3	Incoherent Averaging of Doppler Spectra	26
	3.3.1 Spatial Averaging	26
	3.3.2 Temporal Averaging	27
3.4	The Noise Floor	29
3.5	Discussion	30

Chapter 4: Mo	ethods of Extracting Swell Wave Parameters	32
4.1	Peak Finding Algorithm	33
	4.1.1 Peak Identification	35
	4.1.2 Peak Definition	38
4.2	Processing of Swell Peak Positions	39
	4.2.1 Weighted Mean and Frequency Limits	40
4.3	Applying Second-Order Solutions	42
	4.3.1 Direction of Swell Wave Propagation	43
4.4	Discussion	47
Chapter 5: Sw	vell Wave Parameter Extraction Algorithm	49
5.1	Frequency Modulation of the Radar Echo	49
5.2	Peak Power Ratios	54
5.3	Peak Area Ratios	58
5.4	Automated Fitting Routine for Swell Height and Direction	60
	5.4.1 Directional Fitting	62
	5.4.2 Vertical Calibration	64
5.5	Discussion	66
Chapter 6: Te	sting and Results of the Automated Swell Algorithm	70
6.1	Wave Buoy Analysis at Tweed Heads	71
6.2	Automated Algorithm Results for Swell Height, Direction	76
	and Period at Tweed Heads	
	6.2.1 Tallebudgera Station	76

	6.2.2 Kingscliff Station	85
6.3	Automated Algorithm Results for Swell Height, Direction	86
	and Period at Bass Strait	
	6.3.1 Test Case: Portsea Station – July 18, 2001	89
6.4	Range Limits	99
	6.4.1 Portsea Range Limit	99
6.5	Discussion	101
Chapter 7: F	urther Extensions to the HF COSRAD System	104
7.1	Wind Direction Algorithm	105
7.2	Algorithm Validation	108
7.3	Discussion	116
Chapter 8: D	Discussion and Conclusions	118
0.1	W. M. M. Martin and M. H. D. L.	110
8.1	Wave Measurement with HF Radar	119
8.2	The Automated Swell Wave Algorithm	122
	8.2.1 Radar Configuration	122
	8.2.2 Limitations	123
8.3	Future Work	127
8.4	Conclusions	128
References		130

#### **List of Tables**

- Table 1: Swell peak frequency bands.
- Table 2: Swell wave classification table Australian Bureau of Meteorology
- Table 3: Comparison of pairs for resolution of wind direction ambiguity

# **List of Figures**

- Figure 1: HF radar Doppler spectrum
- Figure 2: Tweed Heads location map
- Figure 3: Tweed River Entrance Sand By-pass system outlet map
- Figure 4: COSRAD coverage at Tweed Heads
- Figure 5: Bass Strait location map
- Figure 6: COSRAD coverage at Bass Strait
- Figure 7: Signal attenuation with range
- Figure 8: Spatial incoherent averaging of Doppler spectra
- Figure 9: Temporal incoherent averaging of Doppler spectra
- Figure 10: Doppler spectrum noise floor
- Figure 11: Second-order swell peaks in the Doppler spectrum
- Figure 12: (a) Bragg peak selection criterion
  - (b) Bifurcated Bragg peak selection criterion
- Figure 13: Swell peak selection criterion
- Figure 14: Bifurcated swell peaks
- Figure 15: Weighted mean adjustment for swell peak positions
- Figure 16: Ambiguity in swell direction calculation
- Figure 17: Trends of swell direction across a radar sweep
- Figure 18: Dependence of swell direction on  $q_{
  m deg}$

- Figure 19: Dependence of  $\Delta \mathbf{w}^{+}$  and  $\Delta \mathbf{w}^{-}$  on beam direction.
- Figure 20: Schematic of Bragg waves modulated in frequency by swell waves
- Figure 21: Relationship between radar beam direction and swell propagation direction
- Figure 22: Two-scale model of Doppler spectrum
- Figure 23:  $R_{swell}$  curve from frequency modulation two-scale model
- Figure 24: Average swell peak ratio ( $R_{swell}$ ) calculation
- Figure 25: (a)  $R_{swell}$  ratios from positive swell and Bragg peaks only
  - (b)  $R_{swell}$  ratios from the dominant side of Doppler spectrum
- Figure 26: Area estimation of Bragg and swell peaks
- Figure 27: Variation in  $R_{swell}$  curve with swell amplitude
- Figure 28: Differentiated  $R_{swell}$  curve
- Figure 29: (a) Calculation of the gradient  $(m_r)$  of radar  $R_{swell}$  values with outliers
  - (b) Calculation of the gradient  $(m_r)$  of radar  $R_{swell}$  values with outliers removed
- Figure 30: Model spectra demonstrating the contribution of the EM component on sideband asymmetry
- Figure 31: Comparison of  $R_{swell}$  with EM component removed from calculations of spectra
- Figure 32: Wave buoy spectra from Tweed Heads Waverider Buoy
- Figure 33: Swell height record for deployment period from Tweed Heads wave buoy
- Figure 34: Swell period record for deployment period from Tweed Heads wave buoy
- Figure 35: Swell direction record for deployment period from Tweed Heads wave buoy
- Figure 36:  $R_{swell}$  values from radar data fitted to the stylised curve in direction and height for March 6, 2001
- Figure 37: (a) Swell direction for March 6, 2001 validated by wave buoy data
  - (b) Calibrated swell height for March 6, 2001 validated by wave buoy data
  - (c) Swell period for March 6, 2001 validated by wave buoy data
- Figure 38: Swell height, direction and period (Tallebudgera station) as measured using the swell algorithm for the deployment period validated by wave buoy data
- Figure 39: Swell height record for deployment period from the Bass Strait wave buoy

- Figure 40: Swell period record for deployment period from the Bass Strait wave buoy
- Figure 41: Swell direction record for deployment period from the Bass Strait wave buoy
- Figure 42: (a) Test case July 18, 200. Validated results for swell height at Bass Strait (b) Test case July 18, 200. Validated results for swell direction at Bass Strait
- Figure 43: Banding of results for swell direction at Portsea and Ocean Grove compared with wave buoy
- Figure 44: Comparison of the error in slope of radar data and the wave buoy swell height record
- Figure 45: Comparison of swell parameters derived from Portsea and wave buoy data
- Figure 46: Comparison of swell parameters derived from Ocean Grove and wave buoy data
- Figure 47: Swell direction with the wave buoy with error cut-off value employed
- Figure 48: Swell height with the wave buoy with error cut-off value employed
- Figure 49: Rank ordered error of fit lines with increasing range
- Figure 50: Schematic showing the geometry of the adjacent radar system configuration
- Figure 51: Diagram showing the wind direction ambiguity about the beam direction
- Figure 52: Spherical geometry calculation for pixel positioning
- Figure 53: Wind direction map at Tweed Heads on March 5, 2001
- Figure 54: Wind speed measured at Coolangatta Airport for the deployment period
- Figure 55: (a) Eastward component of wind speed at Coolangatta Airport
  - (b) Northward component of wind speed at Coolangatta Airport
- Figure 56: Synoptic weather charts (Australian Bureau of Meteorology) for March 5, 6 and 7, 2001
- Figure 57: Wind wave direction measured by the wave buoy at Tweed Heads
- Figure 58: Wind direction validated by wind wave data with S=2
- Figure 59: standard deviations of wind direction for S = 0.5, 1, 2 and 3
- Figure 60: Wind direction validated by wind wave data with S=1.4
- Figure 61: Map of possible configuration for 3 adjacent radar systems at Bass Strait
- Figure 62: Map of possible configuration for 3 adjacent radar systems at Tweed Heads

# Chapter1: Introduction, Aims and Objectives

#### 1.1 Introduction

Recent advances in remote sensing technology have led to expanding applications in environmental monitoring, particularly in the near shore coastal zone. These advances include the use of High-Frequency (HF – generally includes frequencies between 3 and 30 MHz) radar in many areas of the remote sensing field. The HF radar technology can now be used for purposes as varied as homeland security to environmental coastal protection. The use of long range HF radar for defence purposes dates back to the Second World War however its role today is far more diverse. It is used to combat smuggling, drug trafficking, track illegal fishing vessels and to coordinate search and rescue operations, (Sevgi et al., 2001). When these systems are operational they encounter interference from various environmental and anthropogenic sources. The main environmental source is commonly termed ocean "clutter". For many applications this ocean clutter is discarded in search of a better signal to noise ratio, however, for oceanographers this ocean clutter can provide information on the state of the ocean surface. Current environmental applications of HF radar are mainly found in the areas of coastal management but occasionally find uses in the fisheries industry and tracing the progress of surface borne pollutants (Barrick, 1977). These kinds of functions are becoming more common as awareness and confidence in the technology increases. For a country like Australia which possesses the longest coastline of any country and has all of its major cities located on the coast, a tool such as HF radar can be very valuable.

An oceanographic interest in HF radar technology originated when Crombie, (1955), observed a structure to this background noise, or clutter, that he correctly related to ocean surface waves. He noticed the relationship between the transmitted electromagnetic wave and the ocean surface could be exploited to remotely provide information on sea state. HF radar systems have the capability of collecting data over a large area and therefore provide a much higher data density than can be achieved by using moored current meters and directional wave buoys. Since Crombie made his discovery, HF radar has been used to map short wavelength ocean waves and

amplitudes, with applications in coastal management and ship guidance. However, oceanographers are increasingly interested in long period ocean waves that have a greater impact on shipping and contribute to the impact of the ocean on the coastline. Long period ocean waves such as swell can increase the risks involved with the entry of large ocean going vessels into certain harbours and are also a concern when the ship is moored in port (van der Molen *et al.*, 2003). Possible links between swell waves and the generation of infra gravity waves which can prove devastating to ports and coastlines make their monitoring even more desirable (Oltman-Shay and Hathaway, 1989).

As radar technology developed the higher order interaction between the transmitted electromagnetic wave and the longer period ocean waves became accessible to analysis. Barrick (1971) derived a theorem to describe this interaction and proved that it is, in fact, produced by second order wave-wave interaction. Given this theory, oceanographers became enthusiastic about using HF radar to measure sea state. However, Hasselmann (1971) showed that although Barrick's theorem would provide estimates of dominant wave period and height, it would not yield any directional information from the second-order spectrum. This proved to be a complex problem and forced many oceanographers to resign themselves to the fact that the only directionality being extracted from an HF Doppler spectrum would be for shorter wavelengths. Lipa and Barrick (1977, 1986) examined the second-order spectrum closely and found a link between the position of the resonant swell peaks and the dominant direction of the swell waves. This model for the extraction of parameters from the long period wave spectrum remains unvalidated.

# 1.2 Aims and Objectives

This project is aimed primarily at developing a model for swell extraction using two large, independent data sets. The data was collected during February and March, 2001, from Tweed Heads and the Bass Strait during July, using the HF COSRAD system (Coastal Ocean Surface Radar) developed at James Cook University. Firstly an adaptation of the solutions for second-order extraction of swell waves from Lipa and Barrick (1977) will be developed for use with data collected by the COSRAD system.

Once a robust routine algorithm for the extraction of swell parameters has been developed, it will be integrated with COSRAD's current capabilities of measuring surface currents and significant wave heights (wind-wave heights). The system has the potential in the future to provide estimates of sediment resuspension and transport becoming an important tool for remotely sensing the ocean surface in the near-shore zone. Given an energetic environment and assuming a well-mixed water column, the surface currents can be extrapolated to the sea floor using a logarithmic function. This is where the main contribution for sediment resuspension occurs. Swell data and significant wave heights also contribute to benthic water velocities and can be extrapolated to the sea floor in a similar fashion. Given all these parameters and their interaction with sediment, estimates can be made as to the degree of resuspension occurring.

The measurement of wind fields are another area that lends itself to monitoring by HF radar. Short period waves, which are measured as first-order interaction using HF radar, quickly align themselves with the wind direction. Measurement of wind direction has also been theoretically established by Heron and Rose (1986). The method used in that study relies on the analysis of the first-order peaks for calculating the wind direction and the wind-wave peaks for the calculation of the wind speed. The development of a routine algorithm for its extraction would provide a valuable extension to the COSRAD Radar system.

#### To summarize the aims of this thesis:

- Collect two independent sets of data from deployments of James Cook University's HF radar system COSRAD. The deployments are to be conducted at Tweed Heads, and Bass Straight,
- 2. Develop a spectral processing routine specifically to aid in the extraction of swell wave parameters,
- 3. Attempt to adapt mathematical solutions proposed by Barrick (1972b) and Lipa and Barrick (1980) for the calculation of swell direction, height and period from HF radar spectra,

- 4. If necessary, develop an alternative method for the extraction of swell wave parameters,
- 5. Present swell wave parameters as measured by the algorithm during the Tweed Heads and Bass Strait deployments and validate using data from directional wave buoys present at each location.
- 6. Other improvements to the COSRAD system such as resolving wind field measurements.

On completion of this project the COSRAD system will be able to extract surface currents, significant wave heights, wind direction, as well as swell period, direction and amplitude. Such a complete set of data on such a large scale would be extremely valuable for use in a variety of coastal situations. Engineering projects, environmental monitoring and marine biological studies are just a few examples of possible applications.

# Chapter 2: Radio Oceanography – Theory and Previous Work

This thesis is concerned with remote monitoring of the sea surface with particular interest in advancements in measuring sea state. It is important to define sea state and a variety of oceanographic nomenclature prior to further discussion. Firstly, it is best to determine what portion of the ocean wave spectrum with which we are concerned. Ocean surface waves are classified in to numerous categories, most commonly, by the frequency (the inverse of a wave's period) of the wave. The largest category is that of wind generated gravity waves which spans wave periods between 1 and 30 seconds (Kinsman, 1965). Gravity waves are a group containing all waves that are measurable using HF radio techniques. HF is commonly defined as transmitted wavelengths between 10 and 100 m which targets ocean surface waves between 5 and 50 m in length. This relationship will be described later. As defined by Phillips (1977), the term gravity wave refers to all waves whose chief restoring force is that of gravity. This is the case for all waves with a wavelength greater than 1.7 cm; below this the main restoring force is that of surface tension and these waves are classified as capillary waves. The most important of these, for the measurement of sea state, are swell waves. Kinsman divides gravity waves in to two groups, sea and swell. Sea, describes waves that are being worked on by the wind that raised them and swell describes waves that have escaped the influence of the generating wind. Separating the sea and swell by their period results in some overlap. Importantly all wave conditions discussed throughout this are assumed to be deep-water waves. This infers that the ocean floor has no effect on the propagation of the wave. This is considered to be true when the water depth is greater than half the length of the observed wave. Therefore, all waves discussed here to describe sea state are deep-water gravity waves.

### 2.1 Evolution of HF Radar

Advancements in radio technology during the Second World War provided the instrumentation necessary to discover an interaction of radio waves, at high-frequency

(HF), with the ocean surface. The radar system was being used at the time as an early warning for approaching enemy aircraft and was most commonly positioned on the coastline looking out to sea. Before long it was noticed that the ocean surface was scattering the incident radio signal often masking the target being tracked. The importance of the system as a defensive tool was greatly appreciated and therefore this decreased functionality was a considerable concern. However, the relationship between the ocean surface and the scattered electromagnetic waves was not sufficiently understood until well after the war had ended. Crombie (1955) made the discovery that began the new field of radio oceanography. In the ensuing decades, radio oceanography developed rapidly to a point where today certain aspects of the sea surface are monitored routinely by HF radar systems worldwide.

To make his discovery Crombie examined a Doppler spectrum of the backscattered sea echo with the intention of focussing on the background echo, or "clutter", rather than processing the spectrum with the aim of enhancing a particular target's intensity. By doing this Crombie observed that the received Doppler spectrum consisted of two discrete spectral peaks situated at an equal distance above and below the radar carrier frequency (Figure 1). He related this to two discrete targets that must be moving with a constant velocity, of which the radial component could be calculated using the Doppler equation,

$$v_r = \frac{\mathbf{I}\Delta f}{2} \tag{1}$$

where  $\lambda$  is the radar wavelength. With this piece of information Crombie then inferred these two signals could be the result of ocean waves with components moving radially towards and away from the radar. It is known from the gravity-wave dispersion relation,

$$v = \sqrt{\frac{g}{2\mathbf{p}}} L \tag{2}$$

This shows that sea waves of a given wavelength, L, will move at a certain velocity, v, where g is the acceleration due to gravity. Given this relationship, it was then possible to calculate the ocean wavelength, L, which was the target producing these two spikes in the spectrum. This calculation gave a value for L of exactly half that of the transmitted electromagnetic wavelength. Crombie considered that the sea waves act as a

diffraction grating, i.e. a large signal is received when radio waves, of wavelength  $I_o$ , reflect off sea waves with wavelength  $I_w$ , where

$$I_{w} = \frac{I_{o}}{2\cos(\mathbf{q})} \tag{3}$$

and q is the grazing angle of the incident beam on the sea surface. The angle, q, is usually considered to be zero as the radar is at or is very close to sea level. Hence, this simplifies to  $I_w = I_o/2$ . This resonance phenomenon is recognised in other physical situations as "Bragg scatter" and was discovered by W. L. Bragg in 1912. This theory relies on the fact that there are sea waves of this particular length present in the ocean spectrum at all times. However, this is not an issue because the Fourier decomposition of any random area of the sea surface will contain wave energy at or near the required wavelength to support Bragg scatter.

The first-order peaks, Bragg peaks, in the spectrum are easily identifiable, as shown in Figure 1, and provide the necessary connection between the ocean surface and the transmitted radio wave to form the basis for remotely sensing sea state. The spectrum in Figure 1 was recovered by the COSRAD system. The Bragg peaks are located at a frequency of  $\pm 0.56$  Hz determined by the operating frequency of the radar being at 30 MHz. This spectrum represents a single pixel in the sweep, not an average, and still the first-order peaks are clear.

Experimental evidence supporting Crombie's discovery appeared over following years, with the next breakthrough being made in 1966, (Wait, 1966) when it was shown that the intensity of the backscattered signal produced by the resonant ocean waves is related to the height of the wave-train. This discovery encouraged other oceanographers to dedicate time to this area of research, as it was now beginning to remotely provide valuable physical information on the sea surface and further advances in this area looked promising. At this stage it was only possible to examine the short wavelengths due to the radar transmission frequencies that were being used. At HF, between 3-30 MHz, the radar wavelengths interact with resonant Bragg waves of the order of 50 m to 5 m long. These waves are considered short in terms of measuring sea-state. In order to measure long wavelengths by first-order interaction, the radar would be required to

transmit at medium frequency (MF). Transmission at such frequencies requires long antennae arrays to generate such long wavelengths and also, frequencies in this range of the spectrum are widely used for other purposes and therefore anthropogenic interference is common.

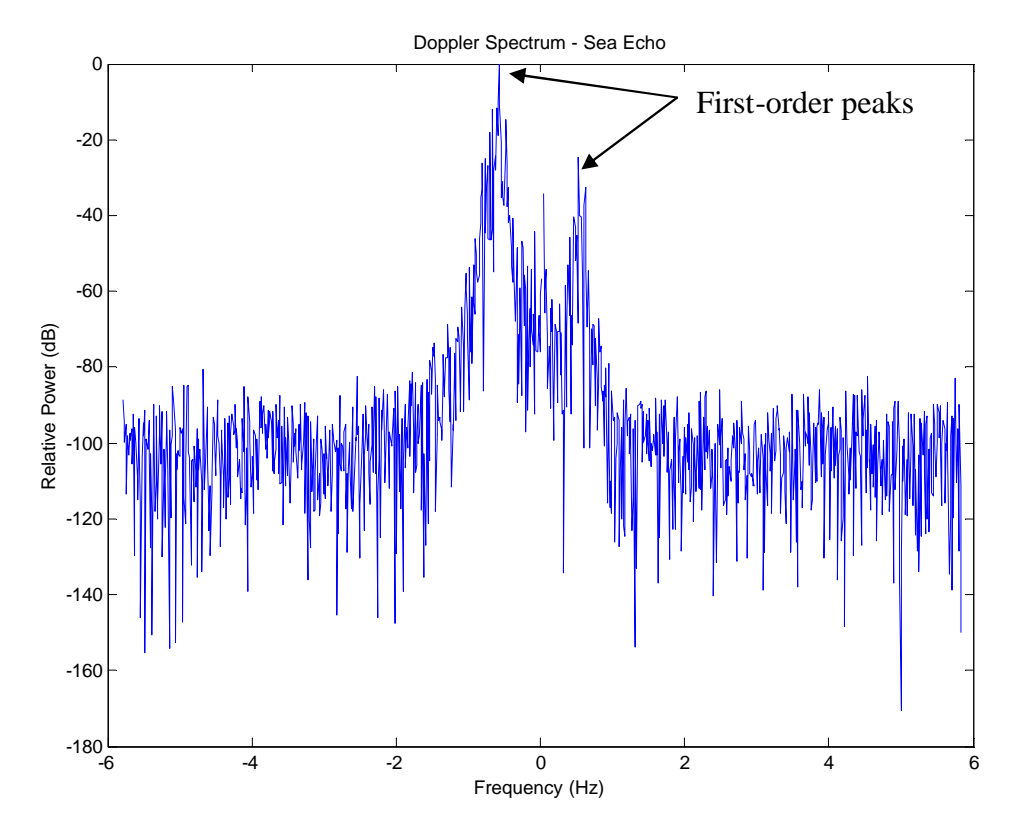


Figure 1: Typical HF Doppler spectrum displaying the two discrete first-order Bragg peaks at  $\pm 0.56$ Hz. Spectral processing is required to distinguish the second-order features.

Therefore, at this time in the development of radio oceanography, scientists had to be content with the extraction of short wave information, such as surface currents (Stewart and Joy, 1974).

Calculating surface current velocities requires the calculation of the total Doppler shift  $f_D$ . The total Doppler shift is comprised of the Doppler shift due to the phase velocity

of the Bragg wave,  $f_B$ , and  $\Delta f$  which is the shift due to the bulk movement of surface water,

$$f_D = \pm f_R + \Delta f \tag{4}$$

Where

$$f_B = \pm \sqrt{\frac{gf_o}{\boldsymbol{p}c}} \tag{5}$$

and

$$\Delta f = -2f_0 \frac{v}{c} \tag{6}$$

 $f_0$  being the radar frequency, c is the speed of light and v is the magnitude of the surface current component parallel to the direction of the radar beam. The Doppler shift due to surface currents,  $\Delta f$ , can be found from the departure of the Bragg peaks from the Bragg frequency,  $f_B$ .  $\Delta f$  can be positive or negative in a particular spectrum depending upon the direction of shift in relation to  $f_B$ , to the left or right. This in turn allows for positive or negative values of v, which represent waves moving towards or away from the radar. In equation 6 the negative sign shows that we label components moving away from the radar as being positive. To resolve directionality of the surface currents and their true velocity, two radar stations are required to operate simultaneously with approximately orthogonally intersecting beams.

This alone was a great discovery and asset to the field of oceanographic remote sensing however, being constrained to the analysis of short ocean waves saw a brief lull in development in the field. The analysis of long ocean waves is crucial if the purpose of the radar system is to measure sea-state. The shipping industry requires a reliable description of the sea-state in order to regulate the safety of its vessels, particularly in a coastal environment. Barnum (1971) sparked another flurry of developments when he realised that the noise floor in the spectrum surrounding the first-order was much higher than expected from atmospheric interference or system-generated noise (Barrick 1972b). He confirmed this by simply examining the system noise spectrum independently of the ocean scatter and also comparing the ocean spectrum to scatter from the land. This idea was taken further by Hasselmann (1971) who suggested that this continuum surrounding the first-order spectrum was due to a second-order

interaction with the ocean and a possible measure of sea-state. However, it was Barrick (1972a, b) that discovered the continuum surrounding the first-order spectrum varies in shape and amplitude with sea-state and radar frequency. Therefore by examining the second-order peaks in the spectrum, their strength and relative positions, information on sea-state can be extracted. The explanation for this higher-order interaction lies in the extrapolation of electromagnetic and hydrodynamic equations to reveal second-order terms. The second-order term resulting from the electromagnetic interaction is shown below:

$$\Gamma_{EM} = \frac{1}{2} \left[ \frac{\left(\tilde{k} \cdot \tilde{k}_{o}\right) \left(\tilde{k}' \cdot \tilde{k}_{o}\right) / k_{o}^{2} - 2\tilde{k} \cdot \tilde{k}'}{\left(\tilde{k} \cdot \tilde{k}'\right)^{1/2} + k_{o}\Delta} \right]$$
(7)

where  $k_0$  is the radar wave number, k' is the short wavelength wind wave number and k is the swell wave number. These wave numbers adhere to the relationship:  $k+k'=-2k_0$ .  $\Delta$  is the normalised impedance of the sea surface (Barrick, 1971). The hydrodynamic contribution to the second order spectrum is:

$$\Gamma_{H} = -\frac{i}{2} \left[ k + k' - \frac{\left( kk' - \tilde{k} \cdot \tilde{k}' \right)}{mm' \left( kk' \right)^{1/2}} \left( \frac{\mathbf{w}^{2} + \mathbf{w}_{B}^{2}}{\mathbf{w}^{2} - \mathbf{w}_{B}^{2}} \right) \right]$$
(8)

where  $i=\sqrt{-1}$ ,  $m,m'=\pm 1$  represents the four combinations of second-order peaks surrounding the first-order Bragg lines.  $\boldsymbol{w}$  is the second-order peak frequency and  $\omega_B$  is the Bragg frequency. The summation of the contributions due to electromagnetic and hydrodynamic effects forms a coupling coefficient

$$\Gamma_T = \Gamma_{EM} + \Gamma_H \tag{9}$$

that is sensitive to second-order wave directionality.

Even though Barrick (1972b) was able to derive this relationship and support Hasselmann's theory that sea state could be deduced from HF sea scatter by the strength and position of second-order peaks, he could not provide confirmation due to the lack of quality measurements available at the time. This would quickly change as technology was soon able to provide high quality sea-echo backscatter spectra and this relationship was proven experimentally.

Since it had been shown that longer waves could indeed be identified by HF radar, it was necessary to develop ways to extract the parameters of these waves, such as, wave height, period and direction of propagation. Hasselmann (1971) provided the means to extract period and wave height but also concluded that it would render the spectrum insensitive to directional information. This remained the case for several years until Lipa (1978) was able to extract wind wave directions from the second-order echo. It was shown that the second-order peaks vary in position and in amplitude with changing direction. The amplitudes are dependant on the coupling coefficient which is known to vary with direction. With this solution to the directional problem now in hand, it was possible to develop a series of expressions to describe sea state from HF radar sea echoes.

HF radar as a reliable remote monitoring tool is gaining acceptance throughout the oceanographic community as repeated validation with conventional measurement devices occurs (Prandle and Wyatt, 1999). HF surface current measurements have reached the level of acceptance that many in the field are trying to achieve with wave measurements.

### 2.2 HF Radar – Technical Information

HF radars have now been used for many decades to monitor the ocean surface and with continuing technological advancements in design and computational processing they are becoming even more popular. There are two forms of radar transmission that are commonly employed for oceanographic purposes. These are known as skywave or ground-wave propagation. Skywave systems reflect the transmitted beam off the ionosphere in order to achieve large propagation ranges. Ground-wave propagation on the other hand is closely coupled to the sea surface in an attempt to minimise complicated ionospheric effects on the sea surface echo. Ground-wave propagation is maintained by polarising the electromagnetic wave in the vertical direction so that it follows the contours of the air-sea interface however, this mode of propagation severely reduces the working range of the radar (Heron *et al.*, 1985). This outline will

concentrate on ground-wave propagation properties; however, many of them are still applicable to some degree to skywave systems.

#### 2.2.1 Ground-Wave Attenuation

The working range of a radar system is dependant on various aspects, both environmental and anthropogenic. The transmitted electromagnetic wave is attenuated in its advancement to the target and again during its return to the receiver. An increase in the range from the radar to the target results in a decrease in the signal-to-noise ratio. The strength of the returned signal is dependant upon the scattering strength of the target, atmospheric noise and noise due to radio interference in the working frequency band (Gurgel *et al.*, 1999). With ground-wave propagation, sea surface conditions are as important a factor as atmospheric conditions. Attenuation over the sea surface is reliant upon the transmitted frequency and conductivity of the sea, where conductivity is a function of water temperature and salinity. High salinity levels allow greater ranges to be achieved at lower power levels.

Scattering strength is an important factor in the attenuation of the ground-wave but is not as straight forward a relationship as first thought. It sounds reasonable to assume that higher sea states would provide higher scattering strengths and this is the case at relatively close range. Stronger signals are received during times of large wave heights, however, it does not continue at intermediate ranges due to the higher losses incurred by the high level of scattering, out to the long ranges and back again (Barrick. 1971, Gurgel *et al.*, 1999).

# 2.2.2 Spatial Resolution

Spatial resolution consists of two dimensions, range and azimuth. Range resolution is dependant upon the transmit frequency and the method of transmission. The two main methods of transmission are by short pulses or by frequency modulated chirps (FMCW). Of course range resolution at VHF is very high but this also decreases the working range of the radar and thus a compromise must be reached. Towards the high end of the HF band working range is reasonable and radio interference can be overcome

by using a very narrow bandwidth for transmission. This, however, will decrease the range resolution of the system. The main advantage of using a pulse system is the simplified design required to run it. The FMCW method allows more flexibility in the alteration of transmission frequency and range resolution (Gurgel *et al.*, 1999).

Direction finding and beam forming are the main methods used for azimuthal resolution. The design of an array of antennas works by each antenna collecting the scattered sea echo from differing azimuthal directions. Each of these received traces is then superimposed to provide one complete signal with embedded directional information. The main advantage for systems employing direction finding is the small array sizes required. It compares the amplitudes and phases of the received signals from each antenna in order to determine the direction they were arriving from on a polar grid relative to the antenna. However, this method can only be used for first-order signals as the second-order is masked by these higher power returns. This method also is susceptible to problems if the assumption that the current field is homogeneous does not apply. The direction finding method will fail to recognise when the same Doppler shift has sources in different directions. The beam forming method doesn't rely on assumptions such as this but does require large antenna arrays in order to provide directional information. Beam forming employs the formation of a narrow beam that can be electronically steered over the required area of the sea surface. They generally can be steered up to a maximum of 45 degrees on either side of the bore sight. The antenna array is normally up to  $8\lambda$  in length, where  $\lambda$  is the electromagnetic wavelength. Optimal spacing between each antenna is  $\lambda/2$ . This system is also sensitive to secondorder sea echo directional information (Heron, 2005).

# 2.3 Data Collection and COSRAD Specifications

The James Cook University developed Coastal Ocean Surface Radar (COSRAD) was deployed on two occasions throughout 2001 as part of this project. On both occasions the radar was in situ for a period of one month, collecting data 24 hours a day. The first deployment began in late February with two COSRAD stations covering a portion of the sea surface off the coast of Tweed Heads. The second deployment of the system was during July, recording data of sea surface conditions at the entrance to Port Phillip Bay in Victoria. The setup of the radar at both stations during a single deployment is exactly the same apart from the look directions. Positioning of the radar is constrained by availability of suitable space to accommodate the antenna array with an uninterrupted view of the ocean. Other settings can be assigned to the system to suit the intended aims of the project. A typical set up of a COSRAD station transmits at a frequency of 30 MHz, (f), that essentially determines the length of the transmitted electromagnetic wave by I = c/f and therefore the length of the resonant ocean wave, which is defined as  $\lambda/2$  by Crombie (1955), where  $\lambda$  is the transmitted wavelength and c is the speed of light. Therefore for this COSRAD setup the transmitted wavelength is 10 m and the resonant ocean wavelength is 5 m. The antenna array consists of 8 elements, spaced half a transmitted wavelength apart. Therefore the complete array occupies an area of approximately 45 x 2.5 m<sup>2</sup>. The 8 elements form a beam of width,

$$\Delta \boldsymbol{q} \approx \arcsin\left[1/(2N_A)\right]$$
 (10)

where  $N_A$  is the number of elements in the array. This gives a beam width of about 7 degrees which is electronically steered to 17 different angular positions about the bore sight. It is important to note here that the 8 element antenna array used for both transmit and receive produces an effective beam width comparable to that of a wide angle transmit antenna and a 16 element receive antenna array which has the advantage of reducing the installation space requirements. However, with this configuration it is no possible to measure the backscatter spectra from all directions simultaneously. The azimuthal extent of coverage of each COSRAD station is approximately  $\pm 30$  degrees about the bore sight. Data is usually collected from 12 different ranges in each of the 17 sectors completing an entire sweep within 30 minutes. To meet these specifications the integration time for each pixel is set at 102.4 seconds. Noise levels are too high to retain workable spectra beyond this. The range resolution is determined by the width

of the transmitted radio-frequency pulse. A common antenna array is used to transmit and receive the frequency signal and therefore the width of the transmitted pulse becomes important. The signal is received by switching the array to receive during the quiet time to detect any scattered signals from the ocean surface. The range resolution for COSRAD during both deployments was set to 3 km using

$$\Delta r = \frac{1}{2}c\Delta t\tag{11}$$

to determine the pulse width,  $\Delta t$ . The maximum range of the system,  $R_{\rm max}$ , is a function of the time between pulses,  $T_P$ , and the pulse width,  $\Delta t$ , related by

$$R_{\text{max}} = \Delta r T_{P} / \Delta t \tag{12}$$

This maximum theoretical range is effectively shortened in practice by numerous factors including interference from land, the sensitivity of the receiver and the resulting signal to noise ratio.

# 2.3.1 The Tweed Heads Deployment

As mentioned above the first deployment was to monitor coastal ocean surface conditions off the coast of Tweed Heads for a period of one month. The deployment commenced on the 12<sup>th</sup> of February and concluded on the 15<sup>th</sup> of March. During this period the radar was in continuous operation, observing a variety of weather conditions including some storm activity and heavy rain. Figure 2 shows the two COSRAD stations located at Kingscliff (28°15.526' S, 153°34.923' E), to the south of the entrance to the Tweed River, and Tallebudgera (28°06.007' S, 153°27.661' E) to the north. The sites were selected for their coverage of a directional wave buoy run by the Queensland Beach Protection Authority (QBPA), the probability of observing strong swell conditions in the area during this time of year and interest in sediment transportation by means of surface currents and wave action in the vicinity of the Tweed River.

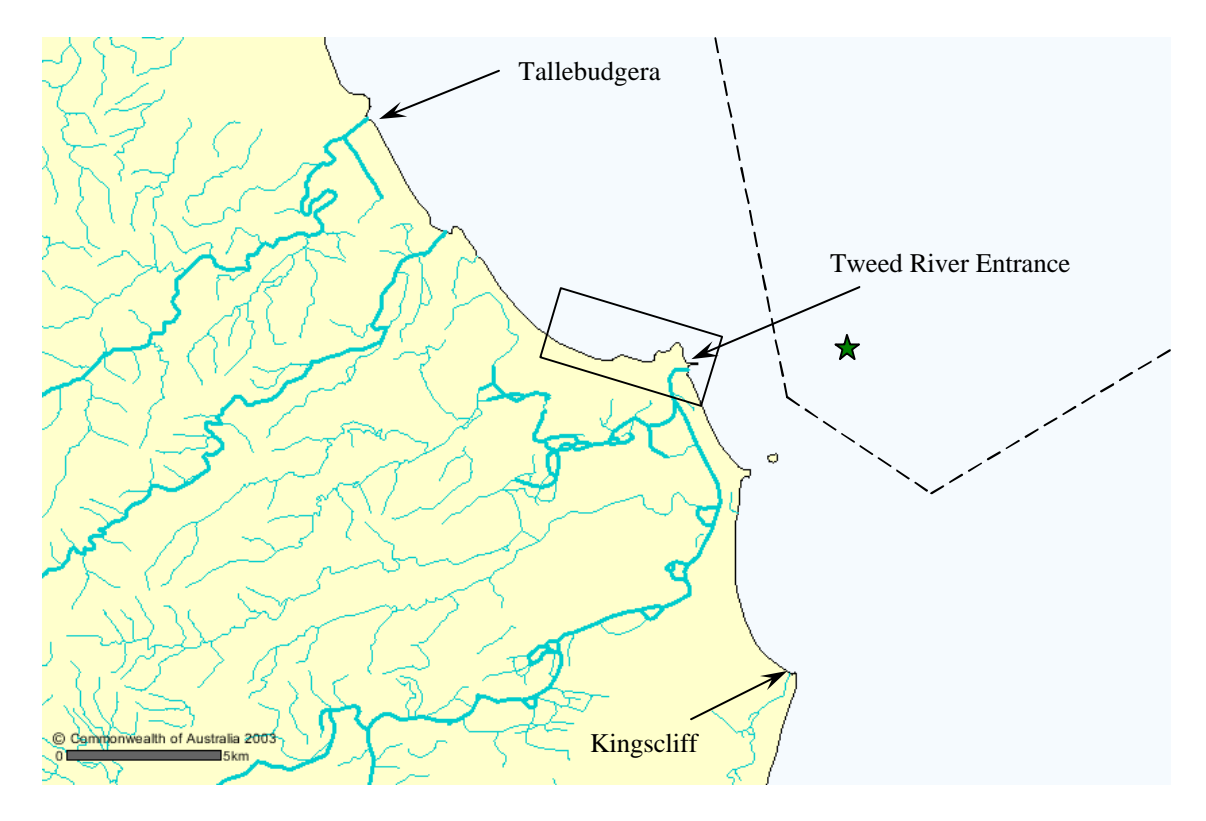


Figure 2: Map showing the main features of the study area. Relative locations of the radar sites at Kingscliff and Tallebudgera are shown. The directional wave buoy is also marked (star). The rectangle encloses the Tweed River Entrance Sand Bypassing Project shown in more detail in Figure 3. The dashed line shows a portion of the radar coverage zone.

The selection of the Tweed Heads region as an area of interest was not only due to the likelihood of strong swell conditions at this time but also to a recent agreement between New South Wales and Queensland state governments to undertake a joint project to employ and maintain a permanent sand bypass system at the entrance to the Tweed River. The aims for the project included an improved navigable entrance to the Tweed River and to supply a continuous volume of sand to beaches on the northern side of the river (Dyson et al., 2001). The entrance bar has historically been troublesome for ocean going craft to navigate due to a net northerly littoral flow of sand that fills the entrance. To combat this occurrence breakwaters were installed in the 1960s with considerable success. However in recent years the build up of sand on the southern wall became extreme and the entrance bar reformed. The sand trapped along this southern breakwater would have naturally supplied the beaches to the north

however with this in place these beaches experienced considerable depletion and erosion. It is these beaches that will be supplied by the bypass system along with initial mass dumps to restore them to their original condition. These mass movements will be supplied by sand collected from preparatory dredging of the river entrance. Figure 3 shows the location of the beaches supplied by the bypass project.

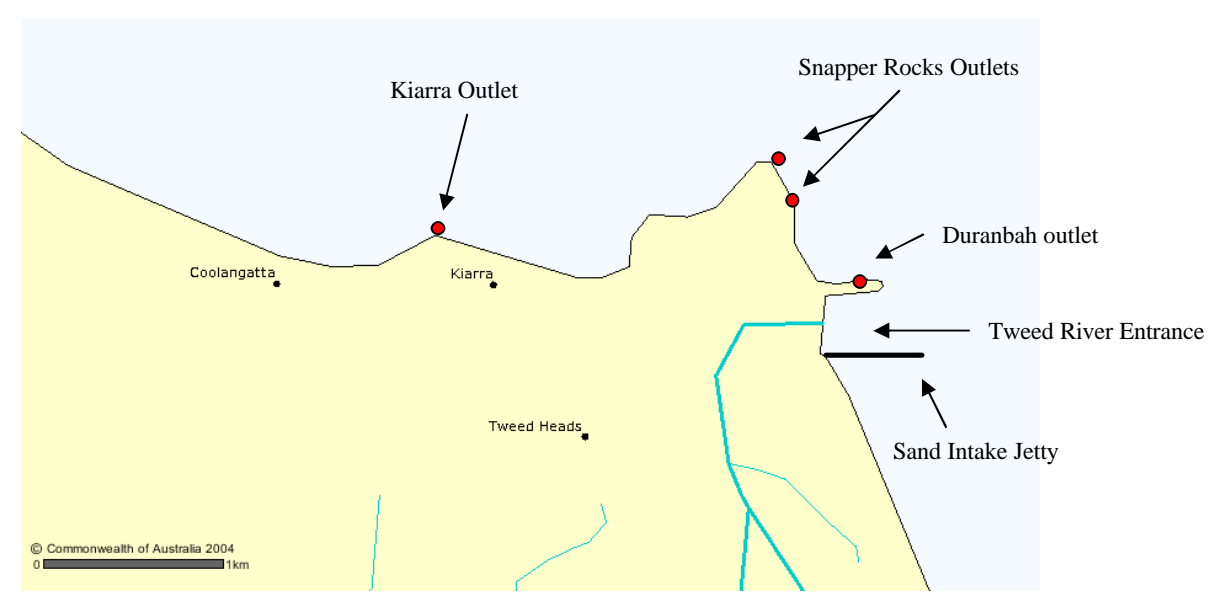


Figure 3: Detailed map of sand outlet points comprising the Tweed River entrance sand bypass project.

At the time of commission a coastal monitoring support system was also in place to provide information for management of the system in order to maintain both beach conditions to the north of the river and a safely navigable river entrance. The monitoring in place is of numerous forms including the Tweed directional wave buoy, a coastal image monitoring system (Anderson et al., 2003) and acoustic Doppler current profiles (ADCPs). This data has been used to produce morphological models of the river entrance to assist in determining how the entrance is reacting to this anthropogenic form of sediment transport (Callaghan and Nielson, 2003).

At the time of deployment this sand bypass project was not fully operational although initial dredging of the channel had occurred. This situation provided a good opportunity to display the ability of the COSRAD system to support such monitoring projects with valuable data including surface current and wave activity that impacts upon the natural sediment transport regime occurring in the area. Results acquired

from the developed directional wave algorithm could be used to provide independent estimates of natural sediment movement due to wave and surface currents which has previously been the role of the moored wave buoy. The wave buoy however only provides data at a single location. The use of COSRAD to provide data over a wider area would assist in observing the components involved in a larger sediment transport system. A map of the operational ocean coverage of the COSRAD system at Tweed Heads is shown in Figure 4.

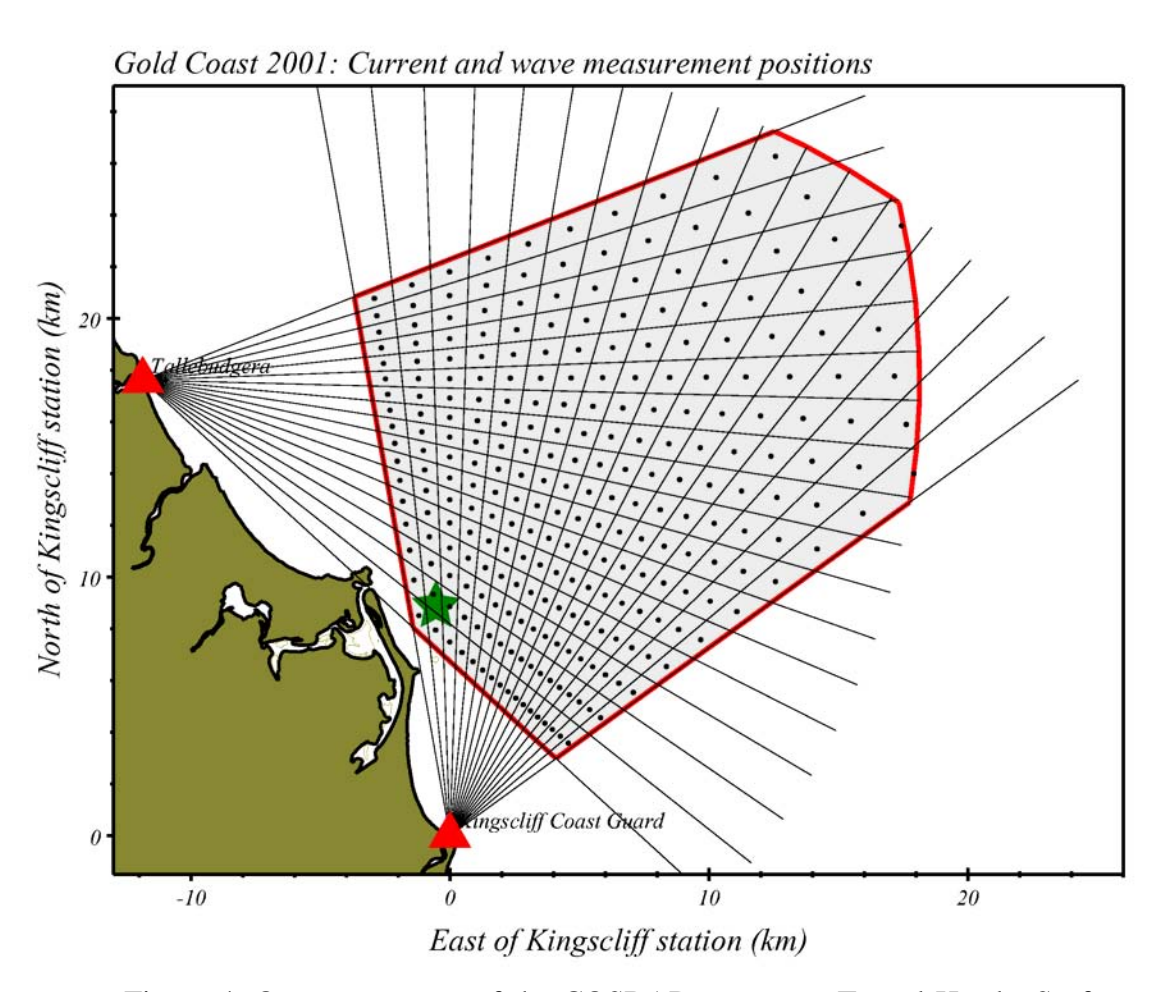


Figure 4: Ocean coverage of the COSRAD system at Tweed Heads. Surface current and wave measurements can be made in the areas of overlap between the two stations. The star marks the location of the QBPA directional wave buoy.

# 2.3.2 The Bass Strait Deployment

Port Phillip Bay has multiple uses including major port facilities, a significant commercial fishery and it also supports numerous nature conservation areas (Harris and Crossland, 1999). The HF COSRAD system has already been employed in this area as a valuable part of the Port Phillip Bay Environmental Study (PPBES) commissioned by the Government of Victoria and carried out by the CSIRO (Commonwealth Scientific and Industrial Research Organisation), (Provis, 2004). This study was concerned with an evaluation of the environmental state of Port Phillip Bay in terms of nutrient and toxicity levels. The COSRAD system was used to provide information in the form of current maps to describe the physical processes involved in the transport of these chemicals (Prytz and Heron, 1999). The coverage area is shown in Figure 5 below.

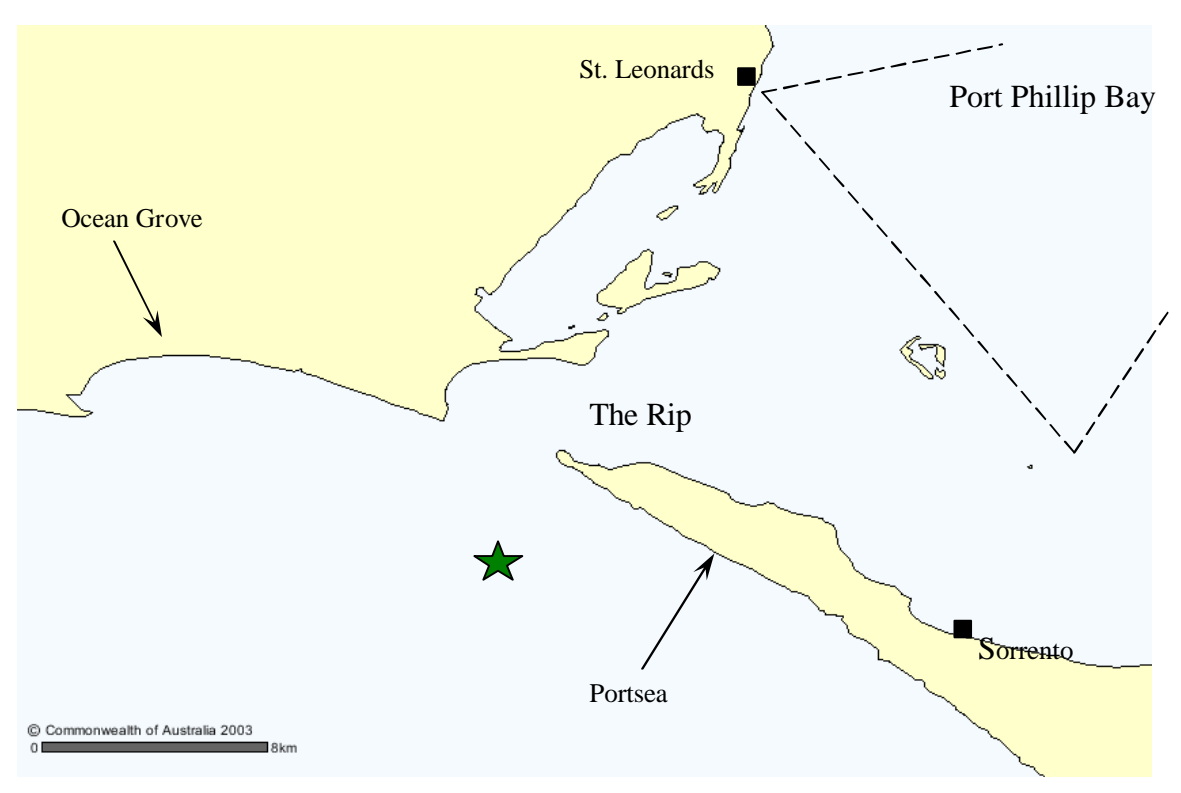


Figure 5: Port Phillip Bay study site. The locations of the COSRAD stations at Ocean Grove and Portsea are shown. The wave rider buoy is also marked (star). The dashed line encloses the coverage area of the previous COSRAD study attached to the PPBES (1999).

The Bass Strait deployment was focussed more towards the extraction of swell data than the Tweed Heads deployment and configuration changes were made to the radar system to facilitate this. The focus on swell detection was the primary reason for the choice of location and the time of year. Bass Strait is known for the large sea states that often reach the shores of Victoria during the winter months (Spillane *et al.*, 1972). Safe passage through Port Phillip Heads for both commercial and recreational vessels is also of concern.

Monitoring of the ocean surface near the entrance to Port Phillip Bay by two COSRAD stations began on the 27<sup>th</sup> of June and ended on the 26<sup>th</sup> of July 2001. The coverage area, the portion where the two sweeps overlap, is shown in Figure 6. The locations of the stations at Ocean Grove (38°16.425'S, 144°30.943'E) and Portsea (38°20.15'S, 144°42.202'E) are shown and are clearly separated by the entrance to Port Phillip Bay. The area shown sufficiently covers all approaches into the Bay and therefore indications of swell wave activity in this region will be extremely valuable for shipping safety.

The operating changes made to the COSRAD system to assist in the extraction of swell parameters were to increase the dwell time at each position. Although this results in a lower temporal resolution it is again not of great concern when extraction of swell is the main objective. This increased dwell time enhances the backscattered ocean signal against the surrounding noise. This parameter was not set for the Tweed Heads deployment because the objects were slightly broader and therefore a compromise was reached. The temporal resolution is an important factor when trying to monitor surface currents and wind direction as they can change significantly within a short time period. As mentioned earlier an entire sweep of the area was produced every 30 minutes at Tweed Heads, this was increased to an hour for the Bass Strait deployment.

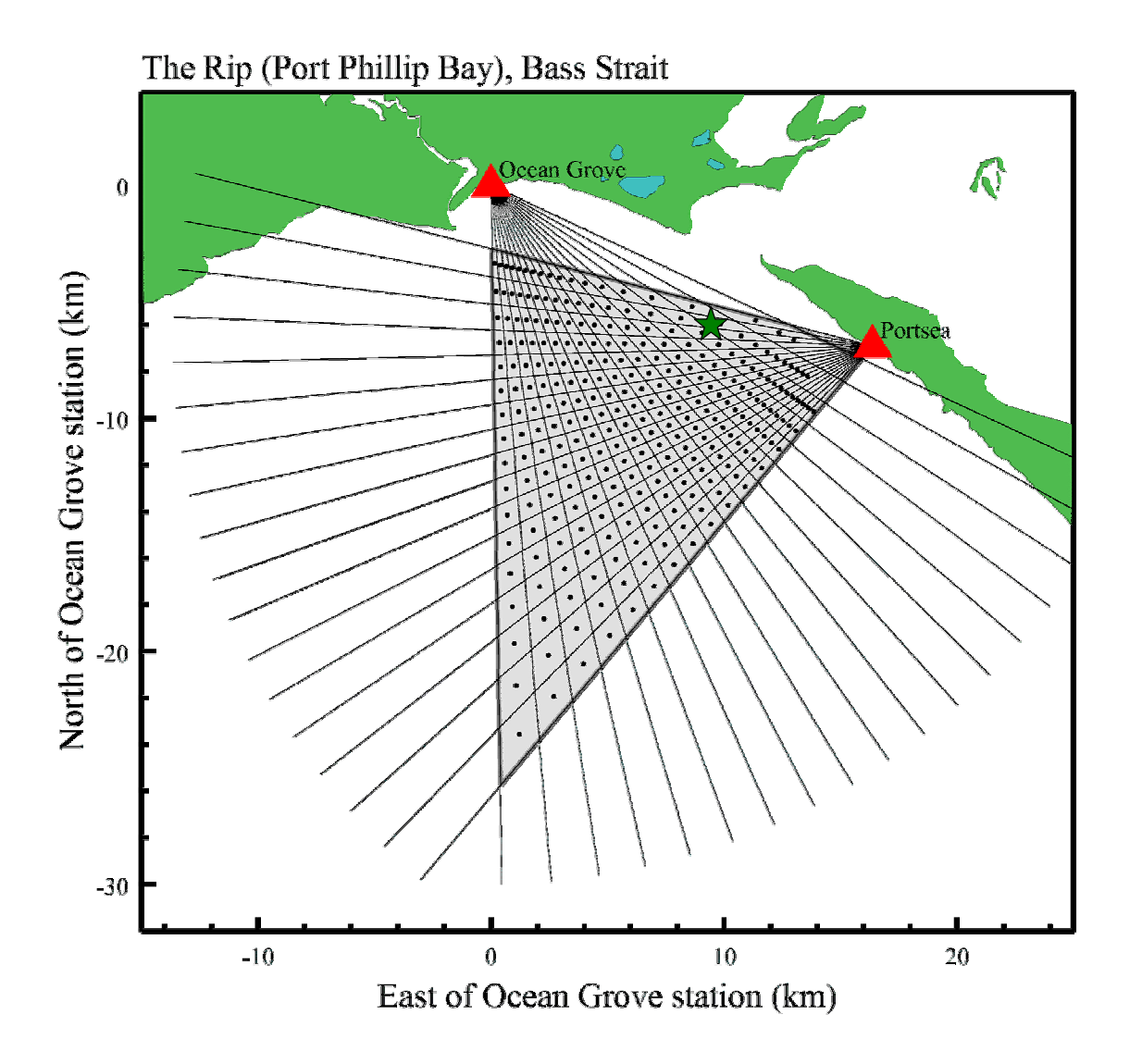


Figure 6: Coverage area of the COSRAD system monitoring the entrance to Port Phillip Bay. The directional wave buoy here (star) is maintained by the Port of Melbourne Corporation.

# **Chapter 3: Pre-processing COSRAD Spectra**

Prior to incoherent averaging of numerous Doppler spectra, there are two essential processes that need to be performed. Firstly, frequency offsets that are present in each spectrum due to surface water movement need to be removed to avoid spectral broadening and peak bifurcation when averaged. The signal power depends on various factors including the attenuation of the electromagnetic wave between the transmitter, target and the receiver, the scattering strength of the target and background noise (Gurgel, 1999). A noticeable reduction in signal strength with increasing range introduces a bias towards nearshore pixels when averaged. To provide an unbiased averaged spectrum, the received power level of each spectrum, as we move away from the transmitter/receiver in each sector, needs to be normalized.

Once these processes have been completed, the spectra can be incoherently averaged to reduce the noise level and enhance the signal to allow the extraction of long ocean wave parameters.

### 3.1 Frequency Normalization

The frequency shift away from the theoretical Bragg frequency,  $f_{\rm B}$ , needs to be removed prior to further manipulation of the Doppler spectra. If the first-order peaks occur at the Bragg frequency then there is no bulk movement of surface water. Movement of surface water produces a frequency shift in the received spectrum that can be used to determine surface current radial velocities, but for the extraction of second-order parameters this information can be removed allowing for spectral enhancement processes to be applied. COSRAD transmits at a frequency of 30 MHz ( $f_0$ ), which corresponds to a Bragg frequency of  $\pm 0.56$  Hz by the relation:

$$f_B = \pm \sqrt{\frac{gf_0}{p_c}} \tag{13}$$

where c is the speed of light.

In order to return the Bragg peaks to the Bragg frequency they must firstly be identified in the spectrum. Identification of first-order features is far easier than those embedded in the second-order due to the favourable signal to noise ratio. The general position of the Bragg peaks can be assumed to be within a relatively small window around the Bragg frequency and to be the most prominent feature in that region. Therefore a window of 0.1 Hz is used, centred on the Bragg frequency, to search for the Bragg peaks. Both peaks are identified in this manner and then compared to find which peak is stronger.

The most reliable method of evaluating the Doppler shift ( $\Delta f$ ) is to work with the stronger of the two Bragg peaks (Georges *et al.*, 1981). The stronger peak should always be unambiguously identified and the amount it has moved away from the Bragg frequency can be easily calculated. The value of  $\Delta f$  can then be removed from the entire spectrum leaving the two Bragg peaks at a frequency of  $\pm 0.56$  Hz.

Incoherent averaging of Doppler spectra without the removal of this frequency shift, results in a smearing of the peaks along the frequency axis, due to variations in the amplitude of surface currents over the area represented by the spectra being averaged. This smearing is evident as a series of broad peaks. Then accurately identifying the position of these peaks for the calculation of swell wave parameters is not possible and defeats the purpose of the averaging process, which is to enhance the second order peaks for analysis.

### 3.2 Power Level Normalization

Power-level normalization is an integral part of the spectral enhancement process. This process precedes the incoherent averaging which reduces the variance of the spectrum in preparation for the analysis of the second order continuum. Attenuation of the signal with increasing range, due to propagation losses in the electromagnetic wave, results in a gradual decrease in signal strength received from more distant pixels. Pixels closer to the antenna array have a distinctly higher power level than those further away. This presents a problem if adjacent pixels, in range, are to be incoherently averaged because

the higher-powered pixels would dominate and the resulting spectrum would not be representative of the entire area but would be an overestimate favouring the nearshore pixel. This is shown in Figure 7, where the spectral energy density samples of three pixels, increasing in range, have been sorted in descending order. This method of spectral analysis, known as rank-ordering, was developed by Heron and Heron (2001) as a means of identifying the main features of the spectrum, including the first-order peaks, the second-order continuum and the noise floor. It is also an appropriate technique to employ to compare the degree of attenuation affecting the electromagnetic wave with increasing distance. The high energy values at the low sample numbers represent the first-order Bragg peaks in the spectrum and show great variation over the three ranges. Pixel 3 is closest to the receiver, and pixel 6 and 9 are distant. As shown the power level of the signal decreases significantly as the pixel is further removed from the receiver.

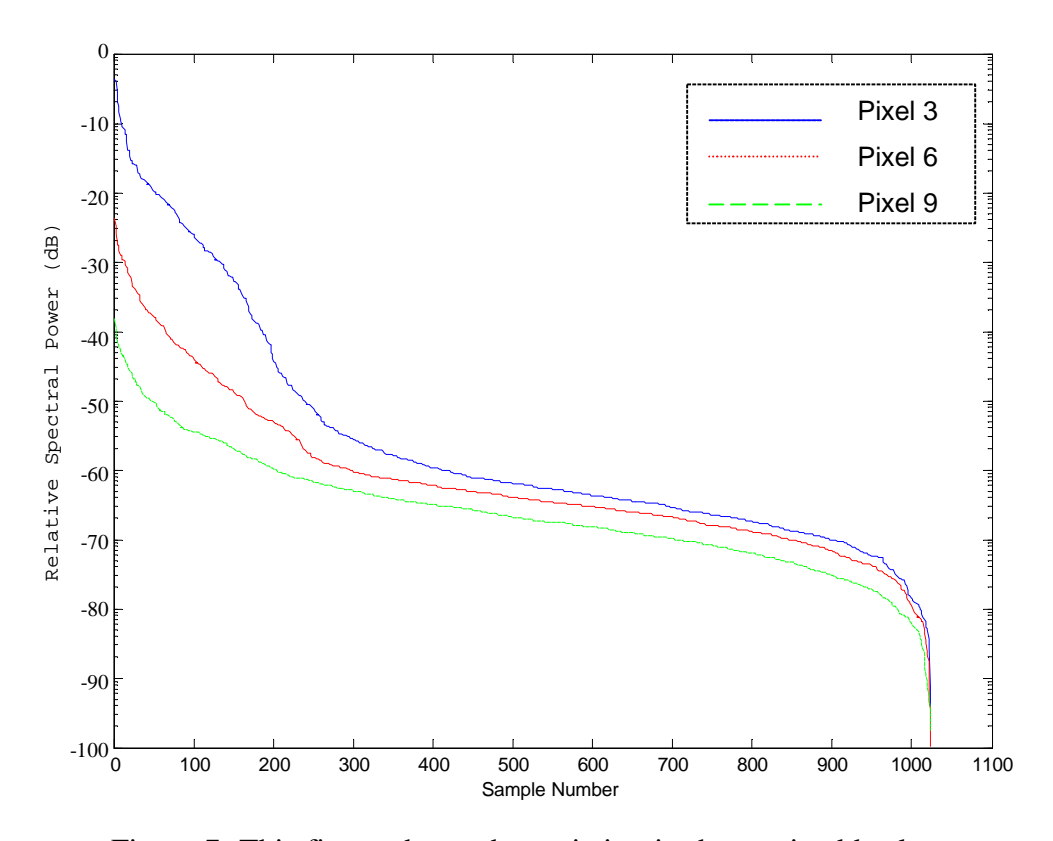


Figure 7: This figure shows the variation in the received backscatter power with pixel distance. The energy of each spectrum has been rank ordered to highlight the power loss. Pixel 3 is closest to the receiver and therefore has the highest power.

This increase in signal attenuation is due to energy loss as the electromagnetic wave travels the greater distances to more remote pixels. At sample numbers greater than approximately 400 the energy density being measured is the background noise. This noise level is very similar for the three ranges but the noise received also reduces slightly with increased range.

To compensate for this effect, the power-level for all pixels needs to be normalized to a common pixel prior to further spectral processing. For the extraction of long ocean wave parameters the relationship between the second-order peaks and the Bragg peaks are analysed and therefore as long as we preserve the relative positions and strengths of the peaks the analysis is not adversely affected by the normalization process. The normalization procedure used here is to rescale the spectra intended for averaging so that each spectrum has the same peak power level. This method gives the best match at the peak values but not in the wide band portion of spectrum due to the variation in noise level with range. There are numerous other methods of normalization discussed by Georges *et al.*, (1981) and Barrick (1980) such as total power, minimum variance and logarithmic normalization which perform better than peak normalization in the wide band portion of the spectrum. However, we are only concerned here with the first and second-order parts of the spectrum which are unaffected by this problem. Peak power normalization is fast and computationally simple which aids in our goal of running the resulting algorithm in near real-time.

The stronger of the two Bragg peaks in the most nearshore spectrum is used as the reference power level to which all other spectra to be averaged will be normalized to. A common concern with this method is the possibility that the stronger Bragg peak in these spectra may not always be found to be on the same side of the spectrum. As the radar sweeps across in angle the Braggs peaks will change in strength. However, as long as the spatial averaging is limited to one or two sectors in angle the probability of this causing a problem is small. The amount of averaging required to produce the desired signal to noise ratio will be discussed below however it will be no more than two sectors.

Upon completion of this process, all the pixels are of an equivalent power and can be incoherently averaged without a bias being imposed by high backscatter returns from pixels in relatively close proximity to the receiver.

## 3.3 Incoherent Averaging of Doppler Spectra

Smoothing the resulting backscattered spectrum is essential to enable the analysis of any second order structure that may be present. Prior to averaging, the second-order is lost in the surrounding noise and is very difficult to identify. By averaging as few as 4 individual spectra the noise level is reduced and the signal is enhanced therefore improving the signal to noise ratio. Precautions have been taken, as explained above, to limit the occurrence of smearing due to the averaging of offset peaks by the Doppler shift. Also, the amplitudes of the spectra have been normalised so all are of similar levels before averaging occurs and therefore there is no bias towards near shore scatter.

#### 3.3.1 Spatial Averaging

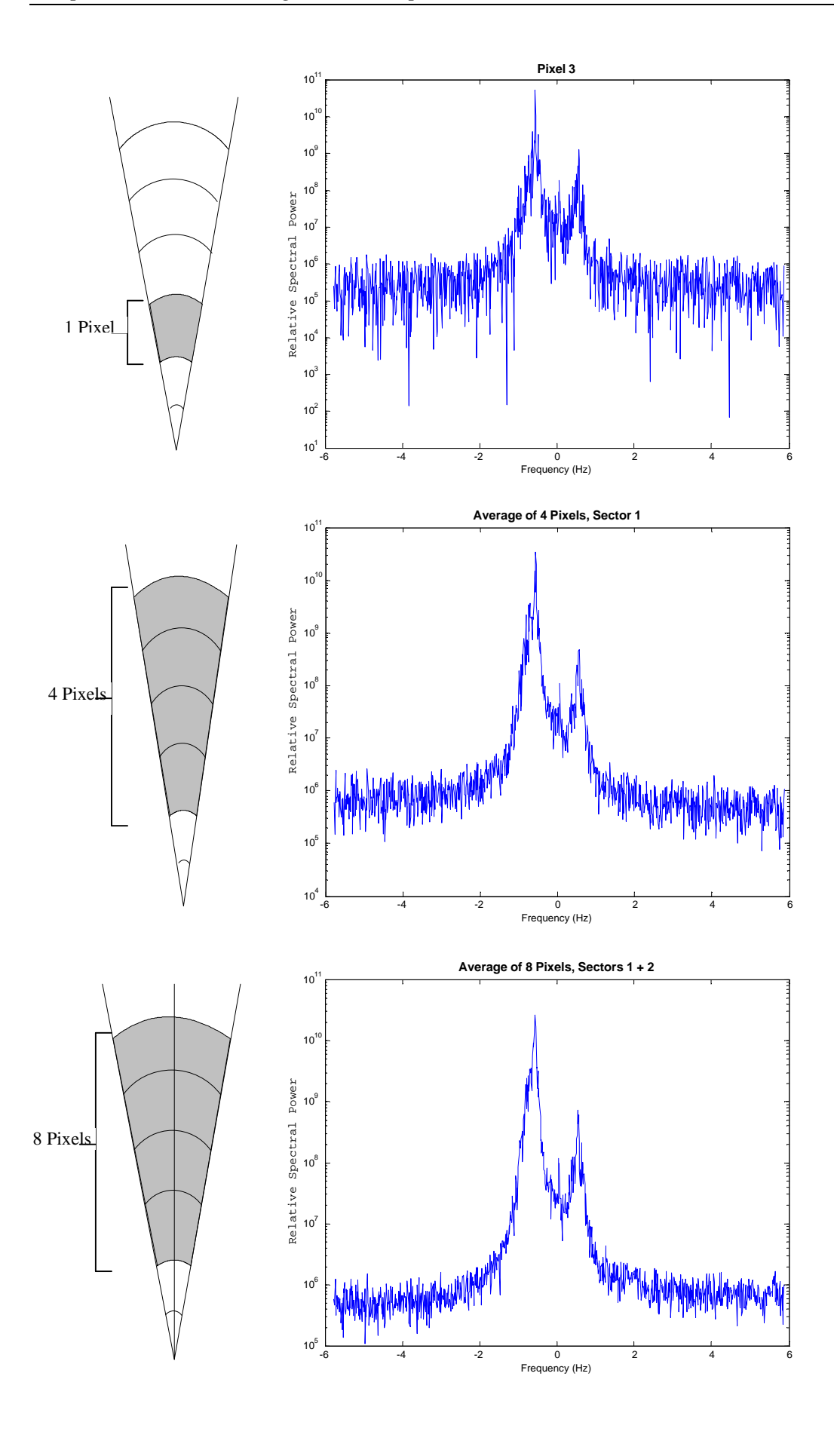
Uniform spatial conditions make spatial averaging a desirable option. A typical COSRAD sweep creates a uniform grid of pixels divided into 17 sectors covering  $\pm 30^{\circ}$  about the bore sight of each station. The range resolution for the COSRAD system is set at 3 km. The increase in spectral clarity achieved by incoherent averaging is a trade off for decreased spatial resolution. This is not of such a concern when the purpose of the process is to enhance the second-order spectrum for extraction of long ocean wave parameters. Swell waves in particular do not vary greatly in height or direction over small areas in deep water.

The amount of averaging needed to obtain a reasonable compromise between the clarity of the second-order spectrum and still retain an acceptable spatial resolution is found empirically. Figure 8 shows the number and position of the pixels averaged and the effect it has on the resulting Doppler spectrum. The degree of incoherent averaging was confirmed by increasing the number of pixels to be averaged and trying to identify

second-order features reliably at each stage. This ensured that averaging was not applied in excess, unnecessarily reducing the spatial resolution. As shown in Figure 8, averaging over just 4 pixels enhances the signal to noise ratio significantly. Further enhancement is achieved by averaging the 4 adjacent pixels in the next sector. The second-order peaks are now distinguishable above the noise. This can now be taken further by averaging temporally so that no more spatial resolution is lost.

### 3.3.2 Temporal Averaging

Temporal averaging is not a desirable method of smoothing when looking at relatively short wavelengths in the ocean wave spectrum. Waves with periods less than approximately 8 seconds tend to respond to changing wind conditions too rapidly to smooth temporally without significantly compromising the resolution required to describe the conditions. Swell waves typically have periods between 8 and 16 seconds or greater and respond to changes in wind direction in the order of hours. The amount of averaging in the temporal domain was again decided upon empirically, guided by the fact that swell is not driven by local winds and therefore does not alter its form in short time periods. Figure 9 shows the resulting spectrum averaged over a two hour period. This equates to four consecutive sweeps by COSRAD. In each half hour period 8 pixels are averaged spatially, as discussed above, therefore over a two hour period a total of 32 pixels are averaged to produce the final spectrum shown in Figure 9. Second-order features can now be examined without interference from surrounding noise. This is ensured by introducing a safety measure in the identification of the surrounding noise level before calculations begin.



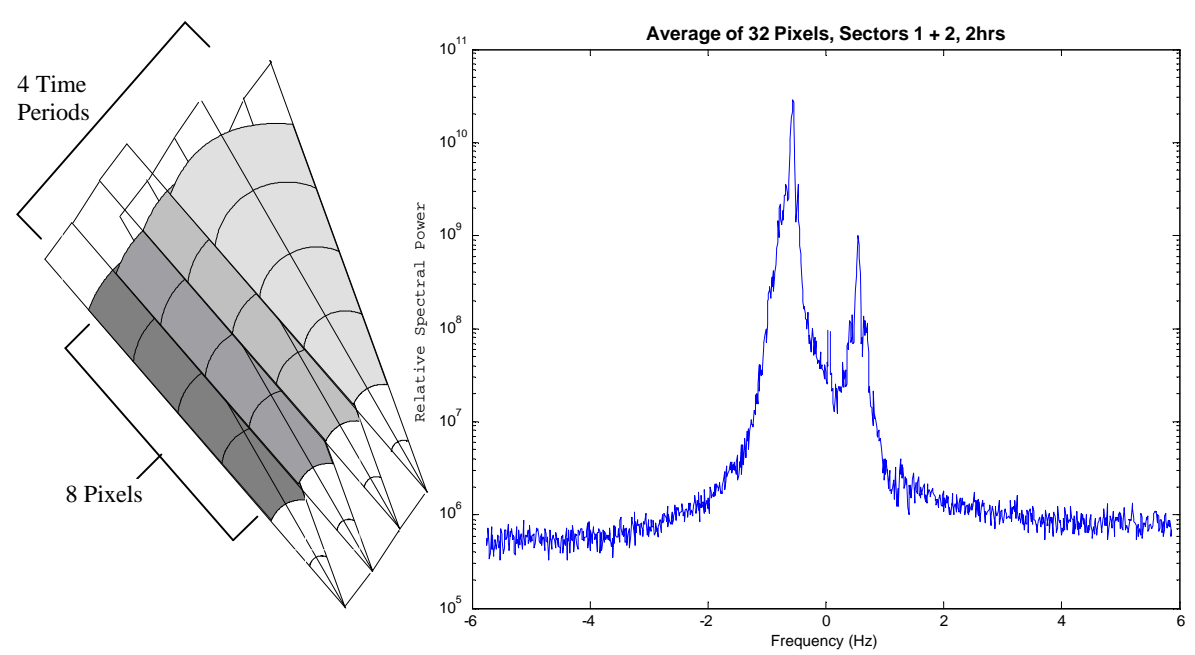


Figure 9: Temporal averaging. Averaging over 4 time periods to further enhance the signal to noise ratio. Swell reacts slowly to local conditions thus a high temporal is not necessary.

#### 3.4 The Noise Floor

Analysis of second order swell peaks is far more involved than that of the first-order Bragg peaks. The first-order Bragg peaks typically sit 20-30 dB above the second-order spectrum and a further 10-20 dB above the noise floor. Due to the proximity of the second-order spectrum to the noise floor it is important to know exactly how close they are and whether spectral noise is affecting the second-order spectrum.

There are many methods available to determine the noise floor of a frequency spectrum, however for this purpose it is sufficient to simply divide the Doppler spectrum into 10 bins, as shown in Figure 10, and find the mean power level in each bin. A bin that includes structure from Bragg resonance or spiky noise from sferics and anthropogenic sources will contribute to a higher mean power density. Therefore, the bin with lowest mean power density will closely represent the noise floor. It is then easy to see if the background noise is interfering with the second-order spectrum and therefore if the

integrity of the information extracted from the swell peaks is valid. A buffer of 10 dB between swell peak amplitudes and the calculated noise floor is used to prevent interference from noise being used to calculate swell wave parameters. Swell peaks that lie within this buffer can not be identified with the same high confidence as peaks that lie above the buffer, and are excluded from further analysis.

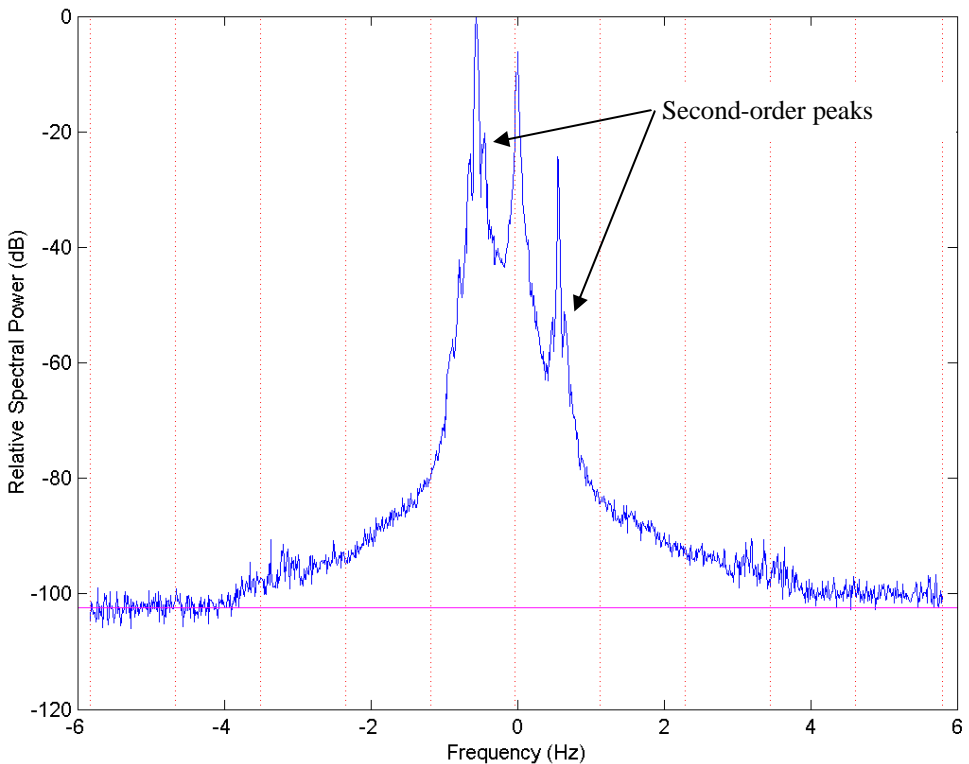


Figure 10: The noise floor is calculated by dividing the Doppler spectrum into 10 bins (dotted lines) and finding the mean power level in each. The lowest value is a close representation of the noise floor (grey horizontal line). Second-order peaks in this case are ~40 dB above the noise floor.

### 3.5 Discussion

Upon completion of these essential pre-processes, methods of swell parameter extraction can be examined. Prior to this, development of algorithms dealing with the second-order spectrum would have yielded poor results due mainly to poor reliability in

identifying the correct peaks. Removal of the Doppler shift due to surface currents is a vital step prior to spectral averaging to prevent severe smearing of the resulting spectrum. This process is common practice in many disciplines involving frequency spectra and along with the normalisation of each spectral range cell, the COSRAD data was prepared for the averaging process.

The incoherent averaging process is an extremely important stage as it ultimately dictates the resolution of the output from the algorithm. With HF spectra collected by COSRAD the incoherent averaging of 32 pixels was found to provide coverage over the largest area. The 17 sectors in a COSRAD sweep are numbered from -8 to +8. We spatially average across two neighbouring sectors then repeat this pattern across the radar sweep, each time overlapping the previous sector. For example the averaging pattern begins by utilizing pixels from sectors -8 and -7 and continues then to average across sectors -7 and -6. This pattern produces 16 incoherently averaged HF spectra across the sweep. This degree of averaging is a reasonable trade of spatial and temporal resolution for improved spectral clarity. The resolution achieved here is adequate to provide useful information on swell conditions over a vast area.

# **Chapter 4: Methods of Extracting Swell Wave Parameters**

The routine extraction of swell wave parameters, period, direction and height are the main aim of this project and also an important goal for the field of radio oceanography in general. This section details the development of an algorithm to do this using Lipa and Barrick's (1980) explanation of the second-order spectrum and inversion methods for extraction of long ocean wave parameters. The second-order peaks in the spectrum result from a second order wave-wave interaction. Swell waves are produced by distant storms or strong winds with a relatively long duration. The swell waves seen at the coast have travelled great distances from their point of generation and during this time they become well organised and quasi-sinusoidal in nature (Kinsman, 1965). These waves are often categorised as long ocean waves usually with a period greater than ten seconds (Lipa et al., 1981). In contrast, wind waves are generally defined as waves that are continually generated by local winds and appear far more random in their structure because of their broader spectrum. In the Doppler spectrum swell waves can be seen as the first prominent peaks in the second order continuum surrounding the first-order Bragg line. These peaks are positioned almost symmetrically about the first-order line, however complications in swell peak identification still occur. Correct identification of these peaks is a vital step in the preparation for the calculation of swell parameters.

The swell peak recognition routine developed and implemented here uses frequency windows, as used when locating the first-order peak, within which the peaks are expected to be found. As a conservative estimate a large window was used so that possible swell peaks were not excluded. This window was determined by the upper and lower wave periods which define the swell wave band and separates swell from sea. Kinsman (1965) defines ten seconds as an approximate boundary between sea and swell with considerable overlap. Therefore to allow for short period swell a lower boundary of eight seconds was chosen. Barrick (1972b) used an upper limit for swell period as sixteen seconds. Again, a conservative upper limit of eighteen seconds was used. These boundaries were converted to act as the frequency limits of the window.

## 4.1 Peak Finding Algorithm

To extract information from the HF Doppler spectrum the first-order and second-order peaks need to be identified. This may seem a trivial part of the process however the creation of a robust peak selection routine can become complex when peaks are not clearly defined amongst their surroundings. It may not be difficult to manually identify these features individually in each spectrum but this is not feasible considering the amount of data collected over the course of a deployment. The aim of automating peak selection is only valid if a high standard of peak identification can be maintained. Spectral processing procedures are an essential precursor to aid in peak identification. Locating first-order peaks may be possible in a raw spectrum, however second-order features would not be differentiated from spectral noise in most cases. The theoretical position in frequency is known for both first and second-order peaks. First-order peaks can be located within a relatively small frequency band centred on  $\pm 0.56$  Hz for a radar frequency of 30 MHz. This is of course after the Doppler shift due to surface currents has been removed. We can also define a frequency range within which we expect to find the second-order swell peaks. Swell is typically defined as having a period between 8 and 18 seconds which translates to a frequency between 0.125 Hz and 0.055 Hz respectively. This frequency window sits on both sides of the first-order peaks and therefore must be added to and subtracted from ±0.56 Hz. The limits to the four second-order frequency windows are shown in Table 1:

	Frequency (Hz)	
Swell Peak 1	-0.66	-0.615
Swell Peak 2	-0.505	-0.46
Swell Peak 3	0.46	0.505
Swell Peak 4	0.615	0.66

Table 1: Frequency windows which should contain swell peaks if present in the spectrum.

This information provides a basis for routinely locating the peaks and the remaining algorithm determines if a potential peak conforms to certain criteria that define a

spectral peak. This refers to differentiating between a true peak and spectral noise spikes for example.

Figure 11 shows two bands defining the swell windows on either side of the receding Bragg peak.

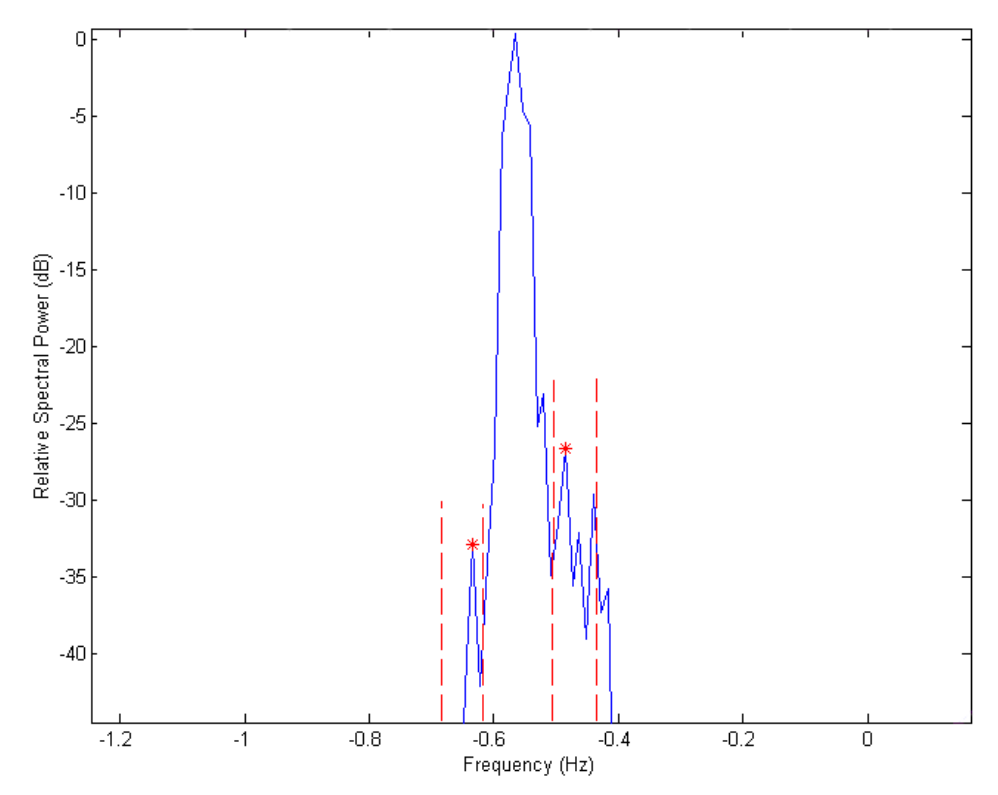


Figure 11: Receding Bragg peak at -0.56Hz flanked by two identified swell peaks (asterisk) inside the defined swell frequency windows with boundaries shown by dashed lines.

The spectrum shown above has been processed following the procedures discussed previously and it is therefore an average of 32 individual spectra spanning 8 pixels over two adjacent sectors in the spatial domain and 2 hours (4 half-hour periods) in the temporal domain. This particular spectrum has well defined swell peaks that are easily identified. However, swell peak selection is not always so straightforward. Compared to the identification of first-order Bragg peaks, these swell peaks are not orders of magnitude above other nearby spikes. The second-order continuum contains legitimate peaks other than swell that can confuse routine identification. Adjacent wind wave

peaks and signal degradation can impact on accurate identification. An example of this occurs in figure 11. The swell window on the right hand side of the Bragg line contains two other discrete peaks besides the selected swell peak. In this case the peak with the highest amplitude in the window is chosen as the swell peak. The next peak appears to be a spur like spike that has split from the main swell peak. The third peak is a prominent peak just inside the swell frequency window. This possibly represents a wind wave signal and shows how the range in frequency between these categories can overlap. Confidence in the selected peak in this case is supported by location in frequency of the other identified swell peak. Confidence in the selected peak on the left hand side of the Bragg line is high as it is a sharp spike and it is the only peak present in the swell window. Its proximity to the inner boundary of the swell window also matches that of the selected peak on the opposite side. Once the peaks have been identified, the analysis of the swell peak positions and the extraction of swell parameters can commence.

#### 4.1.1 Peak Identification

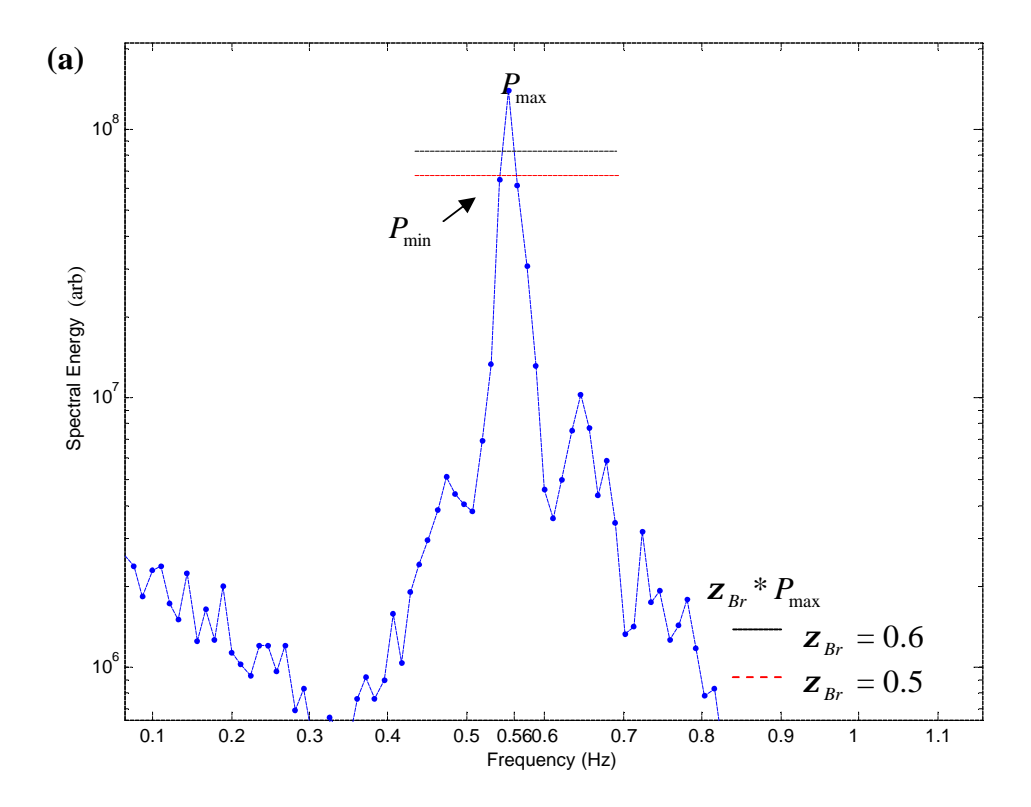
Identifying a value as a peak is not as simple as finding the most powerful value in the spectrum or specified frequency windows; however, this is a starting point. To classify a point as a peak the surrounding values must be significantly reduced in power for the peak to be clearly defined. Assigning a quantitative measure to this reduction comprises part of the criteria employed by the algorithm to correctly identify a peak value. Hence, an eligible peak needs to conform to

$$P_{\min} \le \mathbf{Z}_{Br} P_{\max} \tag{14}$$

where  $P_{\max}$  is the peak value in question,  $P_{\min}$  is the point adjacent to  $P_{\max}$  and  $\mathbf{z}_{Br}$  is the reduction factor which should be of the order 0.5 to 0.6 for first-order peaks. This determines what is acceptable in terms of how prominent a peak needs to be. Deciding if  $P_{\min}$  should be less than 50% or 60% of  $P_{\max}$  needs to be determined empirically on a small test set of the deployment data to find a value that produces reliable results. This factor is likely to change between data sets and even during the course of a deployment as sea state conditions vary.

The Bragg peak is usually easily identified and only confuses the above method of definition when bifurcations are present. As shown in Figure 12(a) a well formed Bragg peak is usually an order of magnitude above its adjacent points in the spectrum and when this is the case the peak is selected without any degree of uncertainty. However, when the Bragg peak is not so well formed, as in Figure 12(b), the algorithm requires a more substantial criterion to resolve the location of the peak. Even though  $P_{\text{max}}$  is the correct peak location the algorithm will initially reject it and look for an alternative peak. If another suitable peak cannot be found the original choice is accepted and will be a source of noise that is, to some degree, carried through to the calculated wave parameters.

Swell peak selection employs the same methodology although  $\mathbf{z}_{sw}$  is typically larger than the determined value for  $\mathbf{z}_{Br}$ , approximately 0.6 to 0.7. This is due to peaks in the second-order continuum being less prominent amongst their surroundings than is the case in the first-order. Figure 13 illustrates the difficulty of swell peak selection with an example of a strong and clean swell peak juxtaposed with a bifurcated swell peak surrounding the same Bragg peak. The methodology easily identifies the strong peak on the left side of the Bragg peak however the bifurcation in the peak on the right hand side causes the algorithm to search for an alternate peak. However, outside of the two peaks that form the bifurcation there is no other acceptable peak inside the swell window. Therefore, the stronger one of these peaks must be selected even though the true swell peak position is likely to be between the two with an increased power level.



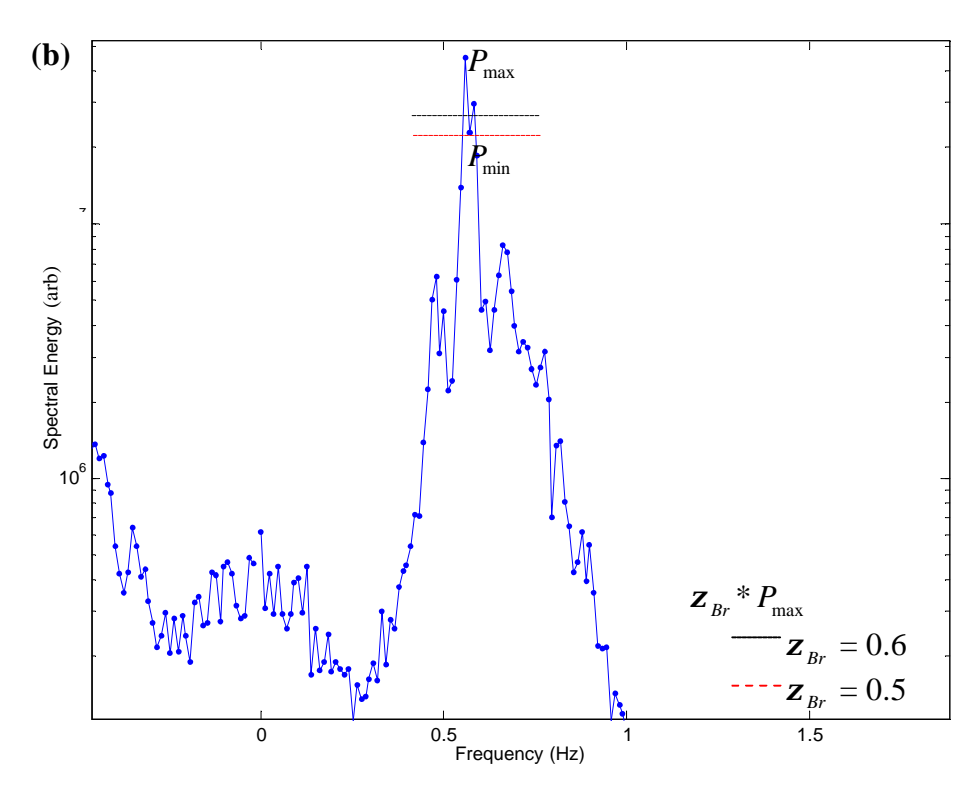


Figure 12(a): A strong clean Bragg peak meets the criterion even with  $\mathbf{z}_{Br}$  =0.5. (b) The algorithm rejects  $P_{\text{max}}$  with  $\mathbf{z}_{Br}$  set at 0.5 due to the bifurcation however it is accepted with a more lenient  $\mathbf{z}_{Br}$  set at 0.6.

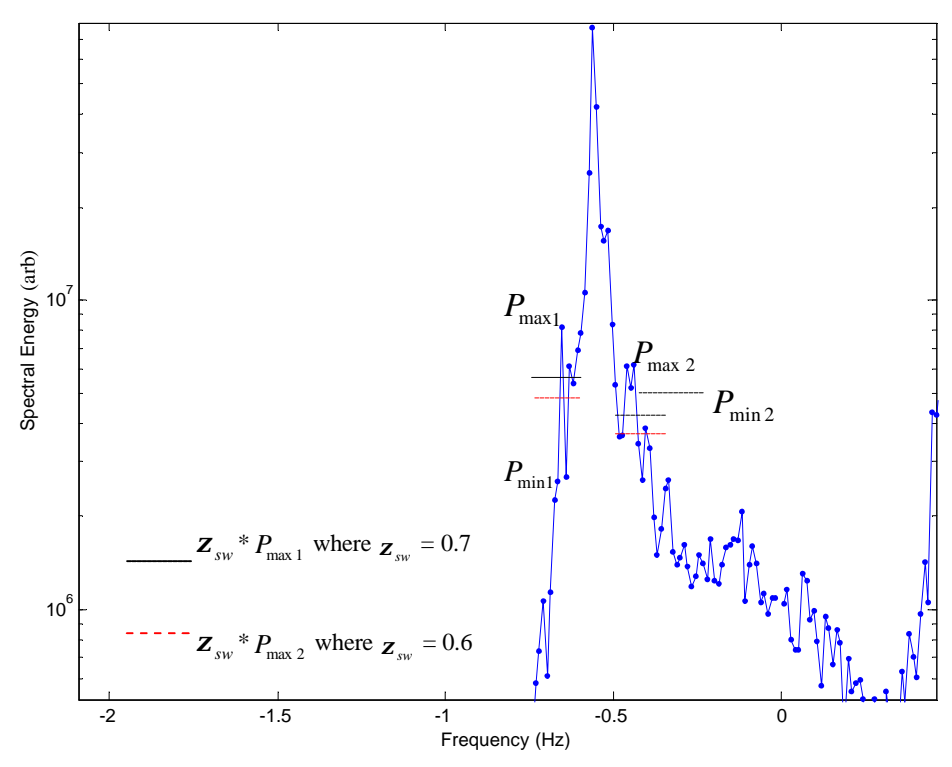


Figure 13: Swell peak selection with examples of strong and noise affected peaks.

#### 4.1.2 Peak Definition

In some instances it is not enough to just know the location and power of a peak but also peak area and peak width are useful. To acquire this extra information the peak needs to be defined in more detail. Calculating the area under a peak requires limits to the frequency width of the peak, or nulls to be identified. Peak width is generally regarded as the widest point between the two sides of the peak which is invariably the distance between the nulls. As with peak location, the shape or form of the Bragg peak is easier to define than the swell peaks. When the Bragg peak is surrounded by prominent swell peaks a clear null is usually formed in between (Bragg null). In most cases this null is shared by the Bragg peak and the swell peak. Difficulty arises in identifying a null on the side of the swell peak that is facing away from the Bragg peak. The second-order is a continuum with limited features outside of the swell peaks to form an identifiable null. The solution to this problem will be discussed later. The method used to identify a true null is similar to peak identification,

$$P'_{\text{max}} \ge \frac{1}{z} P_{\text{min}} \tag{15}$$

where  $P'_{\max}$  is the adjacent maximum to the possible null  $P_{\min}$ .  $\mathbf{z}$  is the same factor as used in the peak identification algorithm and will retain the same value depending upon Bragg or swell null definition. Previously, in the peak identification algorithm,  $P_{\min}$  was not necessarily a null value, however, if the above relation is true then  $P_{\min}$  is defined as a null.

As stated above, the nulls for a Bragg peak are usually well defined and relatively easy to identify. The Bragg nulls are defined as the points in the spectrum at which the sides of a Bragg peak reach a minimum before the second-order frequencies are reached. The algorithm simply searches for the lowest point between the Bragg peak and the surrounding swell peaks and is verified or rejected using equation 15. Problems arise when there is a missing swell peak causing the algorithm to redefine a frequency window to search for a possible Bragg null. In this case the relevant value from Table 1 that defines the inner limit (limit closest to the Bragg peak), is chosen. This case is similar to that of finding a null for a swell peak on the side facing away from the Bragg peak. Firstly a frequency limit needs to be defined to stop the algorithm searching for a null that is too far from the peak. Due to the reliability of finding a definite null on the Bragg peak side of the swell peak we can estimate the peak width as twice the distance from the swell peak to Bragg null and use that as an indication for locating the second null. The peak width can then be used to set an outer limit for the algorithm. In case the peak is not quite symmetrical the limit is set at a point that is an estimated peak width from the centre of the peak thus allowing for some unexpected peak shapes.

# 4.2 Processing of Swell Peak Positions

Obtaining accurate swell peak positions is not a simple task due to their proximity to the first-order peaks and the remaining second-order continuum. Despite care taken during spectral enhancement processes to prevent smearing of the peaks in frequency, common causes of incorrectly located swell peaks are bifurcation and broadening effects. These errors occur mainly due to surface current structure within the pixel. A number of

procedures were developed and utilized to reduce these effects and increase accuracy where possible. These include, applying a weighted mean over all located swell peaks and imposing frequency limits to the locations of each peak. These methods reduce the impact of peak broadening and bifurcation on subsequent calculations.

# **4.2.1** Weighted Mean and Frequency Limits

The algorithm developed here utilizes these two methods to repair or discard adversely affected swell peak positions. Firstly a weighted mean routine is indiscriminately applied to all swell peaks in an effort to minimize effects of peak broadening and peak bifurcation. The peak is categorised as 'broad' if data points adjacent to the peak have a similar power level. If there is a second or third distinguishable peak of similar but lower intensity in the immediate vicinity of the swell peak, separated by a single data point, it is bifurcated. Examples of swell peaks affected in this way are shown in Figure 14.

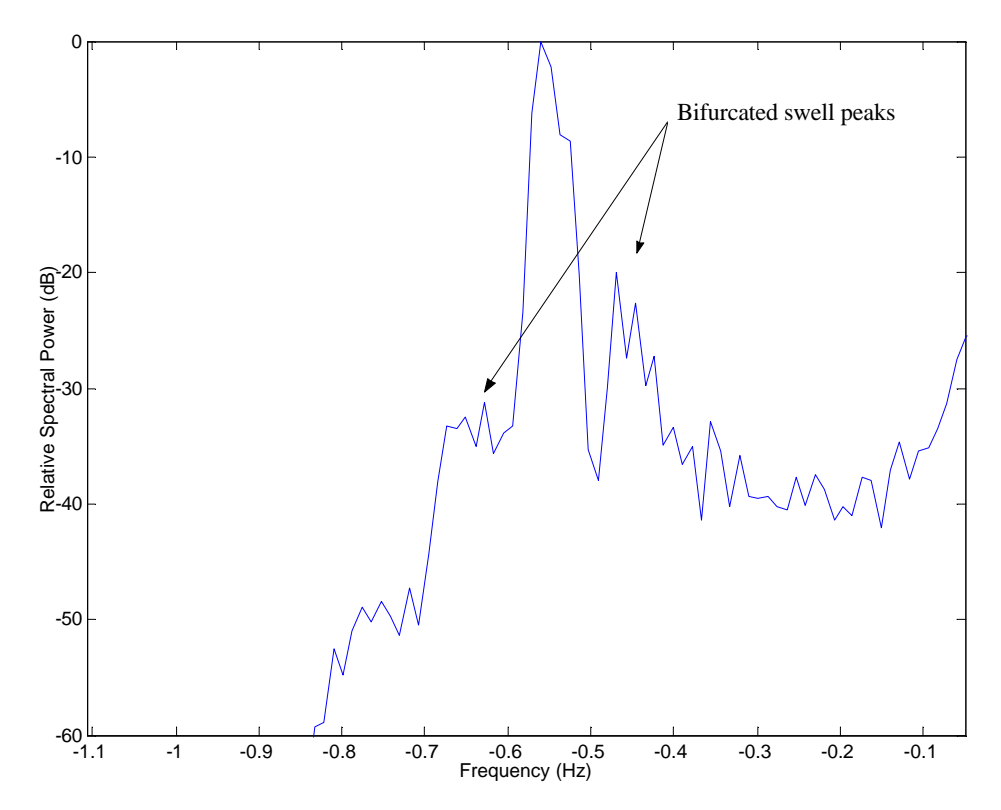


Figure 14: Example of bifurcated swell peaks. The true position of the swell peak is likely to be somewhere in between the two peaks in each case.

The weighted mean routine changes the frequency position of the selected swell peak according to the amplitude of nearby data points. An array of 7 data points is used, 3 points each side of the identified swell peak. The position is altered by,

$$\overline{x} = \frac{\sum y_i \left( x_i - x_m \right)}{\sum y_i} \tag{16}$$

where  $\bar{x}$  is the required frequency shift resulting from the calculation and  $x_i$  and  $y_i$  are the respective frequency and amplitude positions of the data points in the array.  $x_m$  is the mean frequency position in the array, this is the original position of the identified swell peak as it is the centre point in the array. The nature of a weighted mean routine allows it to be applied indiscriminately because if the peak is well defined and roughly symmetrical, the process will not change the position of the peak. Hence, this routine is a very robust processing tool. Figure 15 is a good example of a broad swell peak that has been processed using the weighted mean routine. Although the swell peak on the left hand side of the Bragg line is broad, it is also relatively symmetrical and has therefore not been changed by the weighted mean routine. The peak on the right hand side of the Bragg line is broadened asymmetrically and has been significantly shifted by the routine.

The second method employed to control swell peak interference relies on the fact that swell peaks should theoretically be positioned equal distances from their respective Bragg peak, (Stewart, 1971). The routine does not repair affected peaks but removes severely affected swell peaks from further involvement in calculations of swell wave parameters. Analysing this aspect of each spectrum is carried out by finding the displacement of each swell peak away from its respective Bragg peak and calculating the mean displacement. Reasonable limits of allowable displacement can then be imposed by applying a limiting factor that is determined empirically. Limits that excluded poor results due to broadened or bifurcated peaks were found to be at approximately  $\pm 20\%$  of the mean. Peaks inside these boundaries were utilized in the calculation of swell peak parameters. Peaks outside these boundaries were discarded. Once these procedures have been carried out, we are able to submit accurate swell peak information for extracting information from the second-order spectrum.

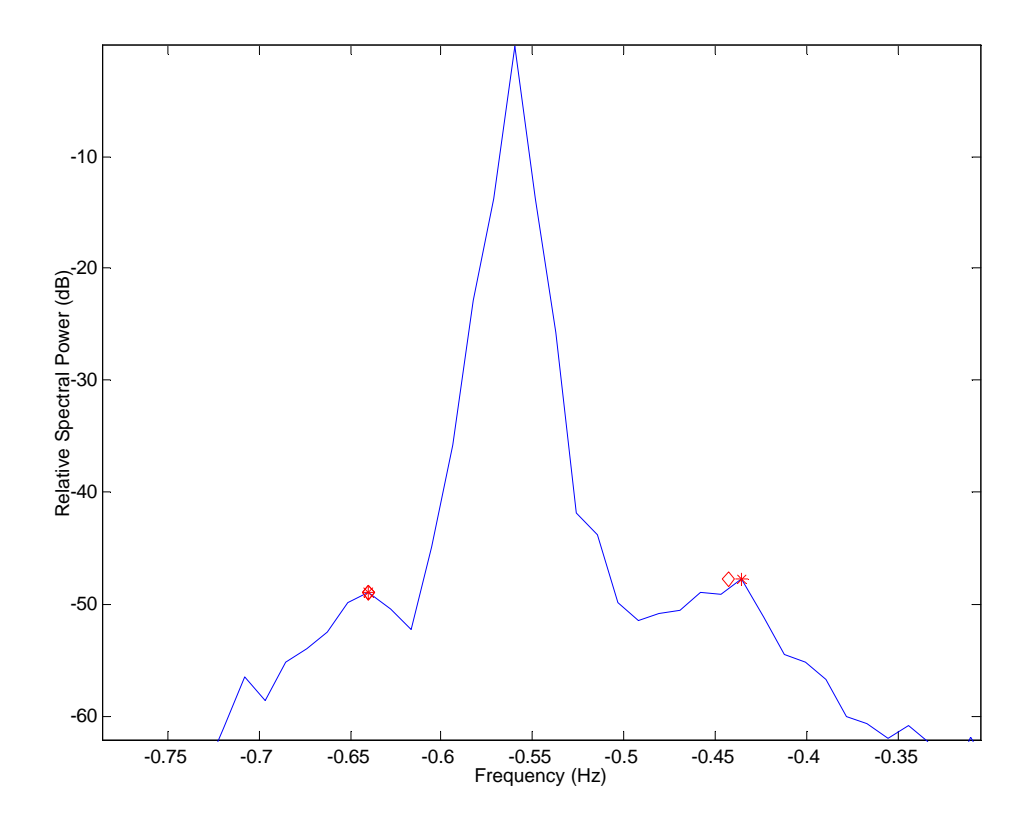


Figure 15: Example of the weighted mean routine as applied to a pair of broad swell peaks. The asterisk marks the original position and the diamond marks the corrected position.

# 4.3 Applying Second-Order Solutions

Barrick (1972) considered a total wave spectrum as the sum of a continuous high frequency wind wave spectrum  $S_w(\tilde{k})$ , with wave vector  $\tilde{k}$ , and a swell component that is generated at a large distance as an impulse function. This gives,

$$S(\tilde{k}) = S_w(\tilde{k}) + H_s^2 \mathbf{d}(\tilde{k} - \tilde{k}_s)$$
(17)

where  $H_s$  is the rms swell height and  $\tilde{k}_s$  is the swell wave vector with magnitude  $k_s$  and propagation angle  $q_s$  with respect to the radar beam. d is the width of the second-order swell peak. When this spectrum is substituted into a standard radar cross section integral equation, a relation is derived that separates the wave spectrum into a

continuous wind-wave spectrum with cross-spectral terms due to interactions between wind waves and swell, and swell interacting with swell.

Following this understanding, mathematical solutions for the extraction of swell wave parameters were soon developed (Lipa and Barrick, 1980) and are shown below.

$$k_s = \left(\frac{1}{16g}\right) (\Delta \mathbf{w}^+ + \Delta \mathbf{w}^-) \tag{18}$$

where  $\Delta \mathbf{w}^{\pm}$  are the radian frequency displacements between swell peaks surrounding the approaching and receding Bragg lines;  $k_s$  is the swell wave number and g is the gravitational constant.

$$T_{s} = \frac{2\mathbf{p}}{\sqrt{gk_{s}}} \tag{19}$$

where  $T_s$  is the swell wave period and  $\mathbf{q}_s$  is the swell wave direction with respect to the look direction of the radar beam given by

$$\mathbf{q}_{s} = \cos^{-1} \left( 8\mathbf{w}_{B} \frac{(\Delta \mathbf{w}^{+} - \Delta \mathbf{w}^{-})}{(\Delta \mathbf{w}^{+} + \Delta \mathbf{w}^{-})} \right). \tag{20}$$

 $\mathbf{w}_{B}$  is the Bragg frequency, which is dependent on the transmitted electromagnetic wave frequency.  $H_{s}$ , the rms swell wave height, is given by

$$H_{s} = \left(\frac{R_{m,m'}}{2\left|\Gamma_{m,m'}\right|^{2}}\right)^{1/2} \tag{21}$$

and contains m and m' which are simply indices,  $\pm 1$ , for the identification of individual swell peaks and their position in relation to the approaching or receding Bragg line.  $R_{m,m'}$  is the first to second-order peak ratio and  $\Gamma_{m,m'}$  is the combined coupling coefficient earlier denoted as  $\Gamma_T$ .

#### **4.3.1** Direction of Swell Wave Propagation

The direction given by the developed algorithm requires a series of corrections to be applied before the results are in a form comparable with that of the QBPA wave buoy data. The angle given by the algorithm is in a trigonometric form that needs to be

converted to a compass bearing or the results would be consistently 90 degrees adrift. Initially the direction is corrected for the 'look direction' of each sector i.e. the angle away from the bore sight. The COSRAD system extends its sweep 30 degrees to each side of the bore sight, therefore the two extreme sectors on each side need to be corrected by approximately  $\pm 30^{\circ}$ . This then needs to be corrected again to compensate for the bore sight of the radar to give the true direction of wave propagation. The bore sight ( $\theta_{bore}$ ) for Tallebudgera and Kingscliff are  $99^{\circ}E_{True}$  and  $21^{\circ}E_{True}$  respectively. Notice this makes the intersection of the radar beams close to orthogonal in overlapping areas, in order to maximise the ability to resolve directional vectors.

Hence, the correction is as follows:

$$\theta_{\text{compass}} = 90 - \theta_{\text{deg}} \pm \text{sector\_correction} + \theta_{\text{bore}}$$
 (22)

where,  $\theta_{deg}$  is the angle given by equation 20 and converted from radians to degrees,  $\theta_{bore}$  is the relevant bore sight angle in degrees East depending upon the station.

However, in addition to these necessary corrections, there is again an inherent ambiguity due to the cos<sup>-1</sup> term in Equation 20. As is the case with the extraction of wind direction, the algorithm cannot determine which side of the radar beam is the correct direction (Figure 16). Of course the calculation of wind direction relies on first-order Bragg peaks which are invariably present in the spectrum and relatively reliable in comparison to second-order structures. Hence, the complete coverage of wind values allowed for a simple comparison between the two stations to resolve the ambiguity. The increased number of contaminated peaks in the second-order, results in a reduced coverage of directional values. It is then often impossible to compare the two stations to resolve the ambiguity because all four directional values, positive and negative values for both stations, must be available for the comparison to work.

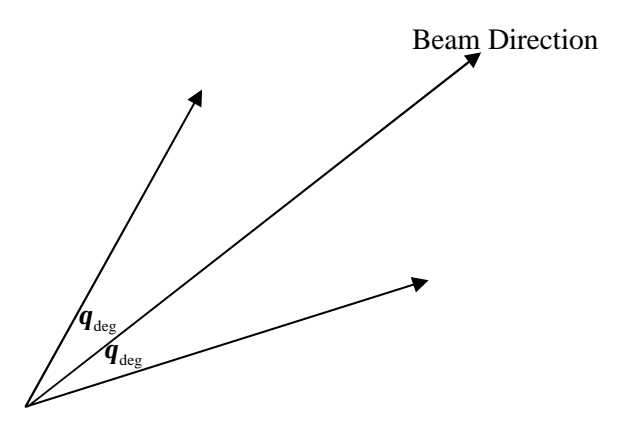


Figure 16: Graphically shows the inherent ambiguity in the calculation of direction.

Due to the inability to resolve the ambiguity problem using a 'comparison of pairs' method, another approach was taken that examines the trend of each set of directional values. The directions produced by the correct side of the beam should result in an almost constant set of values to match the trend of the wave buoy throughout the day. As shown in Figure 17,  $q_{pos}$  and  $q_{neg}$  are calculated as below:

$$\mathbf{q}_{pos} = Beam + \mathbf{q}_{deg} \tag{23}$$

$$\mathbf{q}_{neg} = Beam - \mathbf{q}_{deg} \tag{24}$$

 $q_{pos}$  and  $q_{neg}$  were calculated for each station in two hour intervals for March 5 in order to show any trends. The average swell direction resulting from each sector was found and plotted against the beam direction. At this stage any dependence upon the beam direction should now have been removed and the correct result should show a gradient close to zero. If a positive gradient is found, as in Figure 17, we must assume that the beam direction has not been successfully removed from the resulting direction of swell. The trends for all four situations show a significant increase with increasing beam direction. This shows that the effect of beam steering has not been removed from the data and raises concerns over the output resulting from the Barrick algorithm. If the algorithm is producing results correctly it would be expected that  $\Delta w^+$ ,  $\Delta w^-$  and therefore  $oldsymbol{q}_{ ext{deg}}$ , would show a dependence on beam steering that would require correction to produce the correct wave direction. If  ${m q}_{
m deg}$  is independent of beam steering position then  $\Delta w^+$  and  $\Delta w^-$  are also independent of beam steering position which suggests the algorithm may not be performing adequately to provide usable wave parameters. To test if this dependence exists, firstly a plot of  $extbf{\emph{q}}_{ ext{deg}}$  against beam position was created (Figure 18). As suspected this shows no dependence of  $q_{
m deg}$  on beam position.  $\Delta \mathbf{w}^+$  and  $\Delta \mathbf{w}^-$  were then plotted against beam position, (Figure 19), to confirm that there is no significant variation across the sweep. This is also confirmed statistically as follows,  $\Delta \vec{w}^+ = 1.08$  and  $\Delta \vec{w}^- = 1.13$  with  $s^+ = 0.042$  and  $s^- = 0.052$ . The SEM<sup>+</sup>=0.11 and SEM<sup>-</sup>=0.13 shows no significant variation across the sweep.

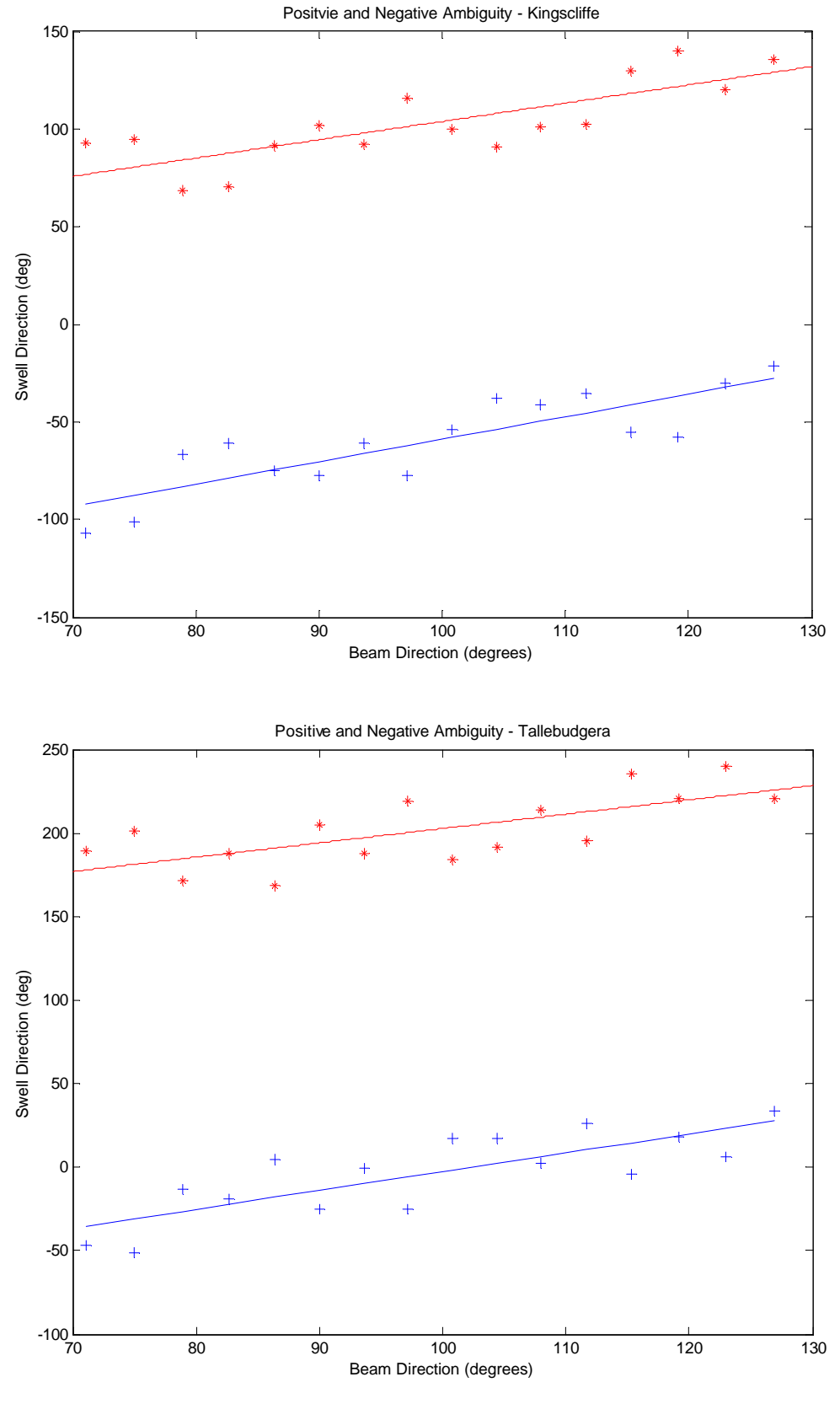


Figure 17: Positive(\*) and negative(+) sides of the ambiguity for both Tallebudgera and Kingscliff stations. Both stations display a positive gradient for both sides of the beam.

#### 4.4 Discussion

This test of the ability to use Barrick's algorithm on data acquired by the COSRAD system, has proven unsuccessful. The theory upon which the algorithm is based is mathematically valid however it would require high resolution data even in the second-order continuum in order to resolve the relatively fine variations in swell peak positions. This test was conducted on a sample set of data from the Tweed Heads deployment which represented the strongest swell wave conditions. Even though second-order peaks were present and routinely identifiable in the power spectrum, the fine scale variations in their peak frequencies was beyond the working parameters of the radar for this deployment. The primary function of the COSRAD system is the monitoring and mapping of surface currents over a vast area of the ocean surface. The operating parameters for this purpose however are not optimal for the extraction of second-order information. The purpose of this project is to extend the capabilities of the system so that the functionality of its primary role in mapping surface currents is unhindered and useful information on the long wave portion of the ocean wave spectrum is provided as an additional benefit.

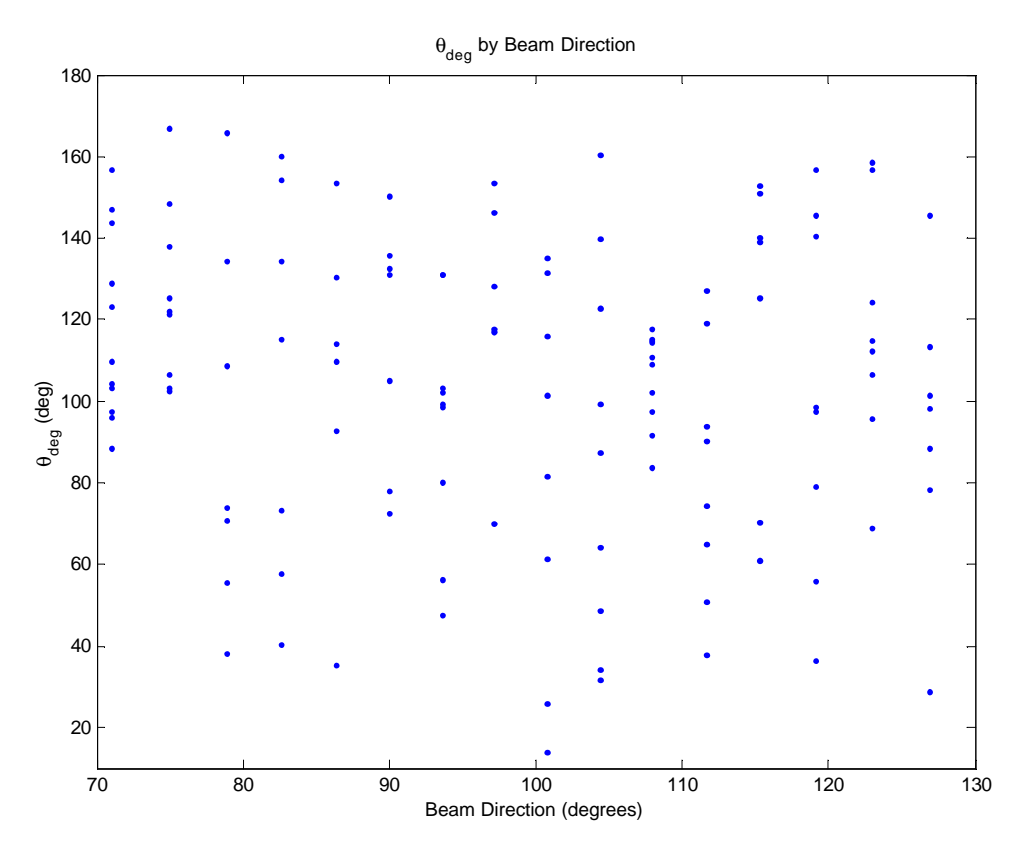


Figure 18:  $\theta_{deg}$  shows no dependence on beam direction and hence extraction of swell direction is not attainable by this method. (March 5, Tallebudgera station).

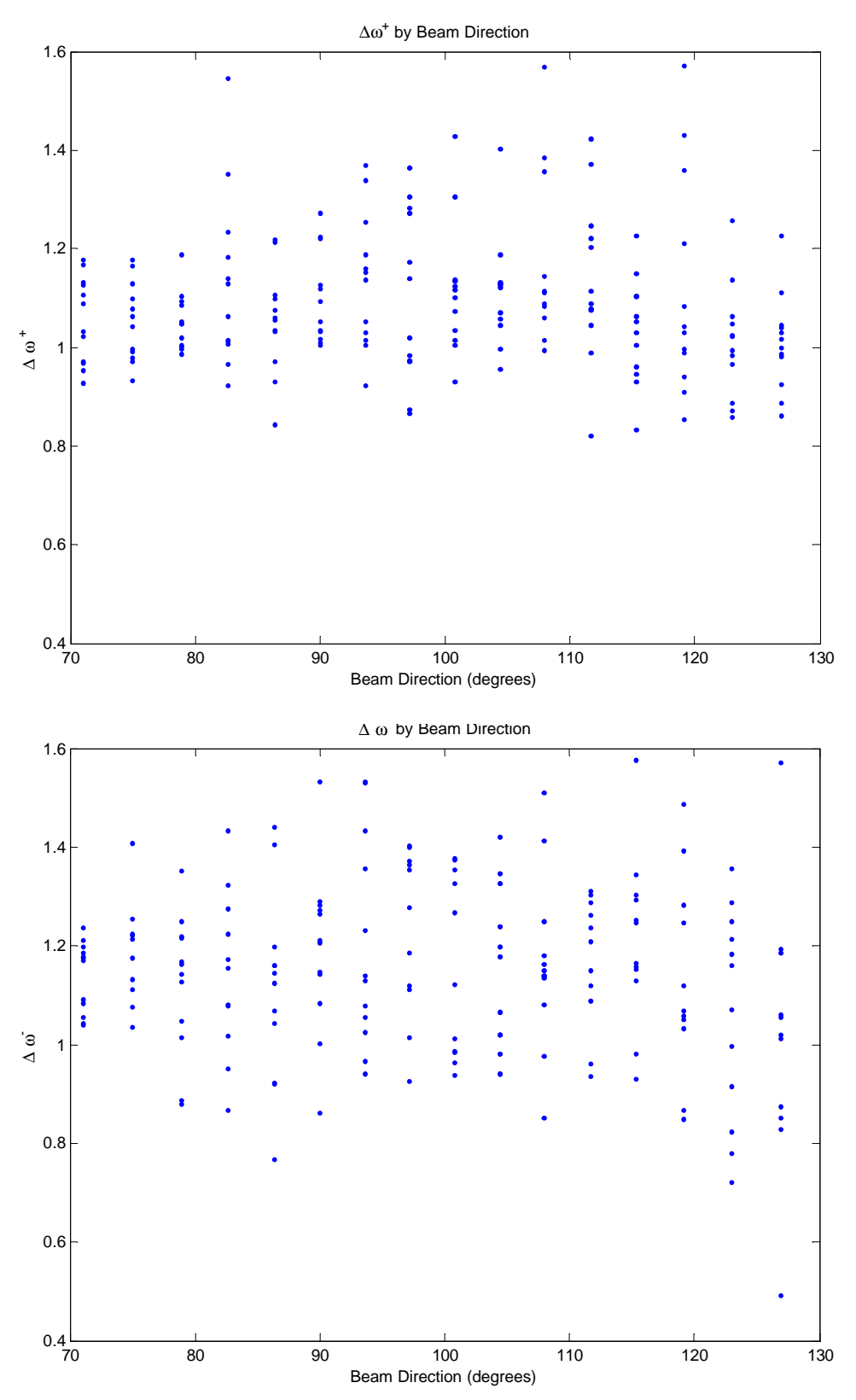


Figure 19:  $\Delta w^+$  and  $\Delta w^-$  show no dependence on beam steering position and therefore it is not possible to extract swell direction using from the COSRAD data using this method. (March 5, Tallebudgera station)

# **Chapter 5: Swell Wave Parameter Extraction Algorithm**

# 5.1 Frequency Modulation of the Radar Echo

As mentioned previously, the main scattering mechanism for ocean radar backscatter is Bragg scattering from the surface wave which is propagating either towards or away from the radar with a wavelength half that of the radar wavelength. For the HF COSRAD system the operating frequency is 30 MHz and the Bragg wavelength is 5 m. The second-order echo in the Doppler spectrum is a manifestation of a double-scatter effect in which two ocean waves simultaneously interact in the scattering process (Barrick, 1977). The method described in this chapter relies on a single scatter approach to extract wave information from the second-order spectrum. When there is an underlying swell the smaller Bragg waves are thrust to and fro by the faster moving, longer wavelength swell waves. Therefore at any given point on the ocean surface the velocity of the Bragg wave is determined by the propagation of that wave itself and the

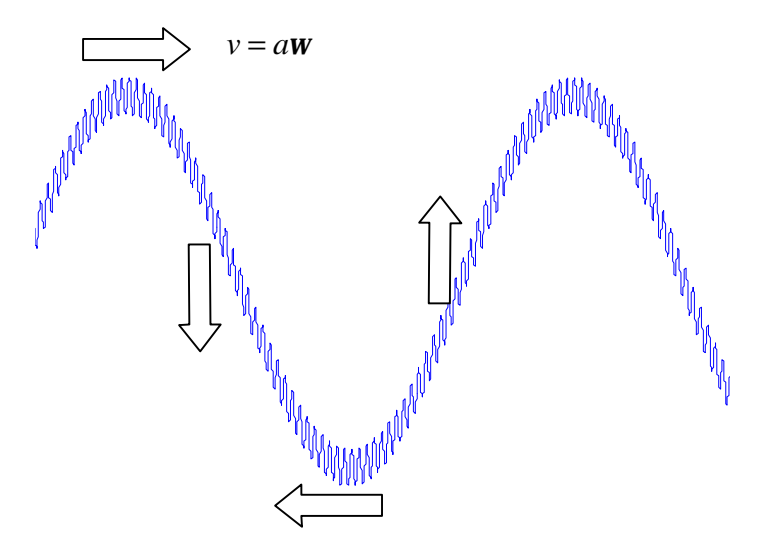


Figure 20: Schematic of a two-scale system with a short wavelength Bragg wave riding on a swell. The arrows show the instantaneous velocity of the surface water particles in response to the swell wave. The surge velocity of the swell wave modulates the instantaneous velocity of the Bragg wave and when the radar wave backscatters, the echo is frequency modulated.

surge velocity imposed by the swell. We assume that these velocities are linearly superposed as illustrated in Figure 20.

The instantaneous surge velocity of a portion of water at the surface, illustrated in Figure 20, is

$$v_{s} = a_{s} \mathbf{W}_{s} \tag{25}$$

where  $a_s$  is the amplitude of the swell wave, and  $\mathbf{w}_s$  is the frequency. In deep water the trajectory of the surface particle of water is a circle in the vertical plane. The horizontal component of the surge velocity is

$$v_{SH} = a_s \mathbf{w}_s \cos(\mathbf{w}_s t) \tag{26}$$

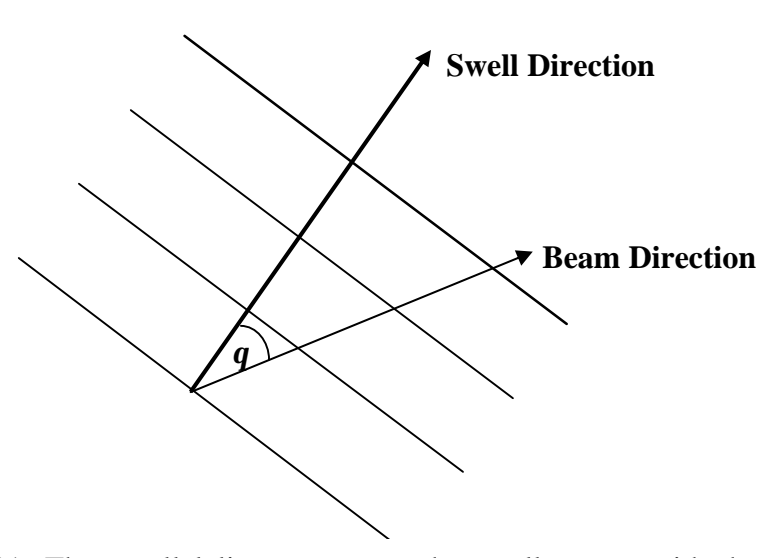


Figure 21: The parallel lines represent the swell crests, with the wave propagating perpendicular to these. The radar beam can be directed at any angle  $\boldsymbol{q}$  to the swell and the surge velocities are projected through  $\boldsymbol{q}$ .

If we were now to consider the swell surge velocity in a direction q from the direction of propagation of the swell, then it is a simple projection as shown in Figure 21, and the horizontal component is expressed as

$$v_{SH} = a_s \mathbf{w}_s \cos \mathbf{q} \cos(\mathbf{w}_s t) \tag{27}$$

The propagation velocity of the Bragg wave is

$$v_B = \sqrt{\frac{gc}{4\boldsymbol{p}\,f_0}}\tag{28}$$

so the combined velocity which modulates the radar backscatter is

$$v_M = v_B + v_{SH} \tag{29}$$

The Doppler frequency imposed on the backscattered echo then becomes

$$f_D = \sqrt{\frac{gf_0}{\boldsymbol{p}c}} + \frac{2f_0}{c} a_s \boldsymbol{w}_s \cos(\boldsymbol{w}_s t)$$
 (30)

and the echo signal may be written

$$E(t) = a_B \cos\left\{\mathbf{w}_B t (1 + m\cos(\mathbf{w}_s t))\right\} \tag{31}$$

where

$$m = \frac{\mathbf{W}_B a_s \mathbf{W}_s}{g} \cos \mathbf{q} \tag{32}$$

 $a_B$  is the amplitude of the Bragg echo and  $\mathbf{w}_B$  is the Bragg frequency as defined in equation 5.

The expression for E(t) represents Frequency Modulation and the corresponding spectrum is a series of Bessel functions when the modulating function is a monotonic sinusoid, as used here. For a small modulation index the spectrum is dominated by the carrier which in this case is the first-order Bragg line, and the first pair of side lobes with relatively minor contributions from the higher order sidebands. Spectral amplitudes corresponding to E(t) can be calculated for any set of two-scale parameters. Figure 22 shows calculated spectra for a test study carried out using conditions encountered during the Tweed Heads deployment of the COSRAD system.

From the radar spectra the measurement of the ratio ( $R_{swell}$ ) of first-order Bragg amplitude to the mean amplitude of the first sidebands is simple to calculate and would be a reliable and robust parameter to extract.  $R_{swell}$  is a minimum when the radar beam points in the direction of swell ( $\mathbf{q} = 0$ ) and is infinite when the beam points orthogonal to the swell direction. This is due to the fact that in this configuration there is no component of modulation from the surge velocity of the swell in the direction of the radar beam and the sidebands are non-existent. Based on this approach it should be possible to determine the direction of swell wave propagation by comparing data from the radar with this two-scale analysis.

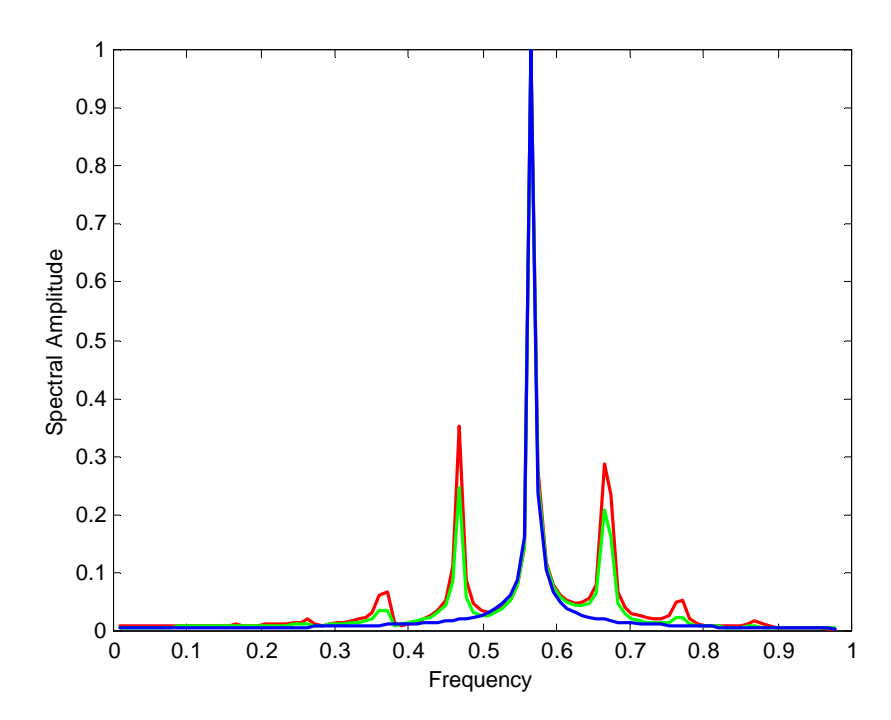


Figure 22: Spectra calculated using the two-scale model.  $\mathbf{q} = 0$  produces the strongest sidebands. The weaker sidebands present are produced when  $\mathbf{q} = 45^{\circ}$  and  $\mathbf{q} = 90^{\circ}$ . The amplitudes fit the case study for conditions on 5 March 2001 at Tweed Heads.

By calculating  $R_{swell}$  for a range of q values between 0 and 90 degrees a curve is generated with a minimum at q=0 and a maximum approaching infinity where  $q=90^{\circ}$ . This curve is shown in Figure 23 where it is mirrored about the minimum. Data collected from a COSRAD station during a single sweep will sit on a portion of this curve, its exact location being dependent upon the angle between the swell wave direction and the mean radar beam direction. Due to the sweep of a single COSRAD station covering only a 60 degree portion of the ocean surface it is possible that the sweep may not look in the direction of, or orthogonally to, the swell direction. However, with this analysis it is not imperative that the radar sweep includes a sector that intersects the swell wave propagation at 0 or 90 degrees because the swell direction can be found by shifting the curve to fit the radar data and hence finding the direction at which the curve reaches a minimum. Before continuing to detail the fitting process more attention needs to be given to the extraction of  $R_{swell}$  from real radar spectra.

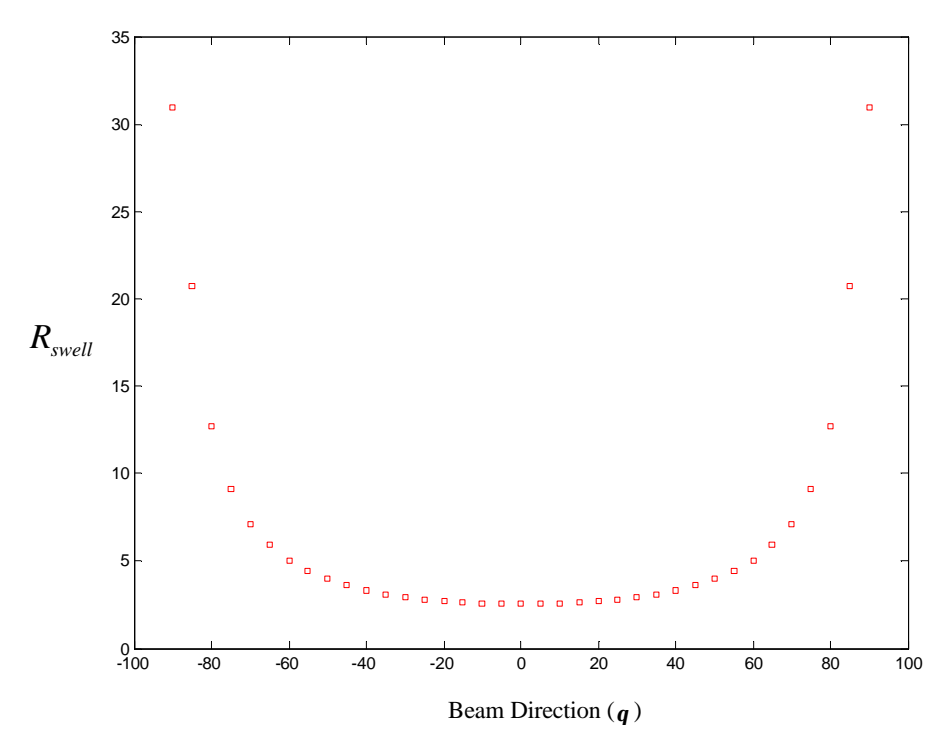


Figure 23: Theoretical ratio data from frequency modulation model of Bragg and swell waves.  $R_{swell}$  is the ratio of power in the first-order spectrum to the average adjacent swell sideband power.

As discussed previously the swell peaks surrounding each Bragg peak are a result of the frequency modulation imposed upon the higher frequency Bragg waves by the lower frequency swell waves as they pass through. The sidebands are also affected by the electromagnetic interaction of the radio wave with the ocean surface. This will be discussed in more detail shortly. The frequency modulation relationship can be quantified by comparing the strengths of the swell peaks in the frequency spectrum to the strength of the relative Bragg peak. This comparison has been calculated using two methods. The first method used mainly for its simplicity and reliability is to compare the absolute peak power values which are generally easily obtainable and easily compared. The second method compares the area enclosed by the Bragg peaks to the area enclosed by the swell peaks. This method is slightly more involved as the peaks' boundaries must be defined in order to set limits to the calculation of the area. The ratio

is calculated by dividing the Bragg peak power or area by the swell peak power or area. For the small modulation indices that we are dealing with, this should always result in a ratio greater than 1 as the expression of swell in the frequency spectrum as a second-order feature should not contain more energy than the first-order Bragg peak. Note that at high modulation indices the sidebands can be greater than the carrier. Each method is examined in more detail below, with the results from each method compared using the two-scale analysis.

### 5.2 Peak Power Ratios

This is by far the simpler of the two methods and the process benefits from this greatly by not requiring empirically set limits to define a peaks area of coverage. There are very few occasions when the peak finding algorithm chooses an incorrect swell peak and therefore the only possible weakness in the method is inherent noise in the spectrum. Higher ratios are generally produced when bifurcated or broadened swell peaks are used in the calculations. When a peak is bifurcated the peak power is usually reduced but the peak increases in width to compensate for the energy lost in amplitude, as shown in Figure 24. The impact on the results due to these artefacts is particularly difficult to detect when they occur on the edges of a sweep. High ratios at the beginning or end of a sweep can be fitted to the two-scale model as it increases towards infinity. This will shift the swell direction and amplitude significantly from the correct value and will not be detected without manually examining the originating spectra which removes the automated advantage of developing the algorithm. To reduce the impact of these artefacts on the results, the ratios are calculated using the dominant side of the Doppler spectrum only. In most cases one Bragg peak is significantly stronger than the other and less susceptible to bifurcations and peak broadening. Selectively choosing data with an increased signal to noise ratio minimizes the number of high ratios due to noise.

Considering a situation where one of the swell peaks is bifurcated, and is reduced in peak power as a result (Figure 24), a higher than expected ratio will be produced. To reduce this effect, the ratio is calculated using the average peak power of the bifurcated

peak and the opposite unaffected swell peak. An elevated ratio may still be produced however it will be much closer to the expected value than the alternative.

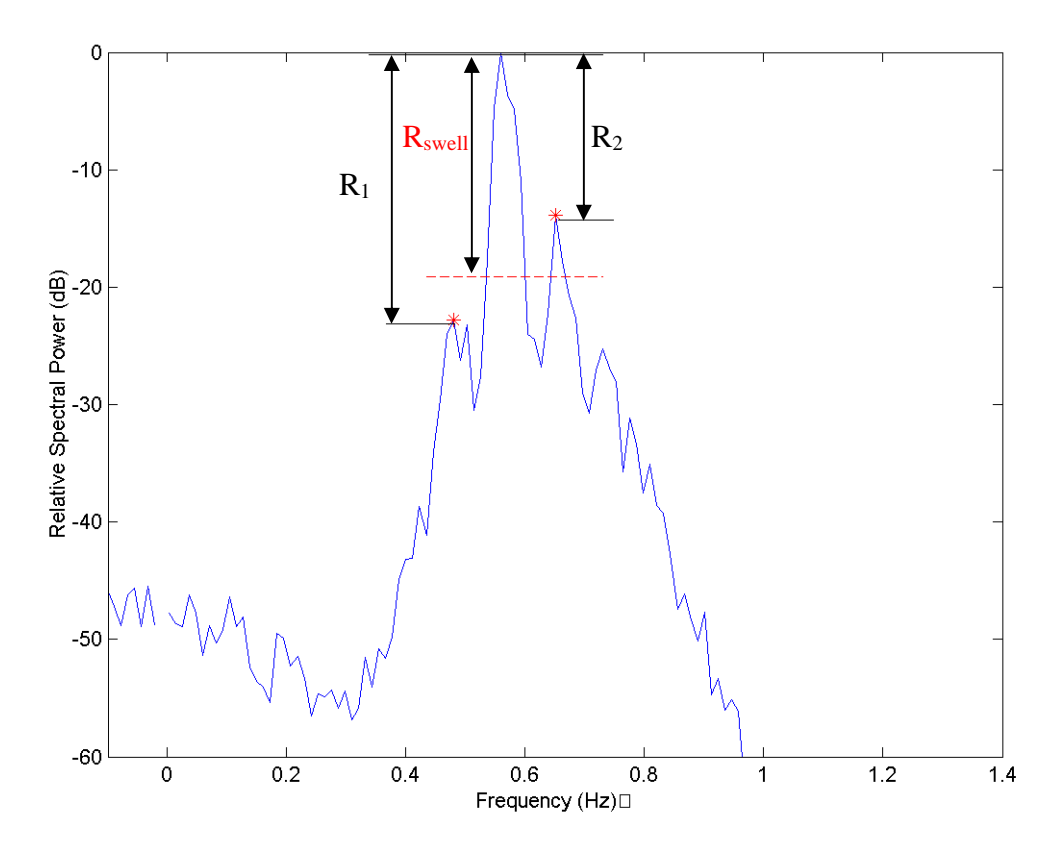


Figure 24: The left swell peak is bifurcated and lower in power as a result. The average ratio is calculated to reduce the impact of the noise on the results.  $R_{swell} = \frac{(R_1 + R_2)}{2}$ 

To highlight the effectiveness of these processes Figure 25(a) shows a manual fit of sample radar data and the two-scale model. The radar data in this case is a selection of ratios calculated from the positive side of the Doppler spectrum only. The positive side however does not always contain the dominant Bragg peak across the sweep. The first few spectra in the sweep have a dominant Bragg peak on the negative side of the Doppler spectrum. Hence, the ratios calculated from the positive side in this part of the sweep are high and drag the fit to the synthetic data across to 155 degrees. In Figure 25(b) the ratios are calculated from the dominant Bragg peak only and show greatly reduced ratios for the first few points in the sweep. A higher degree of confidence can

be assumed for these new ratios and for the fit to the synthetic data. The resulting direction is shifted to 140 degrees.

Averaging the peak power for the two chosen swell peaks may improve the stability of the estimate. This averaging also serves a purpose of reducing the effects of double scatter which will be discussed later.

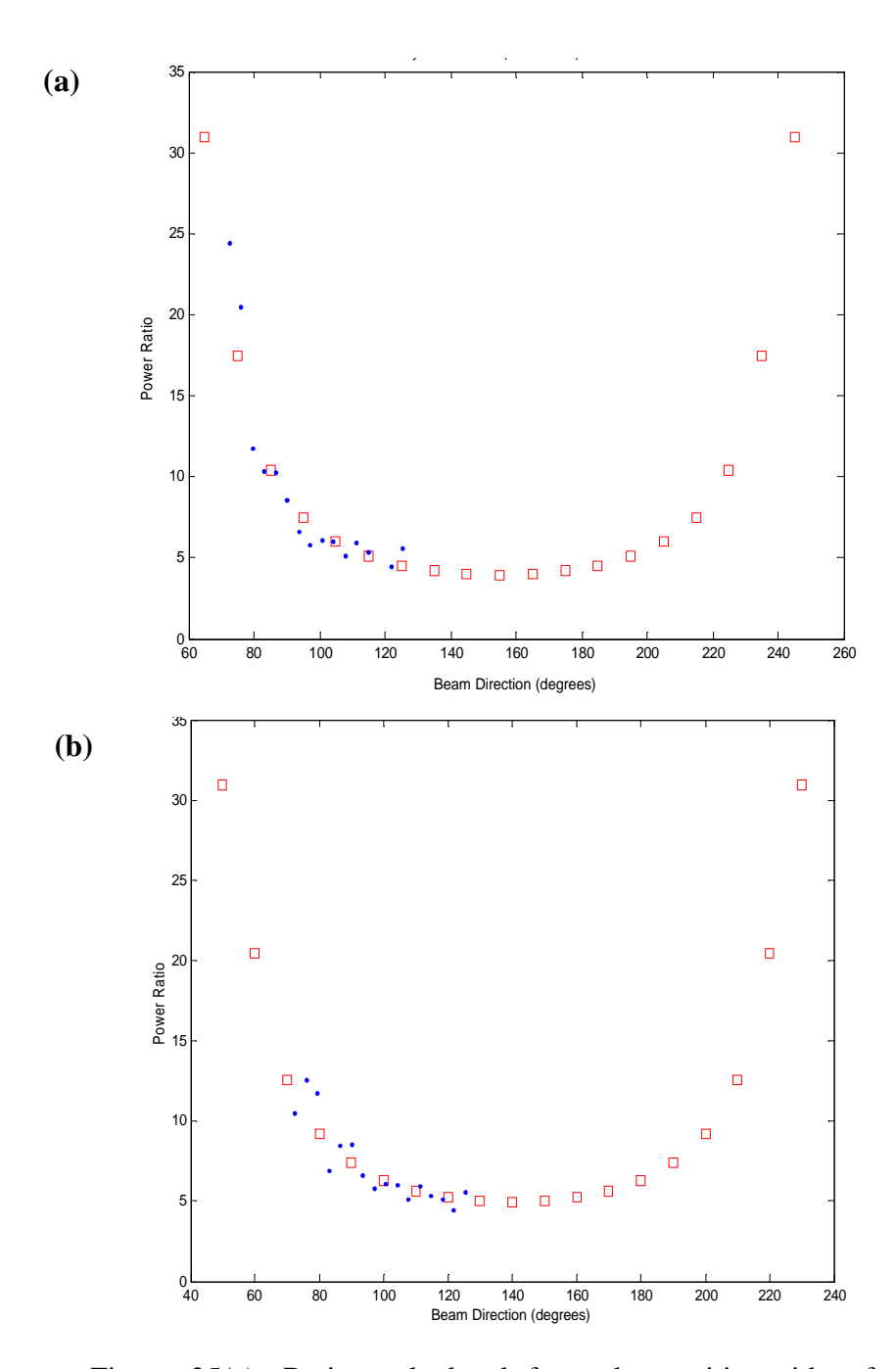


Figure 25(a): Ratios calculated from the positive side of the Doppler spectrum only (?), fitted to the theoretical data (?). Swell direction = 155 (b) Ratios from the dominant side of the spectrum hence removing high ratios from weaker parts of the spectrum. Swell direction = 140

### 5.3 Peak Area Ratios

The area under a swell or Bragg peak requires the identification of a peak's width or location of the nulls on each side. As discussed above this can become increasingly difficult as you move further away from the Bragg peak and various assumptions must be made that may vary between data sets and even within data sets that span long periods of time. Once the end points of a peak have been identified there are a few differing methods that can be utilised to determine the enclosed area. One method is to fit a curve through the three known points, the two nulls and the peak. However this can be extremely inaccurate as a quadratic equation cannot describe the shape of a peak in enough detail and overestimates the area in most cases as in Figure (26). Simpson's rule provides a better estimate of the area enclosed by the peak. Simpson's rule fits a curve at each frequency step within the defined limits of the peak rather than fitting just one curve over three points, thus increasing the accuracy of the area estimation greatly. Simpson's rule is of the form,

$$\int_{a}^{b} f(x)dx \approx S_{n} = \frac{\Delta x}{3} [f(x_{0}) + 4f(x_{1}) + 2f(x_{2}) + 4f(x_{3}) + \dots + 2f(x_{n-2}) + 4f(x_{n-1}) + f(x_{n})]$$
where  $n$  is even and  $\Delta x = (b-a)/n$ . (33)

The area of the Bragg peaks and swell peaks are calculated individually and then used to calculate the ratio. It is reasonable to assume that this method of ratio calculation should be more reliable and robust than using absolute peak power due to compensations made in the area of a peak that has been broadened or bifurcated. Although the peak power is often reduced in these instances, the peak width increases and therefore the resulting area should not suffer. However, this method is reliant on the accuracy of the defined limits of the peak and in situations where bifurcations are present accurately defining the limits also suffers. If the spectrum in the region of the second-order is significantly affected by bifurcations then the defined nulls may be incorrectly identified making the width of the peak to great or too small. In this respect the calculation of the Bragg to swell ratio using the area enclosed by the peak can produce increased scatter. Unlike the power method, it is difficult to implement

mechanisms to reduce the scatter because of the unpredictability of the errors. With the power method it is reasonable to assume that a higher than expected ratio will be produced when confronted with noise affected spectra, however the scatter produced by the area method depends upon the placement of the nulls which can be affected by relatively minor noise spikes resulting in either shortened or increased peak width.

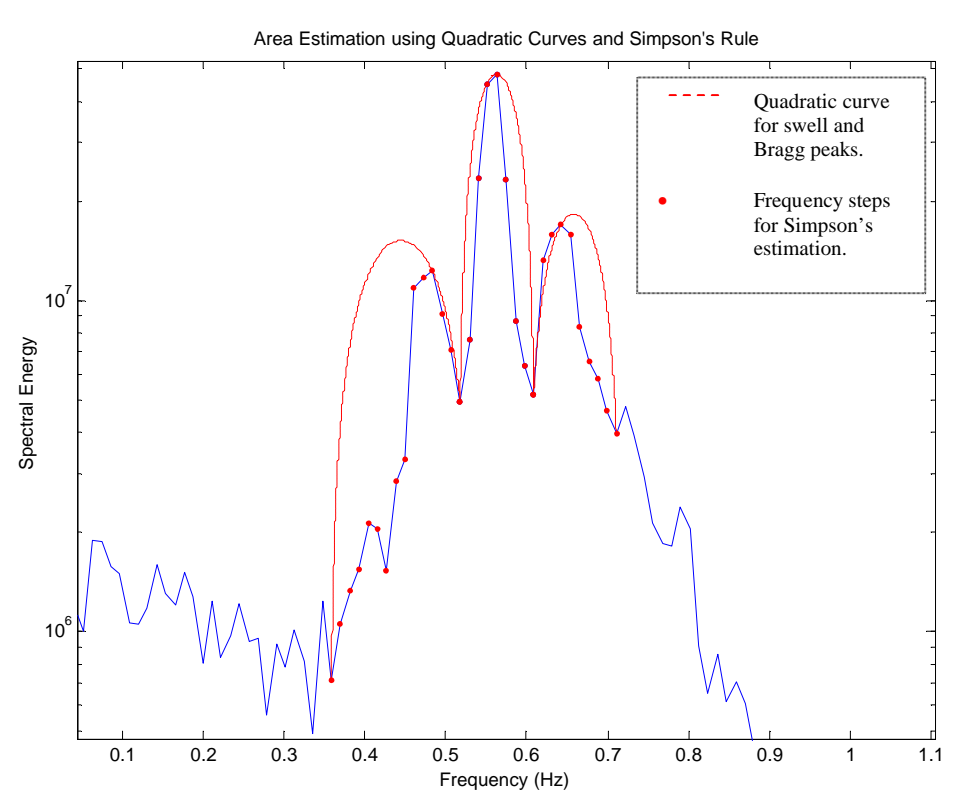


Figure 26: The dashed line shows the exaggerated quadratic estimation of the peaks using a three-ponit fit. The filled circles show the intervals over which Simpson's rule estimates the peaks.

### 5.4 Automated Fitting Routine for Swell Height and Direction

Having found the most reliable method of extracting  $R_{swell}$  the next step is to develop an automated method of fitting the stylised curve data, obtained from the frequency modulation model, to the COSRAD ratios. An automated method would ensure a consistency in the results that would be difficult to achieve manually due to the subjectivity of the decision. Also, automation is ultimately a step towards an algorithm capable of operating in near real-time.

The fitting routine begins with the minimum of the model curve at 0 degrees on the abscissa, extending to  $\pm 90$  degrees in 5 degree steps. A number of parameters must be defined before the theoretical spectra can be calculated and analysed to produce these ratios. These parameters include the radar frequency,  $f_0$ , an estimation of the period of the swell,  $T_s$ , and an initial estimation of the swell amplitude,  $a_s$ . Given these parameters the model can produce a curve of ratios extracted from the calculated theoretical spectra. The estimation of  $a_s$  provides a starting point that is unlikely to be the correct swell amplitude. A problem then occurs due to slight variations in the resulting shape of the stylised curve with varying values of  $a_s$  therefore resulting in inaccuracies in the directional fit. Figure 27 shows a gradual increase in the power ratio values with decreasing values of  $a_s$ .

For this reason an iterative process is required in order to achieve the most accurate result for swell direction and amplitude. On the first pass a stylised curve will be calculated using a mid range value for  $a_s$  which is then fitted to the radar data to obtain a direction and new amplitude. These parameters will be close to the correct values but may be improved by recalculating a new stylised curve based upon this new amplitude value. The new curve will have a slightly different shape which may return a slightly different swell direction and amplitude after it has been refitted to the radar data.

In order to manipulate the position of the synthetic curve to fit the radar data, a polynomial must first be fitted to describe the curve. A tenth order polynomial was

found to be the minimum even order which gives a good fit to these curves depending upon the initial estimate of  $a_s$ . Ultimately, for a routine analysis algorithm, we can simply use the polynomial coefficients to represent the stylised curve.

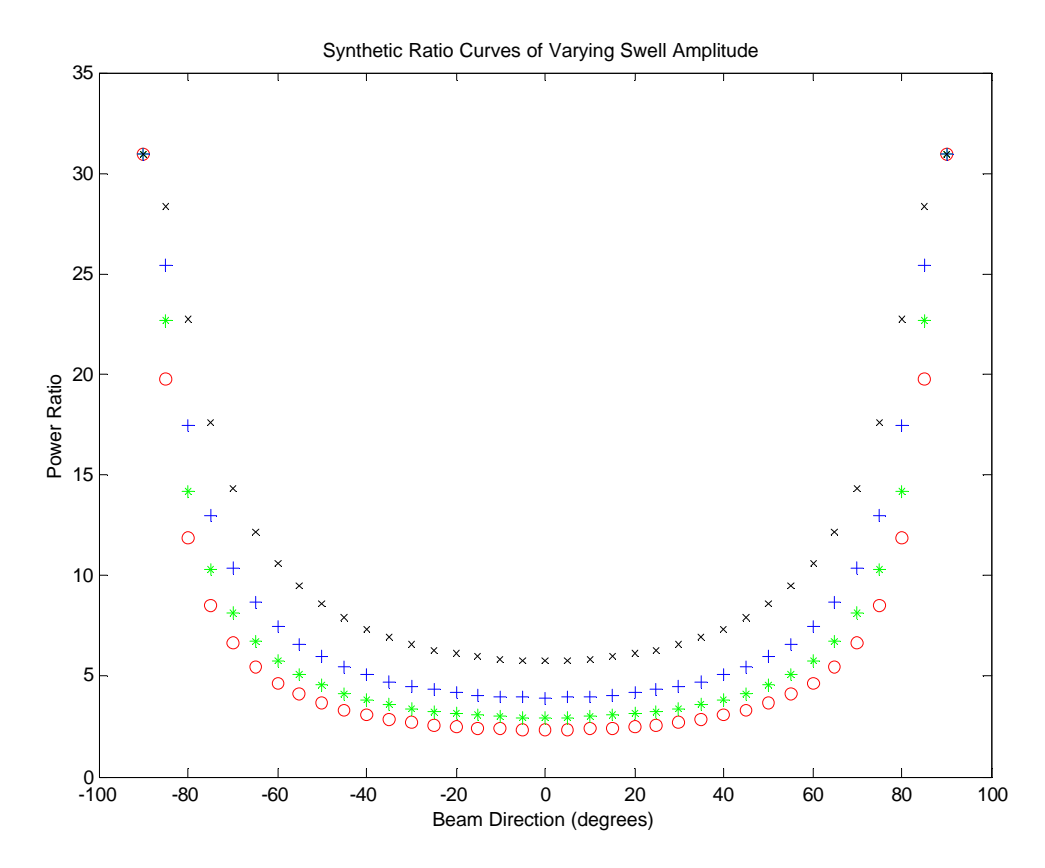


Figure 27: Shows the variation in resulting ratios with varying  $a_s$ . o represents ratios calculated using  $a_s = 0.02$ . \*,  $a_s = 0.016$ ; +,  $a_s = 0.012$  and **x**,  $a_s = 0.008$ . Note values of  $a_s$  shown here are not calibrated.

### **5.4.1 Directional Fitting**

Firstly the stylised curve is manoeuvred to provide a fit in the directional domain, along the x-axis. This is achieved by matching the gradient of the radar data to an appropriate portion of the stylised curve. The gradient,  $m_r$ , of a straight line of least squares through the radar data allows us to identify the appropriate portion of the stylised curve which will provide a good fit. The stylised curve is differentiated, as in Figure 28 and the value closest to  $m_r$  is identified. This process is simple and robust due to the monotonic shape of the differentiated curve. The required amount of displacement in the horizontal direction can then be found and the original stylised curve is moved until the gradients match at the centre of the radar data. At this point we can simply find where the minimum of the stylised curve sits on the directional axis to find the direction of swell wave propagation. It is then simply a matter of adjusting the amplitude so that the stylised curve fits in both dimensions. The vertical adjustment is performed by minimising the difference between the points.

During initial tests it was found that a single misplaced ratio, due to erroneous peak selection or noise affected spectra, could severely affect the directional component of the fitting routine. The nature of the shallow sloping curve means that minor variations in  $m_r$  have a considerable affect on the horizontal positioning of the stylised curve. This is of particular note when the adversely affected ratio lies at one of the ends of data set. When this is the case the resulting swell direction parameter can be up to 50 degrees from the correct position. To reduce the occurrence of producing obviously incorrect swell directions as a result of a small number of outlying ratios a simple routine to remove these outlying values from the set prior to the main fitting routine was implemented. When the straight line is fitted to the ratios derived from the radar data the standard deviation of all points about this line is calculated. Any points that then lie more than two standard deviations away from this line are then deemed to be unacceptable and are removed from the set. A straight line is then fitted to the remaining values and  $m_r$  is recalculated for further use in determining the swell wave direction. Figure 29 shows the two situations. Firstly (Figure 29a) where an outlying ratio is used in calculations giving an  $m_r$  value of -0.028 and a swell direction of 129 degrees which is approximately 25 degrees away from the corresponding wave buoy value. Figure 29b, shows the fitted data after this value has been removed giving an  $m_r$  value of -0.004 and a swell direction of 101 degrees which compares well with the wave buoy. Figure 29 does not show the effect of this removal of outliers on the fitting of the data in the amplitude domain. These outliers have a far smaller impact upon the calculation of the swell amplitude mainly due to the geometry of the stylised curve as mentioned previously. Minor changes in  $m_r$  do not drastically alter the vertical fit.

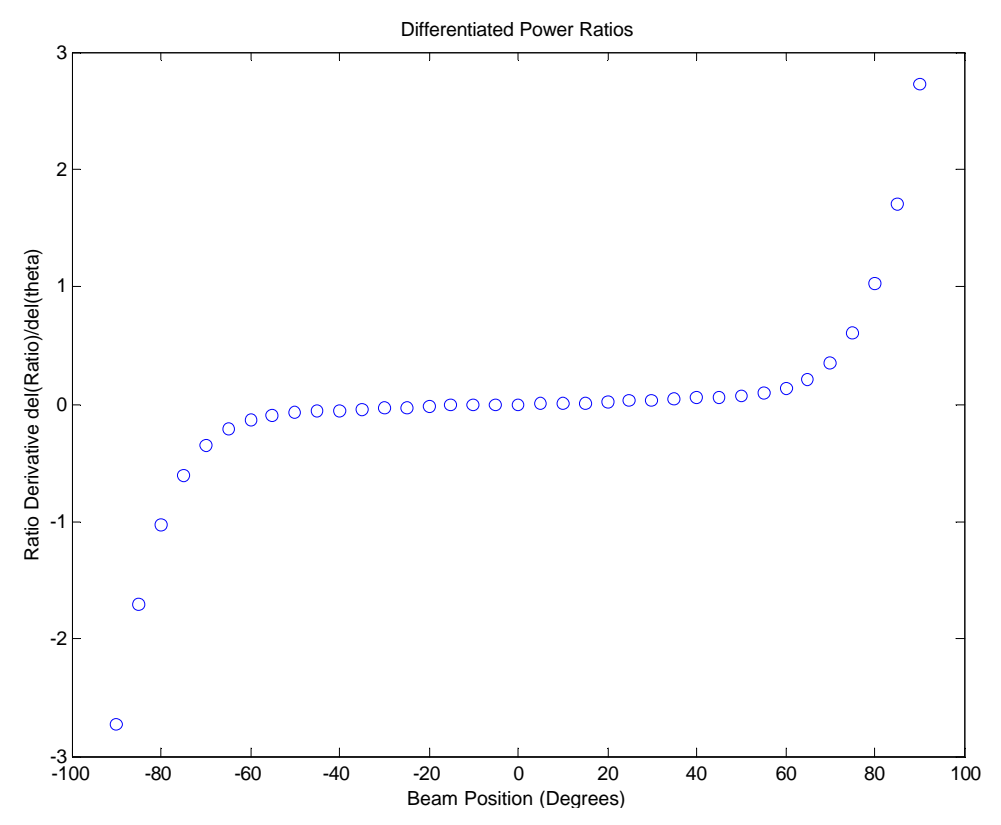


Figure 28: Differentiated stylised curve used to fit data in the directional domain. Its monotonic nature ensures a simple and robust analysis.

### **5.4.2** Vertical Calibration

It is important to note that the radar data integrates over area as opposed to single point measurements from in-situ directional wave buoys. It is then necessary to perform a calibration of the two different sets of data so that comparisons can be made. A calibration is required to scale these differences between the two techniques of ocean surface monitoring.

The  $a_s$  value involved in producing the frequency modulated spectra, from which the ratios composing the stylised curve are calculated, is an order of magnitude lower than the expected wave height values. A calibration factor is required to correct the scale of amplitude so that it produces results comparable to the wave buoy measurements. This calibration need only be carried out on one occasion throughout the deployment. The data point chosen for the calibration is taken from a period of strong swell where the results are most consistent and therefore the resulting calibration will be reliable. Specifically, the point chosen for the calibration will be producing results comparable to the wave buoy for both swell direction and period parameters proving that this point is providing accurate swell information.

This calibration can be performed at the beginning of a deployment and consistently applied to provide real-time results from this analysis technique. However, as in this case, the analysis is being applied after the deployment has been completed and therefore the calibration point can be chosen during a period of favourable swell wave activity.

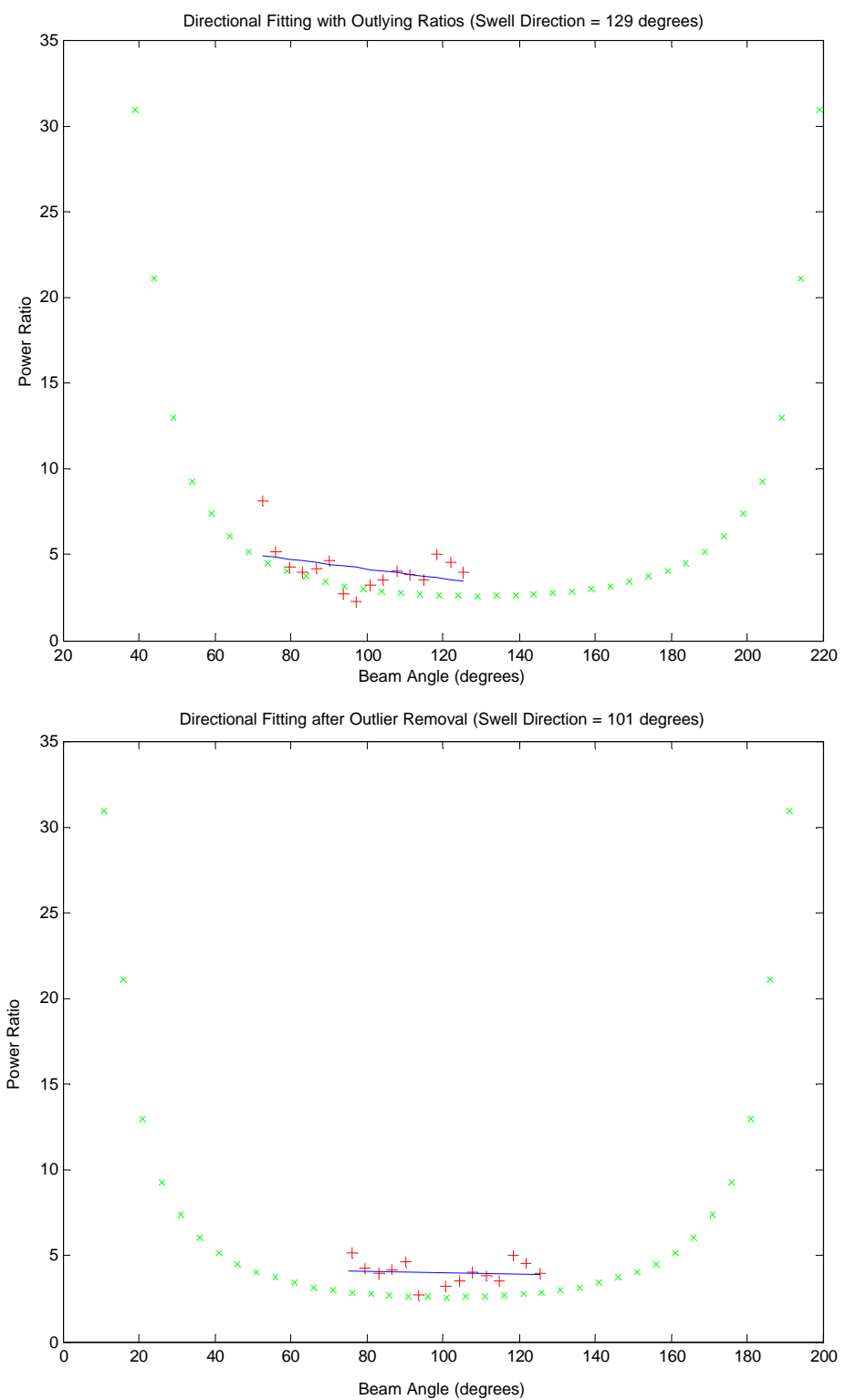


Figure 29: + = radar data, x = synthetic data (a) The first data point artificially increases the gradient,  $m_r$ , dragging the swell direction to the left. (b) The first data point has been removed and reduces  $m_r$  considerably and improves the resulting swell direction.

### 5.5 Discussion

The method of swell parameter extraction discussed here is a good hydrodynamic representation of the interactions between the Bragg waves and the swell. However as discussed during the adaptation of Barrick's solutions to swell parameter extraction, there is an electromagnetic component that is coupled with the hydrodynamic interaction to provide a complete description of the situation occurring on the ocean surface. Barrick (1972b), introduces this as a coupling coefficient,  $\Gamma_{T} = \Gamma_{EM} + \Gamma_{H}$ , that includes both the electromagnetic and hydrodynamic components. This method proved too sensitive to provide reliable results from averaged COSRAD spectra and demanded relatively complex computational requirements. The simplicity of the frequency modulation algorithm not only provides a computationally fast method but also a robust one. Therefore, the question arises, by neglecting the electromagnetic interaction, how are we affecting the quality of the resulting parameters? The hydrodynamic effect is the dominant of the two interactions which is why reasonably accurate swell parameters can obtained without accounting for the electromagnetic component. electromagnetic component does, however, affect the spectrum to some degree. The asymmetry commonly seen in the sidebands, where one sideband of a pair is noticeably less powerful than the other, is due to the electromagnetic interaction. The approach used here relies on frequency modulation theory which specifies that the sidebands are equal in strength about the first-order line. The spectrum according to frequency modulation theory consists of a carrier and an infinite number of sidebands, all of whose amplitudes are various-order Bessel functions of the modulation factor, m, as defined in equation 31 and 32.

Calculating  $R_{swell}$  using the average swell peak height was implemented to reduce the effects of peak bifurcations on the resulting ratios and to reduce the electromagnetic induced asymmetry in the sidebands. By taking the mean swell peak power, any contribution to the asymmetry by this already weak electromagnetic interaction is reduced further so that the model presented above is almost solely based upon the hydrodynamic interaction between the swell and the Bragg waves which is adequately described by frequency modulation theory.

A model for second-order Doppler spectra, with the ability to include or exclude the electromagnetic component, was used to calculate the theoretical frequency spectrum. The aim of this model was to demonstrate the contribution of this electromagnetic interaction on the Doppler spectrum. A comparison of Doppler spectra calculated with both the hydrodynamic and electromagnetic components involved could then be directly compared to a hydrodynamic only case generated under the same conditions. Figure 30 shows one side of a Doppler spectrum generated in this manner. Firstly, a wind wave spectrum is defined using a Pierson and Moskowitz (1964) model and then a simple swell is added to this spectrum. The wind wave parameters entered here include the wind direction, wind speed and wind spread. The swell component is defined by the period, direction, spread and desired peak width of the swell. Although some asymmetry remains in the hydrodynamic case it is reduced with respect to the electromagnetic case. In this specific case the lower peak increased markedly and the stronger peak reduced only very slightly. Therefore by taking the mean swell peak height in both cases will result in a very similar value.

To show this more thoroughly, Figure 31 shows both cases calculated over a range of swell directions with respect to the radar beam. The figures show the decreasing swell peak amplitudes as they approach 90 degrees with the asymmetry present for both cases. The average amplitude is also taken every 10 degrees. The asymmetry is greater in the case where the electromagnetic coupling is applied although still present to a lesser degree in the hydrodynamic only case. Importantly, this example shows that averaging the asymmetry in both instances results in very similar amplitudes, supporting that the hydrodynamic effect is the dominant interaction inducing the peaks in the second-order spectrum.

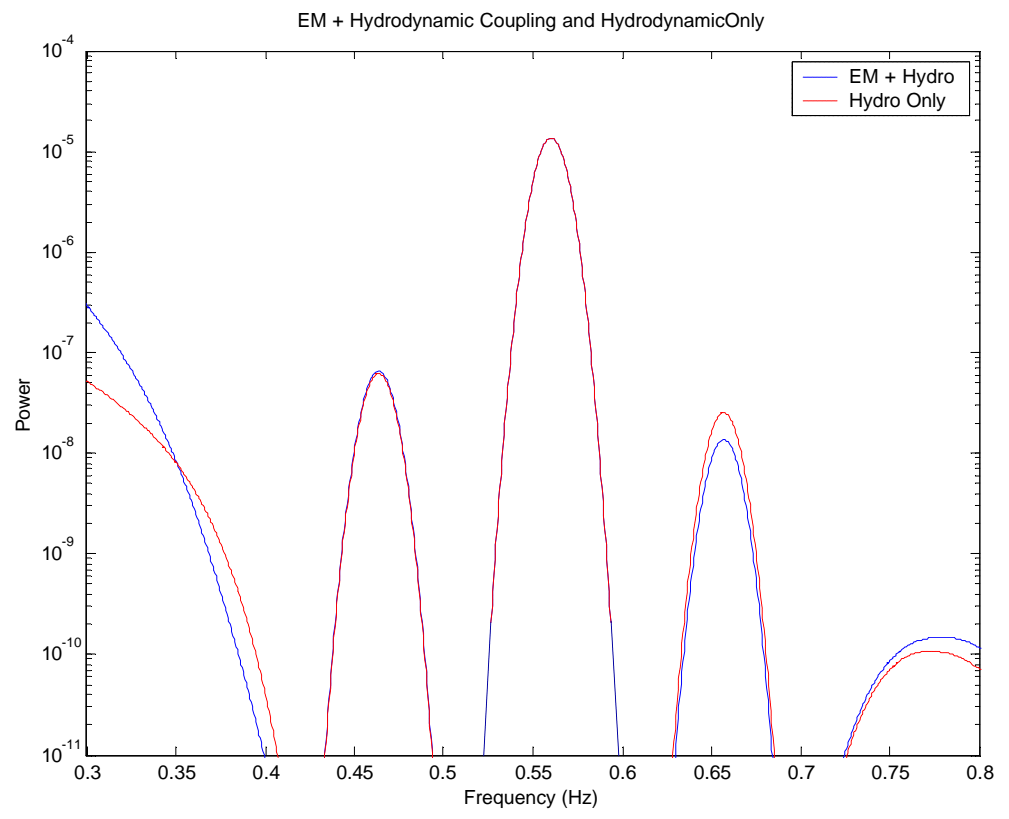


Figure 30: Highlights the contribution of the electromagnetic component on the sideband asymmetry. The red dash line shows the spectrum calculated using the hydrodynamic coupling only and there is a significant shift in the sideband powers in an attempt to become level. Wind wave parameters: wind speed = 5m/s, spread = 40deg, direction = 100deg. Swell parameters: Period=12s, direction=70deg, spread=10deg and peak width=0.02s.

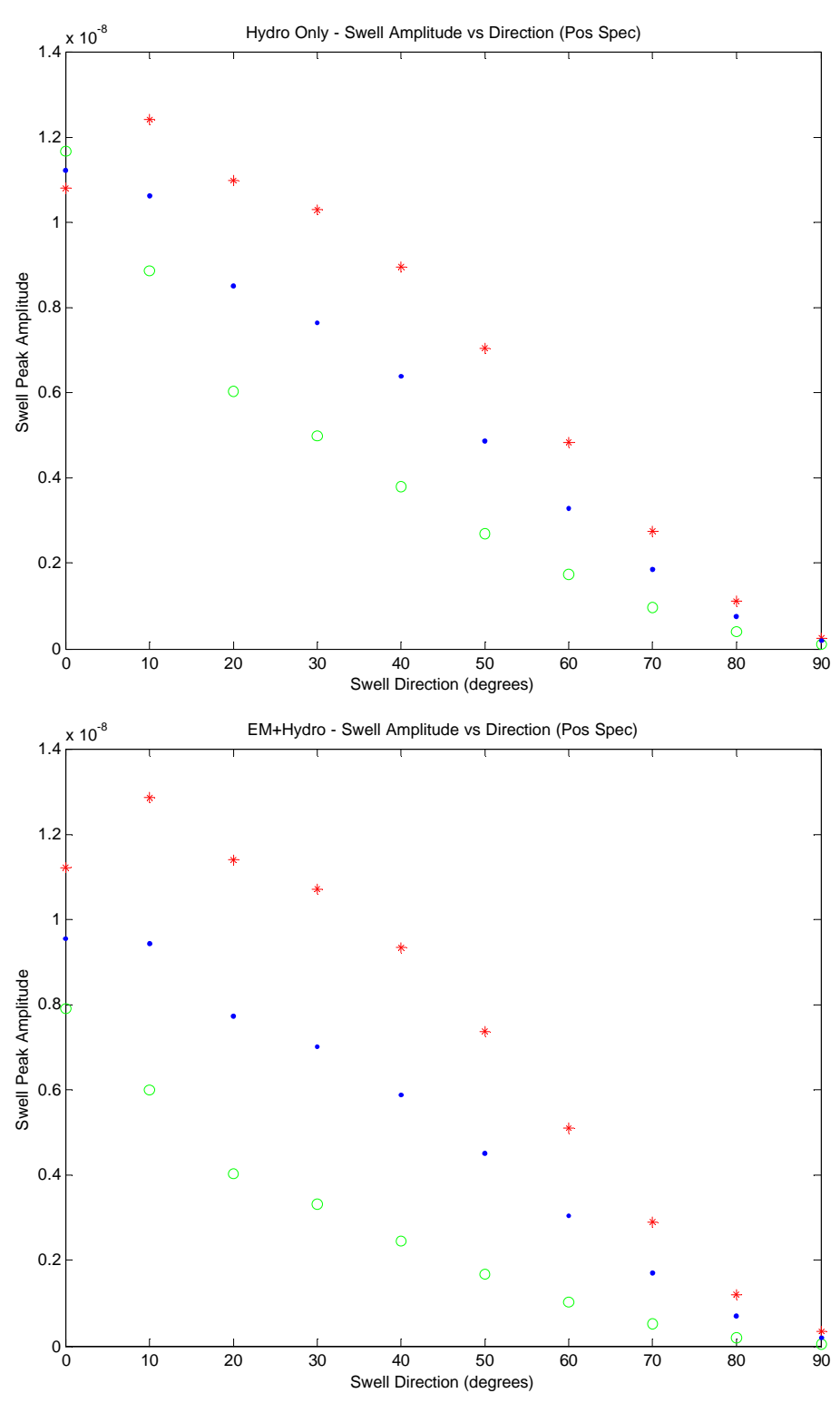


Figure 31: o – Inner swell peak,\* - Outer swell peak, • - Mean swell peak power. Peak amplitudes resulting from an increasing angle between the swell propagation direction and radar look direction.

## Chapter 6: Testing and Results of the Automated Swell Algorithm

The following chapter presents the results of the working algorithm for the extraction of swell wave parameters and their comparison with in situ wave buoy data. A brief summary of the oceanographic conditions experienced throughout each deployment, both Tweed Heads and Bass Strait, is presented as observed in the wave buoy records. Periods of strong swell conditions are identified and used to indicate the best time during the deployment to test the completed algorithm. Once tested on a small subset of data, any final additions or changes to the methodology will be made if necessary to improve the performance of the extraction. Following this the entire deployment will be analysed to produce a long record of swell parameters that is comparable to the corresponding wave buoy.

Also discussed and evaluated in this chapter are the limitations to the algorithm. These limitations are expected to be dominated by the quality of the radar spectra for analysis of the second-order structure. Increased noise in the spectrum can be due to the size of the waves and the range at which they are being measured. Since the strength of the swell is a factor in determining the signal to noise ratio, this suggests that at some point, as the swell decreases in height, the noise will increase making the analysis of the second-order increasingly difficult. Thus the algorithm will have a lower limit for detectable swell height. Swell waves that are smaller than this height limit will not be reliably detectable in the spectrum and thus the extracted parameters will display this noise. This value ( $Hs_{min}$ ) will be determined for both the Tweed Heads and Bass Strait deployments. This value may be unique to each deployment as the dwell time for the radar at Bass Strait was double the value employed at Tweed Heads. The upper limit on detectable swell height is determined theoretically as the saturation limit. This limit is defined by Hisaki (1999) and, Lipa and Nyden (in press) as

$$h_{sat} = \frac{2}{k_0} \tag{34}$$

This equates to a saturation limit of 3.18 m at a radar frequency of 30 MHz. This value could not be validated using data from either deployment as the greatest swell height observed was only 0.96 m.

The other limitation that needs evaluation is the maximum effective range of the algorithm. Both at Tweed Heads and Bass Strait deployments the radar collected data for 12 pixels in each sector at 3 km intervals. It is expected that averaged spectra evaluated using the distant pixels towards the end of each sector may be affected by noise to the extent that the algorithm becomes unreliable. The furthest range at which the algorithm still extracts swell wave parameters that are comparable to the wave buoy and of similar accuracy to near shore ranges will be determined as the maximum working range of the algorithm.

### 6.1 Wave Buoy Analysis at Tweed Heads

The QBPA owned Datawell Directional Waverider Buoy, positioned inside the COSRAD coverage zone at Tweed Heads, continually monitors wave parameters and records a power spectrum (m<sup>2</sup>/Hz) every 30 minutes. Swell wave information can be extracted from this spectrum using a frequency window method to find the swell peak. This method is similar to the one used to extract the second-order structure in a COSRAD spectrum. The frequency limits used to locate the swell peak in the wave buoy spectrum are 18-8 seconds, which converts to frequencies of 0.055 and 0.125 Hz respectively. This frequency window can be seen to enclose a prominent swell peak in Figure 32 below. The energy contained at higher frequencies in the spectrum, such as the minor peaks at ~0.2 Hz equate to wind waves with periods of approximately 5 seconds. The swell wave height can be determined by finding the square-root of the area enclosed by the swell peak for a unit frequency increment. The swell period is simply determined by inverting the frequency of the peak and the direction is measured by the wave buoy at each frequency. These parameters were extracted from the wave buoy data for the duration of the COSRAD deployment and are shown in Figures 33, 34 and 35 below.

The position of the wave buoy is relatively close to shore in comparison to the maximum working range achievable by the COSRAD system (Figure 4 – COSRAD coverage map Chapter 2). Some differences in the comparison of the two measurements can be explained by a combination of the fact that the two instruments are not

measuring exactly the same waves and also the COSRAD measurements result from an averaged range of pixels compared to the single point measurement of the wave buoy. However, as long as the water depth is still considered to be deep water in terms of the waves being measured at both locations the two data sets are comparable.

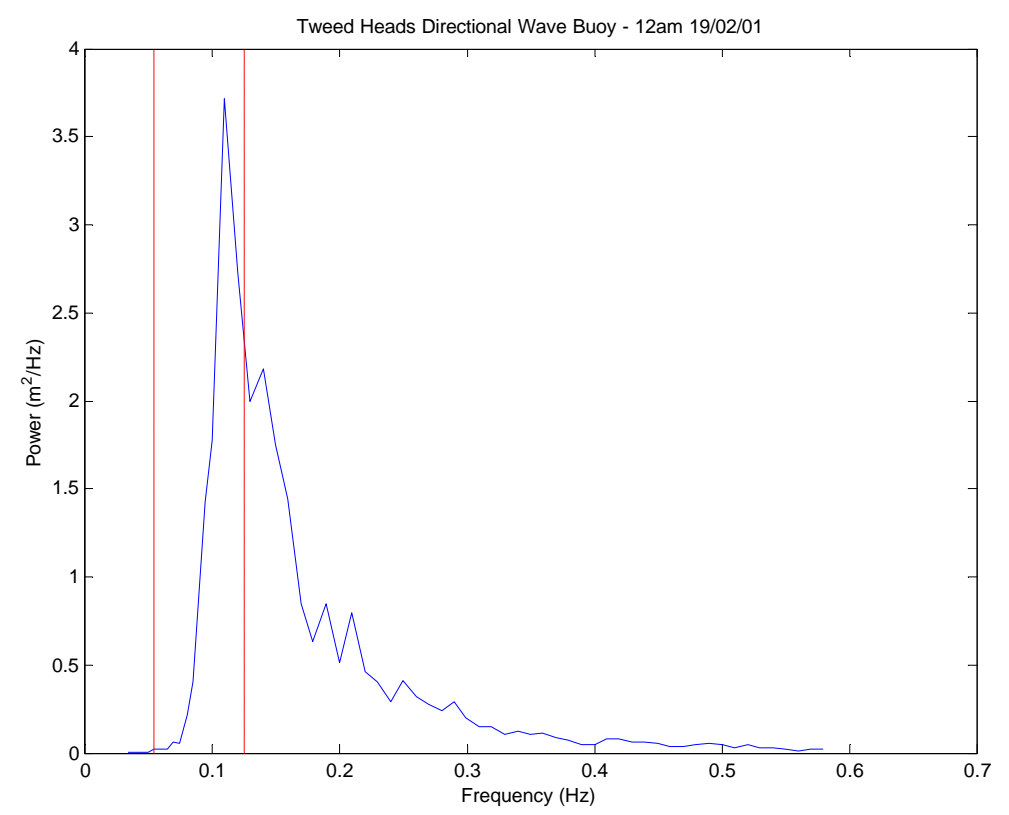


Figure 32: Power spectrum from the Tweed heads wave buoy showing a swell peak at 0.11Hz (period of 9.1s). The dashed lines represent the swell frequency window at 0.055 and 0.125Hz

The swell height record as seen in Figure 33 shows good variation in wave height over the course of the deployment. There are periods of low energy swell and also stronger periods that will provide a reasonable range to test the sensitivity of the algorithm. However, the strongest swell observed during the deployment, less than 1m, is still categorised as 'low' as shown in Table 2. Weak swell conditions such as these may not be within the algorithm's capabilities for measurement, particularly at long ranges.

Height (metres)	Description	Length (metres)	Description
0-2	Low	0-100	Short
2-4	Moderate	100-200	Moderate
Over 4	Heavy	Over 200	Long

Table 2: Swell wave classification table taken from Bureau of Meteorology – Observing the Weather: The Australian Co-operative Observers Guide, 1991.

The record can be divided in to three major phases as shown in Figure 33. The first major phase is a period of swell height of approximately 0.3 m with a brief increase to 0.4 m, labelled as Phase 1(a). These periods may prove valuable in determining the  $Hs_{\min}$  value. This phase is easily distinguishable from the following phase which is characterised by very low energy swell. The boundary between the two is a sharp decrease of almost 0.2 m. The third phase is in the latter part of the Tweed Heads deployment is characterised by the strongest swell conditions. Data from this phase was chosen as a test set for the algorithm due to this strong swell activity which peaks on the 6<sup>th</sup> of March. After this peak in swell height a gradual decay in conditions from the 7<sup>th</sup> to the 11<sup>th</sup> of March is observed. As recorded by the wave buoy, the swell hight decreases from 0.96 m to 0.2 m during this time. The maximum swell height is well inside the saturation limit ( $h_{sat}$ ) for the transmitting frequency of the COSRAD system.

These three phases in swell height have been superimposed on the swell period record in Figure 34. Phase 1 does not generally show any marked change in swell period with the increase in height. However, the brief surge to shown in Phase 1(a) is evident as a sharp spike in wave period increasing from 9 to 12.5 seconds. Phase 2 exhibits an increase in period during this low energy swell. Phase 3 reaches a maximum period of 14 seconds and averages approximately 12 seconds between the 4<sup>th</sup> and the 8<sup>th</sup> of March. The period then decreases to 10 seconds at a similar rate to that of the decreasing swell height over the next few days.

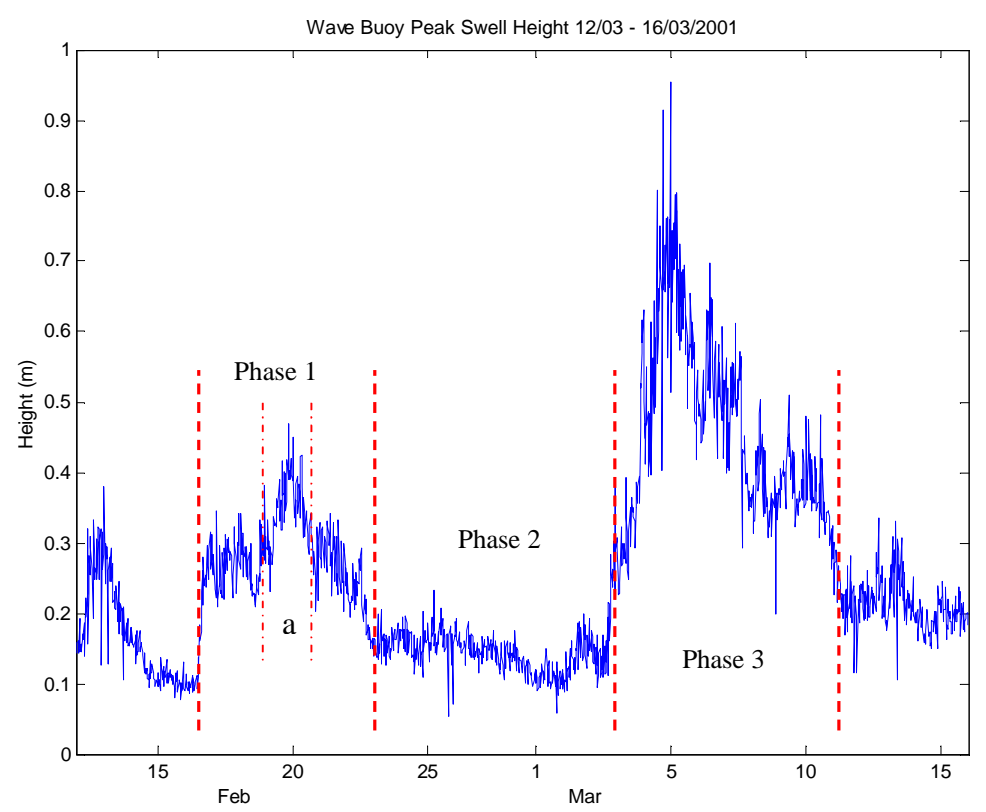


Figure 33: Swell height record extracted from power spectra measured by the QBPA Directional Waverider buoy at Tweed Heads.

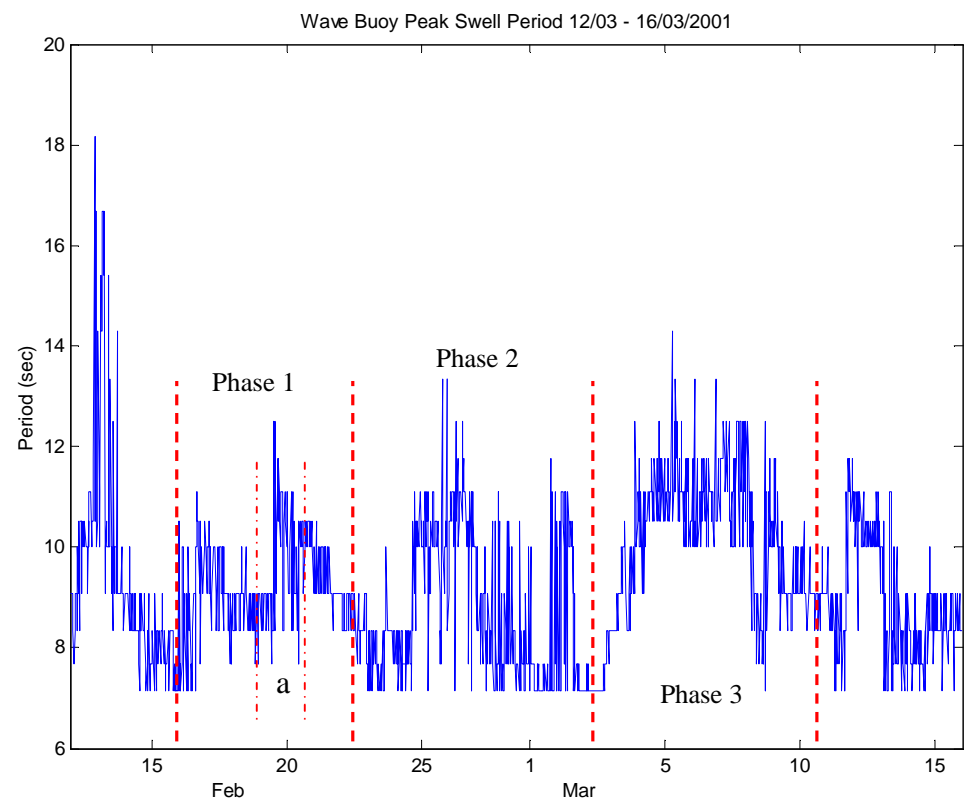


Figure 34: Swell wave period as measured by the QBPA Directional Waverider buoy at Tweed Heads. An extract from 12/02 to 16/03/2001.

This approach was also employed to highlight changes in swell direction (Figure 35) that correspond to these distinct phases in swell height. Phase 1 is easily distinguishable in the directional record. The swell direction changes from approximately 90 degrees East (magnetic) on either side of Phase 1, to an average of 110 degrees East (magnetic) during Phase 1. The sharp increase in wave height that characterises Phase 1(a) is seen as a sharp change in direction from 110 to 90 degrees East (magnetic) and then gradually returns to 110 degrees. As the wave height decreases sharply at the boundary of Phase 1 and Phase 2 the swell returns to an easterly direction. No further changes in the direction can be linked to changes in swell height during Phase 2 even though the swell direction does vary by up to 20 degrees. Phase 3 begins at 120 degrees East (magnetic) and gradually changes towards an easterly direction as the phase progresses. This does not appear to be linked to the changing swell height as, during this slow rotation towards the east, the swell height increases to reach its peak of 0.96 m and then decreases with no affect on the direction.

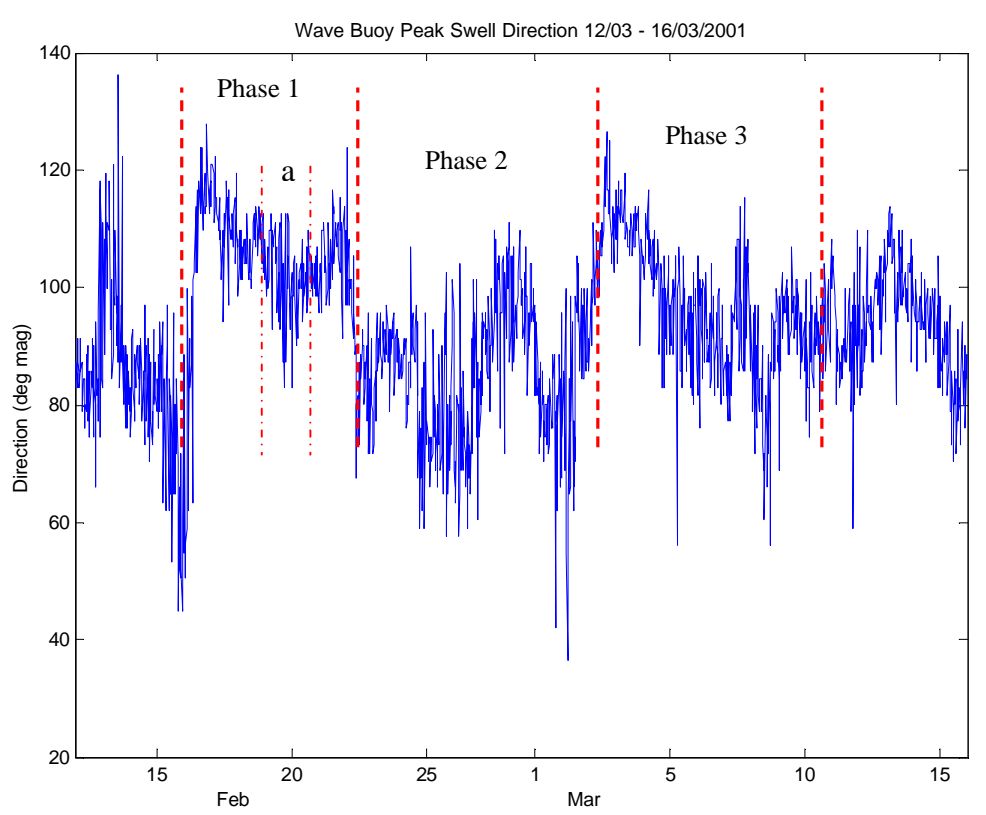


Figure 35: The swell directional record as measured by the QBPA Directional Waverider buoy at Tweed Heads.

# 6.2 Automated Algorithm Results for Swell Height, Direction and Period at Tweed Heads

It was decided that data from the Tweed Heads deployment would be used to test the performance of the algorithm. This is mainly because this data set was used when developing the spectral processing procedures at the beginning of the project and also due to the slightly stronger swell conditions experienced over the course of the deployment. A day long extract of radar data from the 6<sup>th</sup> of March was analysed using the automated swell algorithm. It was during this day of the deployment that the strongest swell conditions were recorded by the wave buoy, and for this reason it was seen as a good set of data for testing the algorithm. The manifestation of the swell waves in the radar Doppler spectrum during this period would be at their peak and reduce the impact of noise on the second-order. A relatively near-shore range for the radar was selected, the average of pixels 3 to 6, which is easily within the range limit but also beyond any shallow water effects. Data from the Tallebudgera station was tested first.

### **6.2.1** Tallebudgera Station

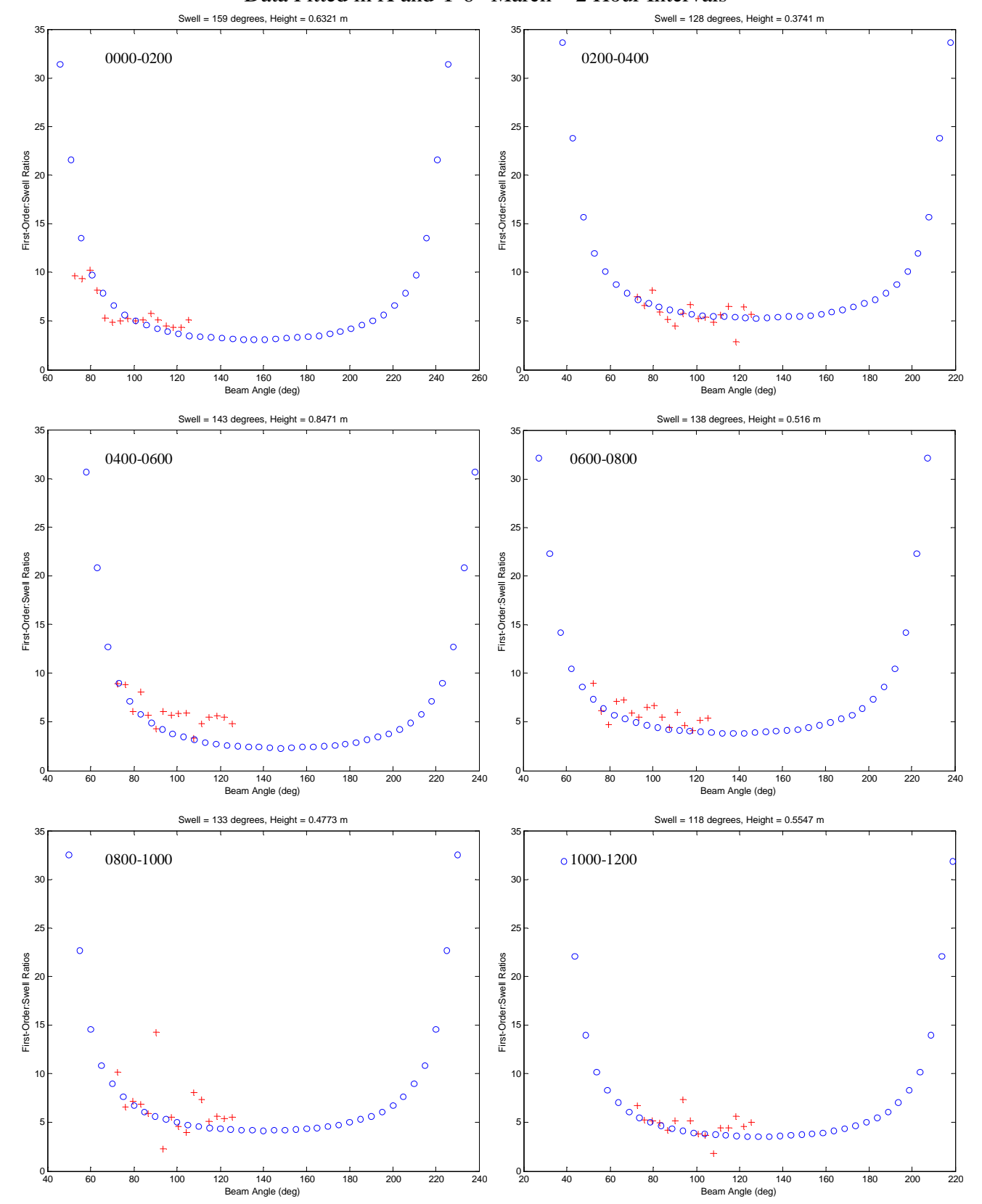
The Tallebudgera data tested well when compared to the wave buoy. Figure 36 shows the fit of the ratios extracted from COSRAD data to the theoretically derived ratios for each 2 hour period. The ratios, calculated at 16 points across the sweep, show a slightly negative gradient as would be expected. As the beam sweeps from left (69 degrees East) to right (129 degrees East) the angle between the beam and the direction of swell is reduced. Therefore the second-order peaks increase in strength as the beam sweeps across which results in a decreasing swell to Bragg ratio ( $R_{swell}$ ). The swell direction as measured by the algorithm agrees well, to within approximately 15 degrees, with the wave buoy. The first value, 12am to 2am, produces a swell direction of 159 degrees which is obviously in error. When the  $R_{swell}$  values in the first diagram of Figure 36 are examined it can be seen that the trend can be separated into two groups. The first is a cluster of four ratios that are detached at a higher value, approximately 4 points higher,

and a second group consisting of the remaining ratios. If this first group of values were removed the remaining second group would provide a gradient which is nearly zero. The resulting directional shift of such a gradient would be very close to 100 degrees and close to the measured direction of swell by the wave buoy. This example highlights the effect that a minority of slightly noisy  $R_{swell}$  values can have on the resulting swell direction. It is possible that the first four sectors of the sweep encountered some interference or noise source affecting the second-order structure. The method of removing points that are outside two standard deviations from the line of best fit does not always prevent the occurrence of incorrect  $R_{swell}$  values particularly when there are multiple noisy values in the sweep. This large discrepancy is inherent to the geometry involved in the fitting process. When the radar beam is pointing close to the direction of swell propagation we expect to find the  $R_{swell}$  data to plot about the minimum of the synthetic curve. However, inaccuracies in the ratio values, resulting in a slightly more negative or positive gradient, produce an exaggerated shift in the directional domain when matching this gradient. This is the consequence of fitting low gradients to such a shallow curve. Small variations in the gradient equates to a large discrepancy in the direction. Conversely, fitting low gradients to a shallow curve produces a high degree of accuracy in the vertical domain. If the trend of  $R_{swell}$  swell values is almost horizontal, as in the latter half of the test period, the swell height is measured accurately and compares extremely well to wave buoy measurements. The algorithm results for swell height are within 0.1 m of the wave buoy during this part of the test (Figure 37(b)).

Figure 37(a) shows the comparison of the radar-extracted swell direction with the wave buoy measured values at two hour intervals for March 6. Apart from the initial noisy result discussed above the remaining values compare to within 15 degrees of the wave buoy value. This is also the case with the extracted wave heights shown in Figure 37(b). The first value is again in error but the remaining heights compare to within approximately 0.1 m. The radar extracted heights are calibrated to the wave buoy data to give the best overall fit for that day.

The swell period is calculated independently of the frequency modulation method however it is an important parameter to extract to completely describe the sea state. The swell period for March 6 varies between 10 to 12 seconds according to the wave buoy. From the COSRAD data the average swell period for this test was approximately 12 seconds. These results for swell period are validated by the wave buoy in Figure 37(c).

# Data Fitted in X and Y 6<sup>th</sup> March – 2 Hour Intervals



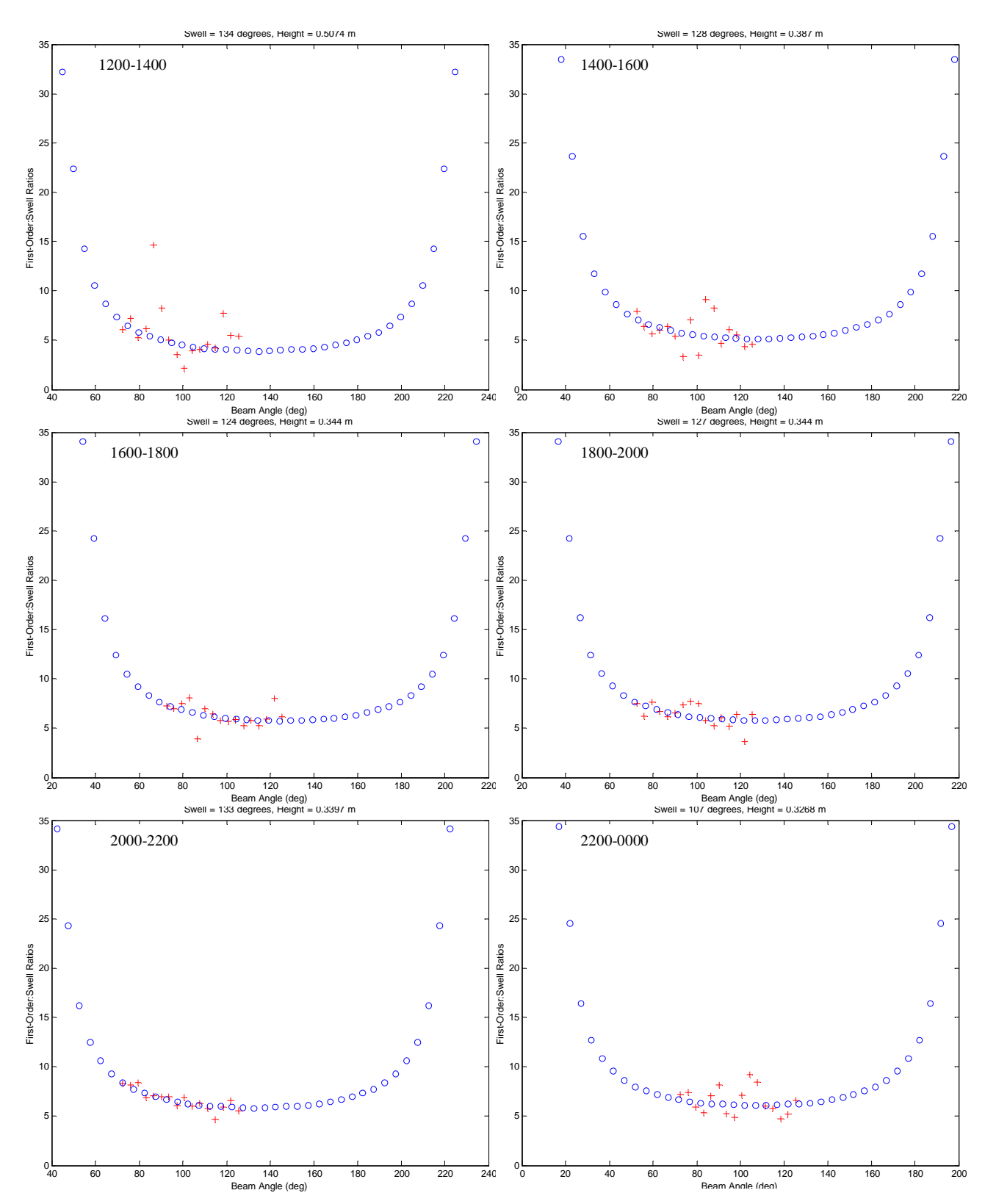
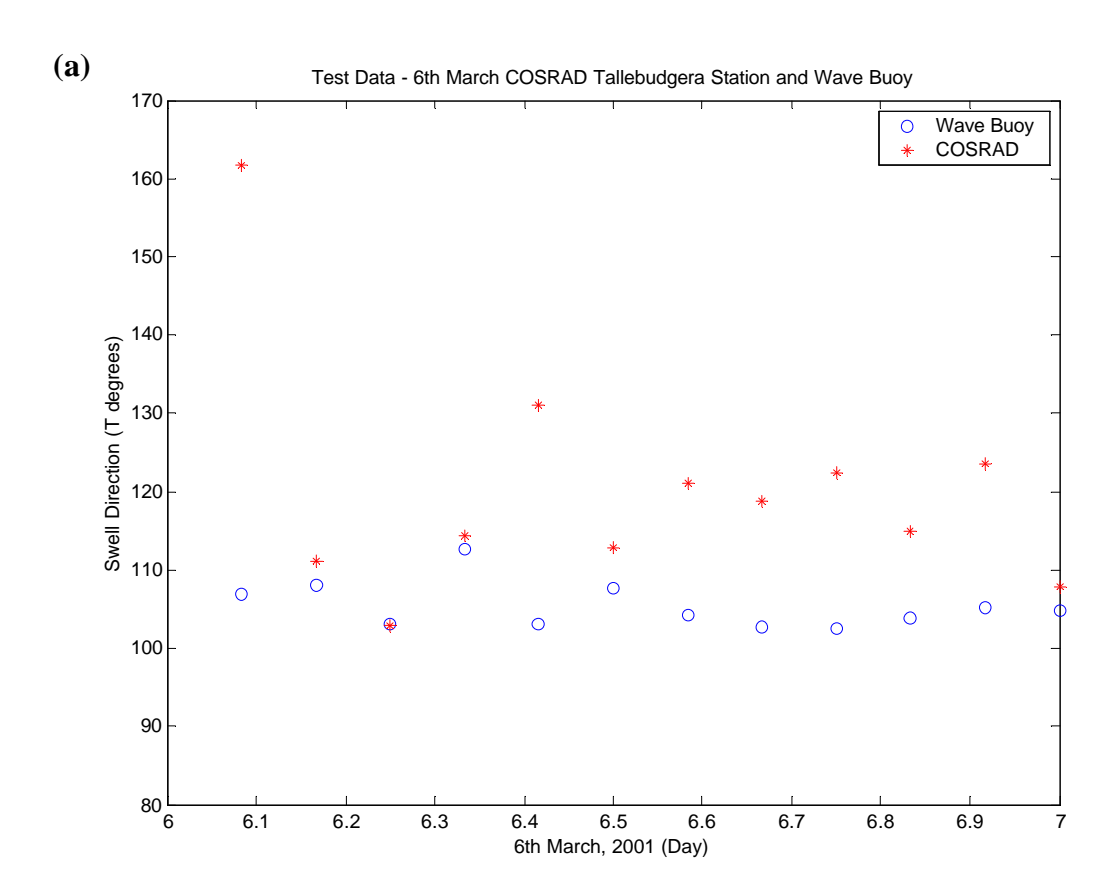


Figure 36: Radar data from the Tallebudgera station fitted in both direction and height to model results at 2 hour intervals for the  $6^{th}$  March.



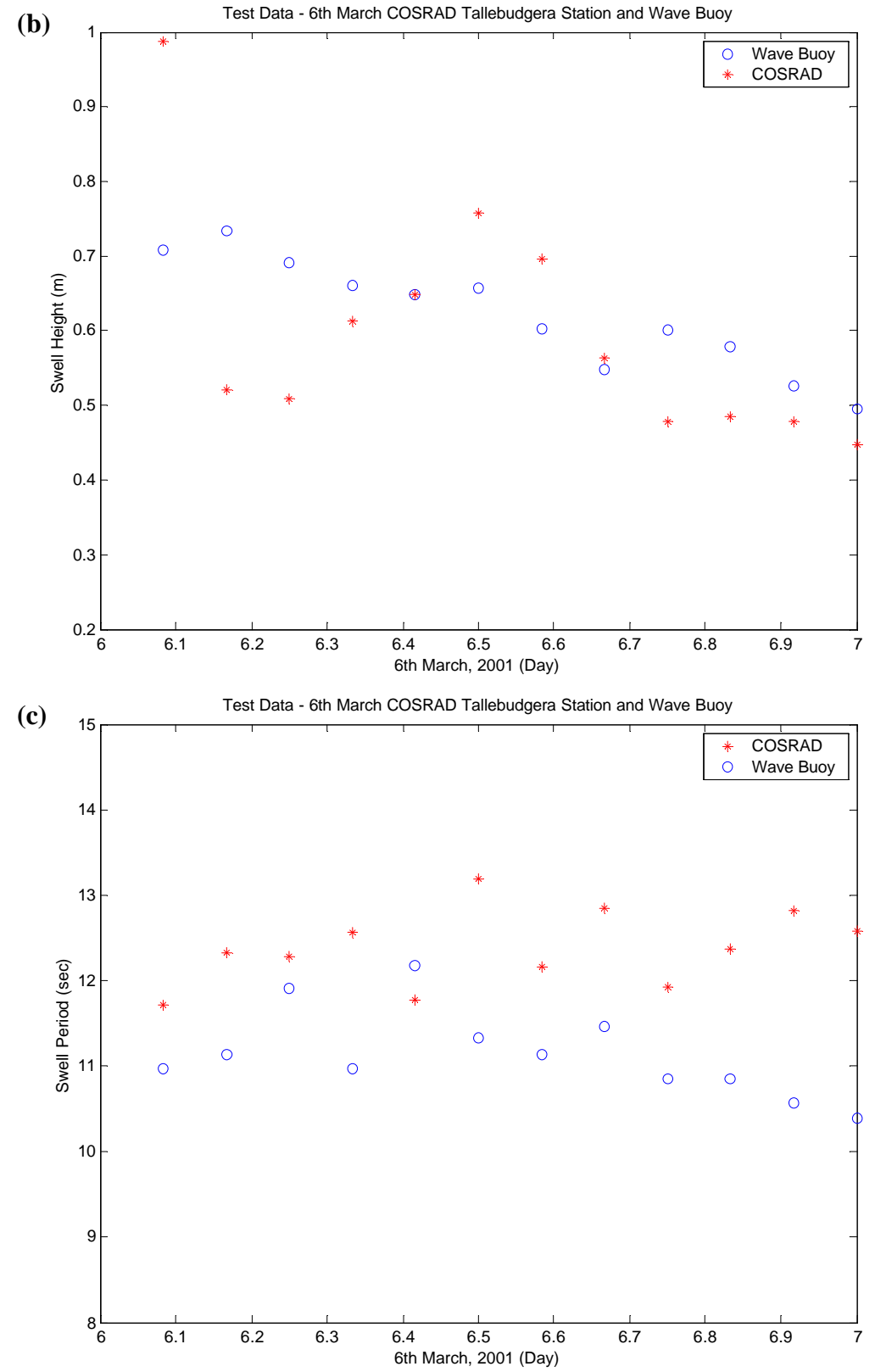


Figure 37: March 6 data used for testing the algorithm is compared to the QBPA wave buoy at Tweed Heads. (a) Swell direction, (b) calibrated swell height and (c) swell period.

Following this successful test, the remaining data from the Tallebudgera station was analysed using the algorithm. Figure 38 shows the comparison of the directional wave buoy at Tweed Heads with the swell parameters extracted by the algorithm. The swell height comparison clearly shows reduced noise levels in the results over the period where the swell height is at its greatest. The noise also decreases for a period around February 20 where the swell height is slightly elevated from the minimum but still significantly lower than the maximum swell height encountered on March 6. It is this phase and the period about March 9 and 10 that will determine the working capabilities of the algorithm in low swell conditions ( $Hs_{\min}$ ). The minimum swell height for the algorithm to produce reliable heights appears to be approximately 0.3 m. Below this value the swell heights extracted from the radar data become unreliable.

Although the same effect can be seen in the directional comparison it appears that the value of  $Hs_{\min}$  is higher than that of the height comparison. This difference in  $Hs_{\min}$  values for swell height and direction is not unexpected and is due to the angle between the station's bore sight and the dominant direction of swell wave propagation. As discussed above the bore sight at Tallebudgera is almost directly in line with the direction of propagation at the time of the strong swell phase. This provides the algorithm with the most favourable conditions for the swell height extraction process. However, these conditions are not quite optimal for the extraction of swell direction. With these conditions the signal must be strong for the accurate extraction of swell direction and this can be seen in the results with good comparison between the buoy and algorithm at the time of highest swell. As the swell height decreases the extracted direction quickly becomes overwhelmed with noise long before the extracted swell height begins to suffer. This places the  $Hs_{\min}$  value for swell direction at approximately 0.5 m.

Swell period is found independently of the frequency modulation method of parameter extraction and is extremely accurate even in times of weak swell conditions. During the strong phase, the algorithm measures the period to within less than 1 second of the wave buoy. This increases to 2 seconds when the swell is less than 0.2 m in height. This is definitely an acceptable range of error under such weak conditions.

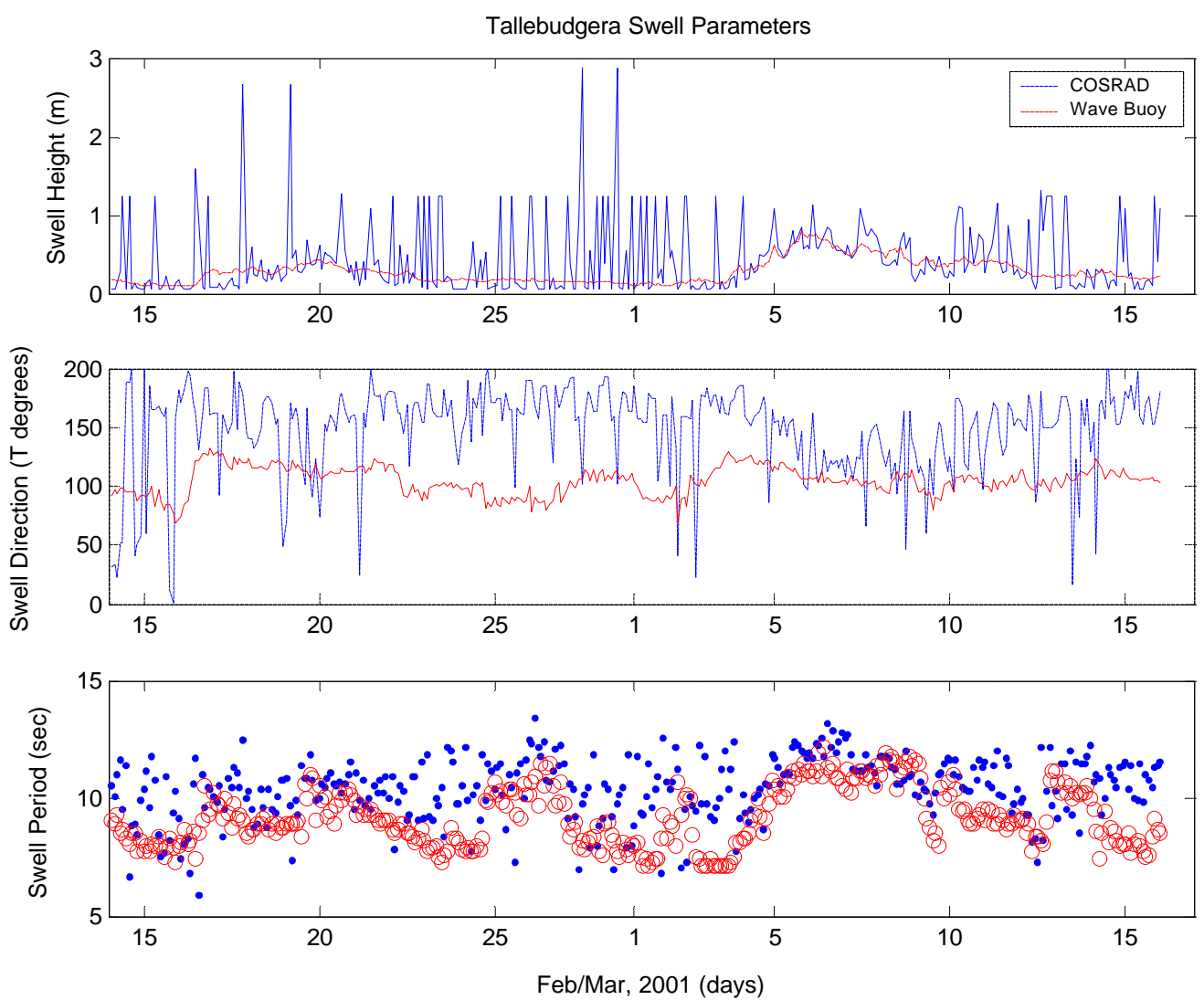


Figure 38: Deployment record of swell parameters extracted from radar data collected at Tallebudgera compared to the QBPA Waverider buoy. In the swell period record, o denotes wave buoy measurements.

### **6.2.2** Kingscliff Station

The Kingscliff station provided poor results in comparison with those extracted from data collected at Tallebudgera. This is a consequence of the effective geometry between the approaching swell and the bore sight of the Kingscliff station (21 degrees East). The COSRAD stations at Tweed Heads were positioned so that their sweep patterns intersected orthogonally in order to resolve surface current vectors. This geometry is not necessarily optimal for resolving swell wave directions using this methodology. In this instance the station at Kingscliff is directed so that for much of the deployment the radar is looking along the crests of the swell waves. This results in little or no manifestation of swell waves in the Doppler spectrum. During the strong swell periods of the deployment the wave buoy measured the direction of swell propagation to be approximately 100 to 120 degrees East. Therefore the wave crests are lined up along directions between 10 to 30 degrees East, perpendicular to the direction of wave propagation. With a bore sight of 21 degrees and therefore extreme beams at 351 and 51 degrees East, ±30 degrees, much of the sweep is looking perpendicular to the direction of propagation. The beams surrounding the bore sight would record no indication of swell in the spectrum. The extreme beams may obliquely detect the swell but at these angles the second-order peaks would not be prominent and difficult to routinely identify amongst the clutter of the second-order. This makes it difficult to supply the model with a reliable trend of swell peak to Bragg peak ratios.

The advantage of this method of swell detection is that it is not necessary for both stations to provide results in order to resolve the parameters. If only one of the two stations is in position to capture the swell at angles near to that of the wave propagation reliable results will be produced. With the stations positioned to optimize the extraction of surface current parameters it is expected that one station will be in a better position to take swell measurements than the other at any given time. The particular station providing the better results may change over the course of the deployment as the direction of swell propagation varies.

# 6.3 Automated Algorithm Results for Swell Height, Direction and Period at Bass Strait

Bass Strait is renowned for its extreme sea states (Spillane et al. 1972, Falconer and Linforth, 1972 and Gush, 2003) and it was the focus of this deployment to observe strong swell conditions. A second validation of the extraction algorithm with stronger swell conditions than those observed at Tweed Heads would support this method of swell monitoring. However, weak swell conditions dominated the region for the majority of the deployment. The average swell height over the course of the deployment was less than 0.3 m and reached a peak on July 17 of 0.48 m (Figure 39). This stronger swell, greater than 0.4 m, lasted for two days before rapidly decreasing over the following days. This strong phase is observed in the swell period record as a distinctly shorter period, ~12 seconds, than the weaker swell that precedes it, ~15 seconds (Figure 40). It was found in the analysis of the Tweed Heads data that swell heights below 0.4 m provided increasingly noisy results particularly in the directional domain. Therefore the conditions observed during the Bass Strait deployment should confirm the values of  $Hs_{min}$  for the accurate extraction of swell height and direction. If  $Hs_{min}$  is similar to that at Tweed Heads then the majority of the Bass Strait data will potentially not provide accurate swell information. However, it will also be interesting to see if the increased dwell time of the radar beam at Bass Strait will act to effectively lower the  $Hs_{min}$  value and allow for the analysis of the weak swell conditions in this data set. This will provide valuable information for determining the optimal configuration of the COSRAD system for coastal monitoring of swell waves in the future.

The wave buoy directional swell record remains relatively consistent throughout the deployment, varying by only 20 degrees (Figure 41). During the peak phase the swell direction is 200 degrees East (magnetic) which is slightly higher than the average swell direction of approximately 195 degrees East (magnetic). The bore sight for the Portsea station is 252 degrees East, therefore at its extreme, negative, beam (222 degrees East) the radar beam will never quite point directly into the propagating swell. The magnetic declination for the east coast of Australia is approximately 11 degrees which brings the swell to within 10 degrees of this extreme beam at Portsea. The Ocean Grove station is

facing towards 147 degrees East which makes its most extreme, positive, beam pointing at 177 degrees East. Therefore this beam is at a minimum 20 degree angle to the direction of swell propagation. This suggests that the Portsea station was in a slightly better position for observing the swell during this deployment which will likely be displayed in the quality of the extracted parameters. The positioning of these stations is an improvement over the situation encountered at Kingscliff. The other extreme beam of the Portsea radar is directed at 282 degrees which is just short of encountering the swell orthogonally. However the Ocean Grove radar may encounter this situation with its most negative beams (117 degrees) at some stages of the deployment. Given this, the Portsea station in particular may be in a perfect position in terms of bringing a balance to the fitting routine when trying to accurately measure both direction and height simultaneously.

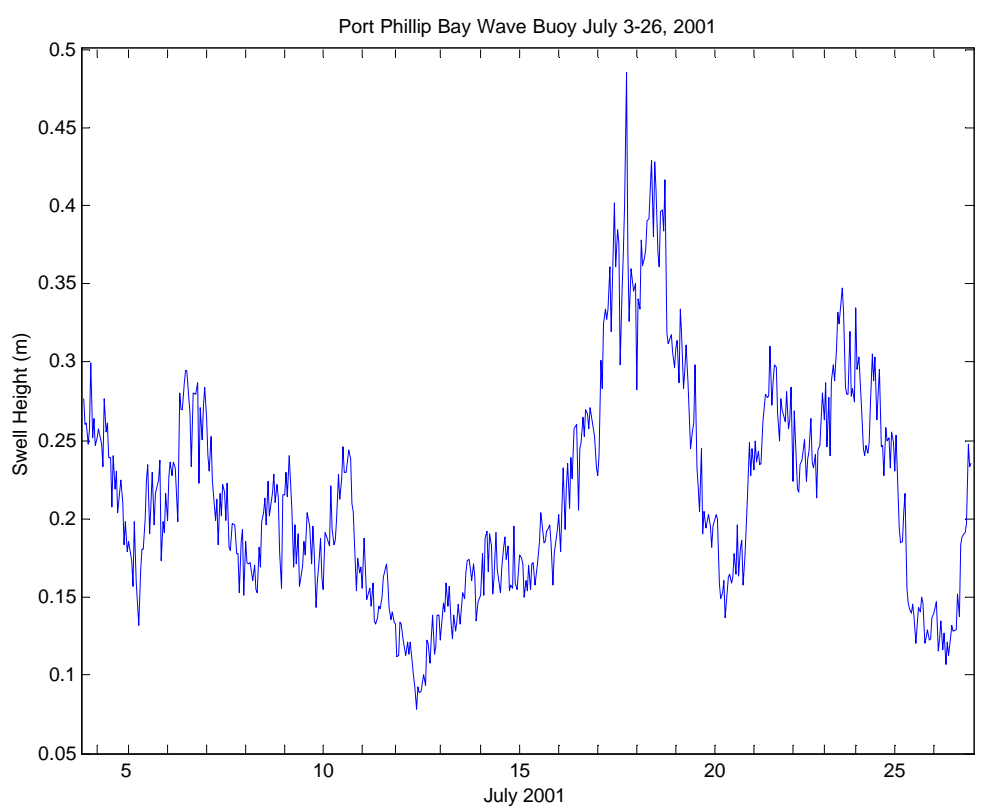


Figure 39: Swell height as measured by the Victoria Channels Authority's (VCA) Waverider buoy for July 2001.

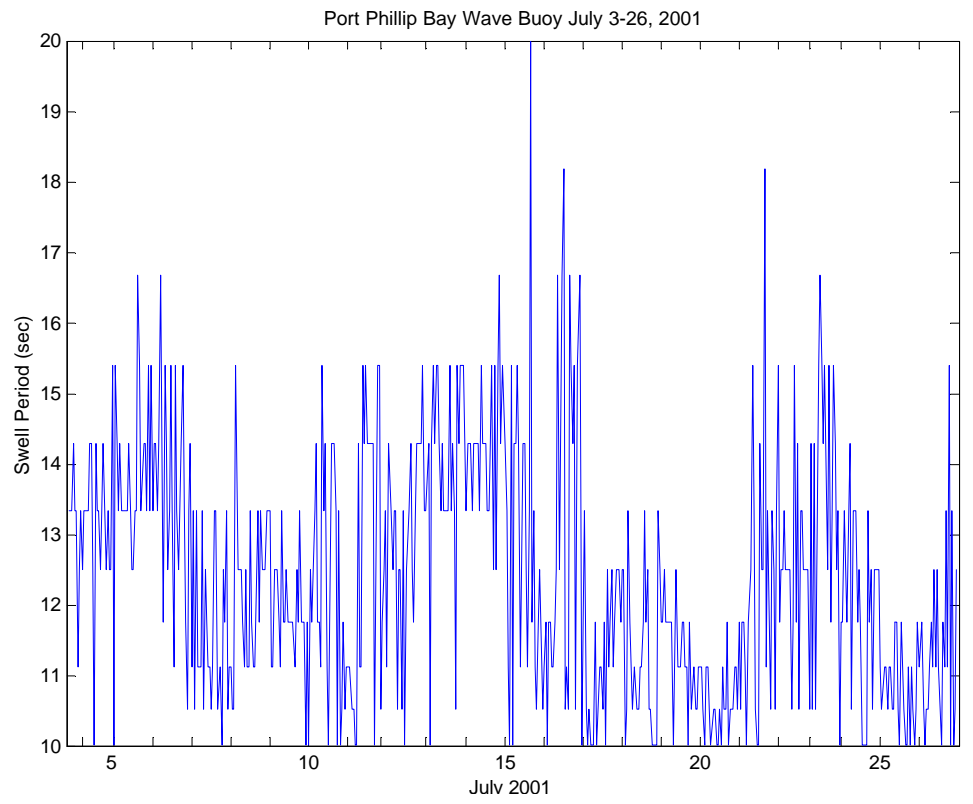


Figure 40: Swell period as measured by the Victoria Channels Authority's (VCA) Waverider buoy for July 2001.

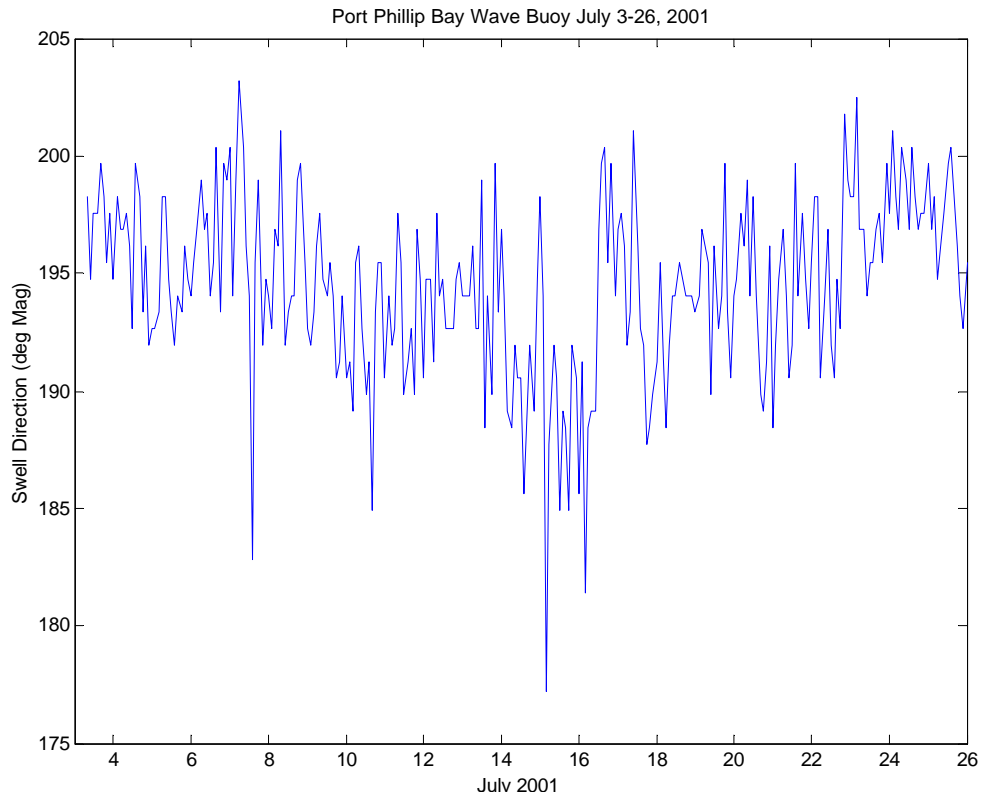


Figure 41: Swell direction as measured by the Victoria Channels Authority's (VCA) Waverider buoy for July 2001.

### 6.3.1 Test Case: Portsea Station – July 18, 2001

The first analysis of Bass Strait data was completed at the pixel range 3 to 6 from both Portsea and Ocean Grove stations. In this range band the radar is illuminating the ocean surface well beyond the surf zone where the water is deep and the signal is strong. With the swell conditions considerable weaker than those at Tweed Heads an initial test of the algorithm on data collected on July 18, when the swell was at its peak for the deployment, was conducted. This test was carried out to ensure that reliable data could be extracted from the second order in such conditions. During similar periods of swell height at Tweed Heads the algorithm was operating close to its limit for accurate swell measurement. The  $Hs_{\min}$  value for swell height detection at Tweed Heads was 0.4 m, and it was 0.5 m for accurate swell direction measurement. However, these values suffered, particularly swell direction measurement, from poor radar-swell geometry. This appears to have improved for this deployment, particularly in the case of the Portsea station.

Swell height during July 18 ranged from approximately 0.32 m to 0.42 m. This will provide a good test of the capabilities of the algorithm and may give an indication of the importance of improved radar-swell geometry or maybe improved results due to the increased radar dwell time in place for this deployment. Figure 42(a) shows excellent agreement between the COSRAD measured swell heights and the directional wave buoy. Even at swell heights of only 0.3 m the radar measurements are within 0.1 m of the wave buoy. Similar success was achieved with the measurement of swell direction (Figure 42b). A spread of approximately ±10 degrees about the wave buoy measurement was found. The algorithm detects the small undulation in swell direction during the first half of the day. This short test period shows promise for the successful measurement of swell parameters over the remaining time period. Although the swell conditions on this day are more favourable than much of the remaining deployment, and there are likely to be periods where the swell is simply too small for measurement, the results displayed here are already an improvement over those achieved at Tweed Heads.

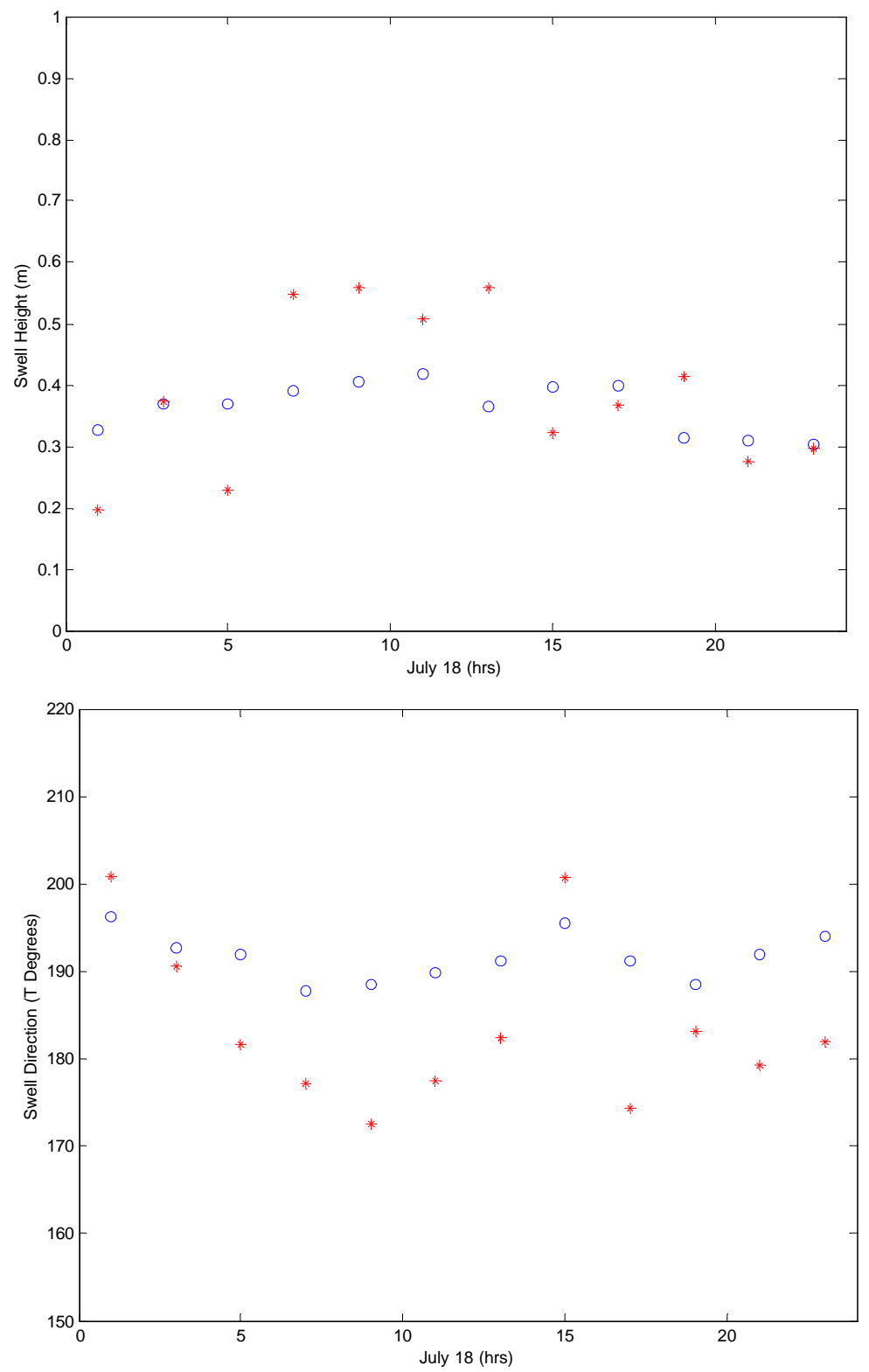


Figure 42: (a) Swell height and (b) swell direction on July 18, 2001 at Bass Strait as measured using COSRAD data (asterisks). Compared with directional wave buoy measurements (circles).

With an initial examination of the output of swell direction successfully completed, the remaining data collected for the Bass Strait deployment was analysed. Swell direction was examined first for both Portsea and Ocean Grove measurements over the entire length of the deployment. It is immediately noticeable that the results appear to be grouped into two distinct bands, (Figure 43). At Portsea the data was divided between one band positioned about the wave buoy values at 200 degrees and another band positioned around 300 degrees. Ocean Grove experienced a similar effect with one band surrounding the wave buoy values and the other around 100 degrees. In both cases there are few results scattered between the bands. If this banding is noise induced and the band that is approximately 100 degrees, in both cases, away from the wave buoy values is considered to be noise affected then there should potentially be a gap in this noise band during the phase of stronger swell conditions on July 17 to 18. This phase is marked in Figure 43 by arrows and highlights a distinct gap in the noise band. This noise gap is slightly longer in the Portsea record than the Ocean Grove record which supports the fact that the Portsea station is positioned better to monitor the swell from this direction.

The banding occurs because of the oblique angle at which each station is observing the swell. Correctly plotted data will be positioned at relatively high gradients on one side of the synthetically derived curve. Noisy data are also more likely to be positioned on these steep slopes than at the minima due to the shallow nature of the synthetic curve. On this shallow portion of the curve there is only a small variation in gradient that covers a large range of directions. Those directions between the bands shown if Figure 43 fall in the shallow portion of the synthetic curve. Conversely the gradients on the sides of the curve vary significantly over a small range of directions producing the narrow band of results. This geometry is somewhat favourable for providing accurate directional information however the radar analysis must have a method of excluding the directions that result from noisy data without consulting the wave buoy. A measure of data quality that will distinguish parameters resulting from noisy data and those derived from clean second-order peaks is required. This can be done by examining the quality of fit of the straight line to the  $R_{swell}$  values. If there is a large variation of  $R_{swell}$  values about the straight line the fit quality will be low and the error of fit value will be high.

The error in the fit of a straight line through the  $R_{swell}$  values is calculated as:

$$Err = \frac{2\mathbf{s}}{\Delta x} \tag{35}$$

where s is the standard deviation of  $R_{swell}$  values about the line of best fit and  $\Delta x$  is the horizontal extent of the radar data. Note  $\Delta x$  is not always a constant 60 degrees, ie extent of a sweep, as there may have been outliers eliminated in previous processes. This error gives an indication of the level of noise present in the spectrum and therefore is expected to have an inverse relationship with the height of the swell. This relationship is shown in Figure 44, where the error in the slope over the deployment is compared to the swell height as measured by the wave buoy. When the swell height is at its lowest point, July 12, the error is high. Conversely, when the swell height is at its peak, July 17, the error is at its lowest. More specifically, when the swell height is above the  $Hs_{min}$ value the error will plateau at a low point and will not vary very much if swell height continues to increase. This allows us to use this measure of data quality to resolve the problem of banding in the directional results shown in Figure 43. Swell parameters resulting from data with a degree of error that is deemed unacceptable can be removed. This leaves only the swell parameters extracted from data with a low level of noise and high level of accuracy. The cut off value is determined empirically at the highest error level possible that still excludes obvious noise affected parameters. Inevitably some inconsistent parameters may pass through with error values close to the cut-off value. To determine this cut-off value for quality assurance, further comparison of the error over the course of the deployment with direction and height must be made. Figure 45 displays all three extracted swell parameters from Portsea station with corresponding wave buoy validation and the error plotted adjacently for easy comparison. This highlights the relationship between the reduction in error and the increased accuracy in the directional parameter. The phase of low error, between July 16 and 19, matches perfectly with an increase in directional accuracy. We can therefore use the boundaries of this phase to determine the maximum error of fit allowable for the accurate extraction of swell direction. This relationship is also

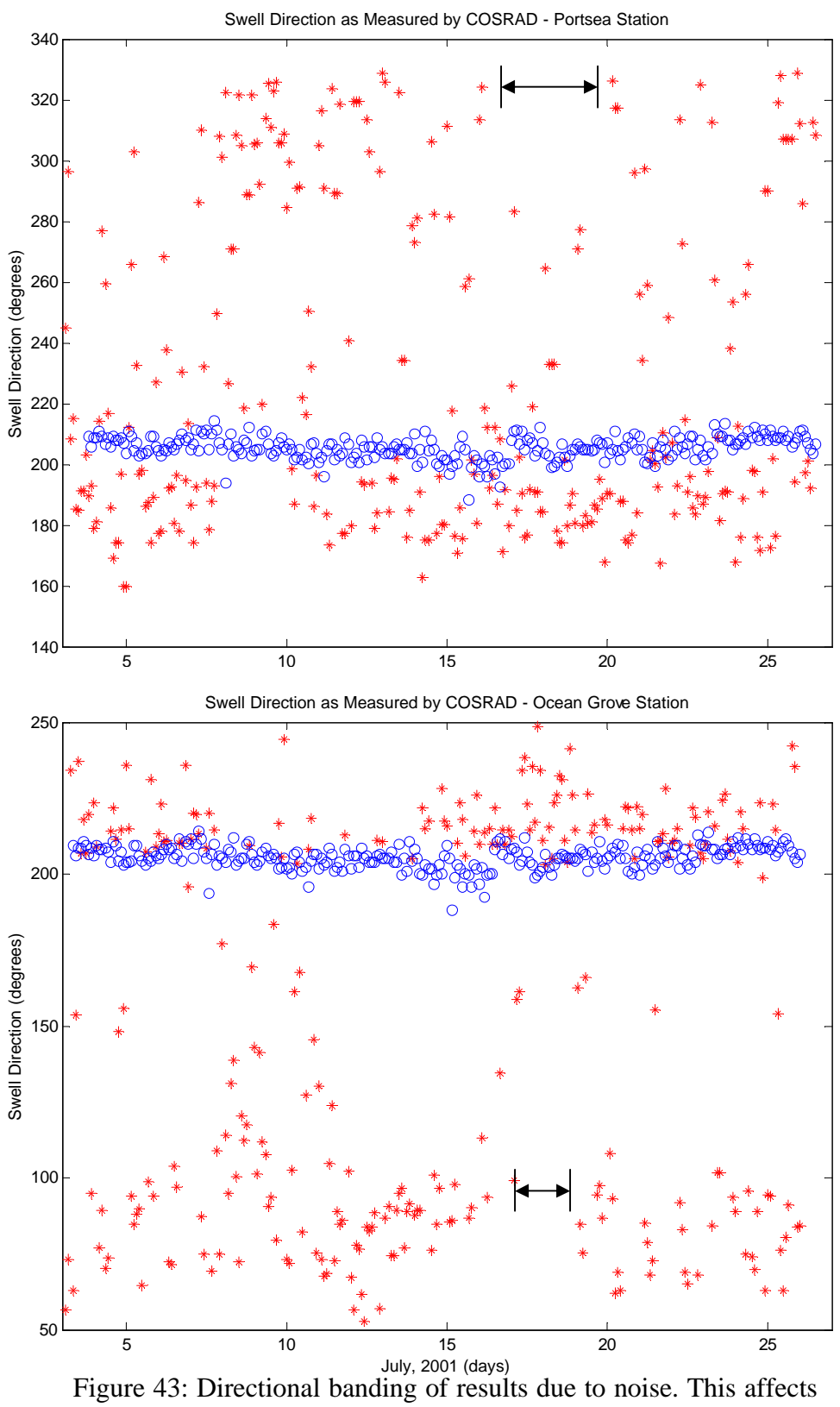


Figure 43: Directional banding of results due to noise. This affects the fitting routine by providing inaccurate gradients to match the theoretical curve. This banding is present in both Portsea and Ocean Grove results. (? Wave buoy and \* COSRAD)

seen in the swell height record (Figure 44) and will also be used to determine the cut-off value. The automation of this process is yet to be developed and the maximum allowable error has been estimated for this project using the empirical method described above.

The calculated parameters at Ocean Grove (Figure 46) display a higher degree of noise than those calculated from Portsea data. The swell height parameter suffers markedly in comparison and the swell direction is measured accurately for a shorter period of time. This is due to the less favourable geometry between the Ocean Grove station bore sight and the propagation direction of the swell waves. This will be discussed in more detail later.

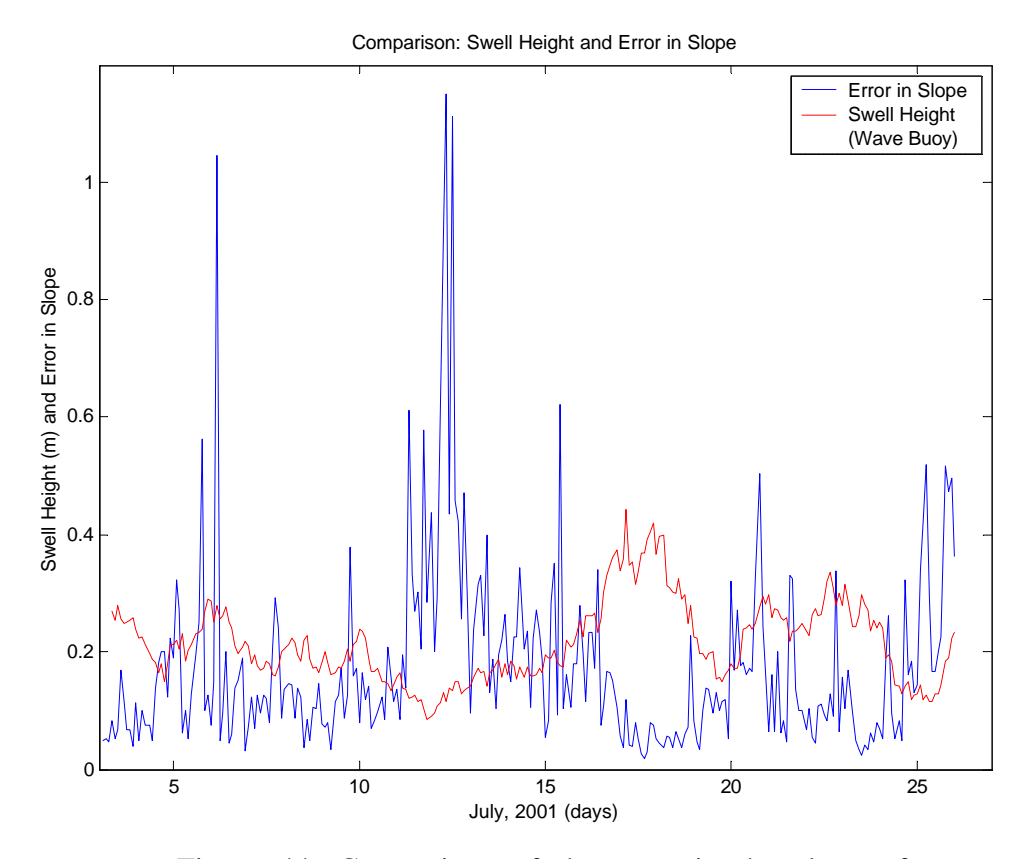


Figure 44: Comparison of the error in the slope of COSRAD data and the swell height as measured by the wave buoy (dotted line). The error reaches a minimum when the swell height is at its peak.

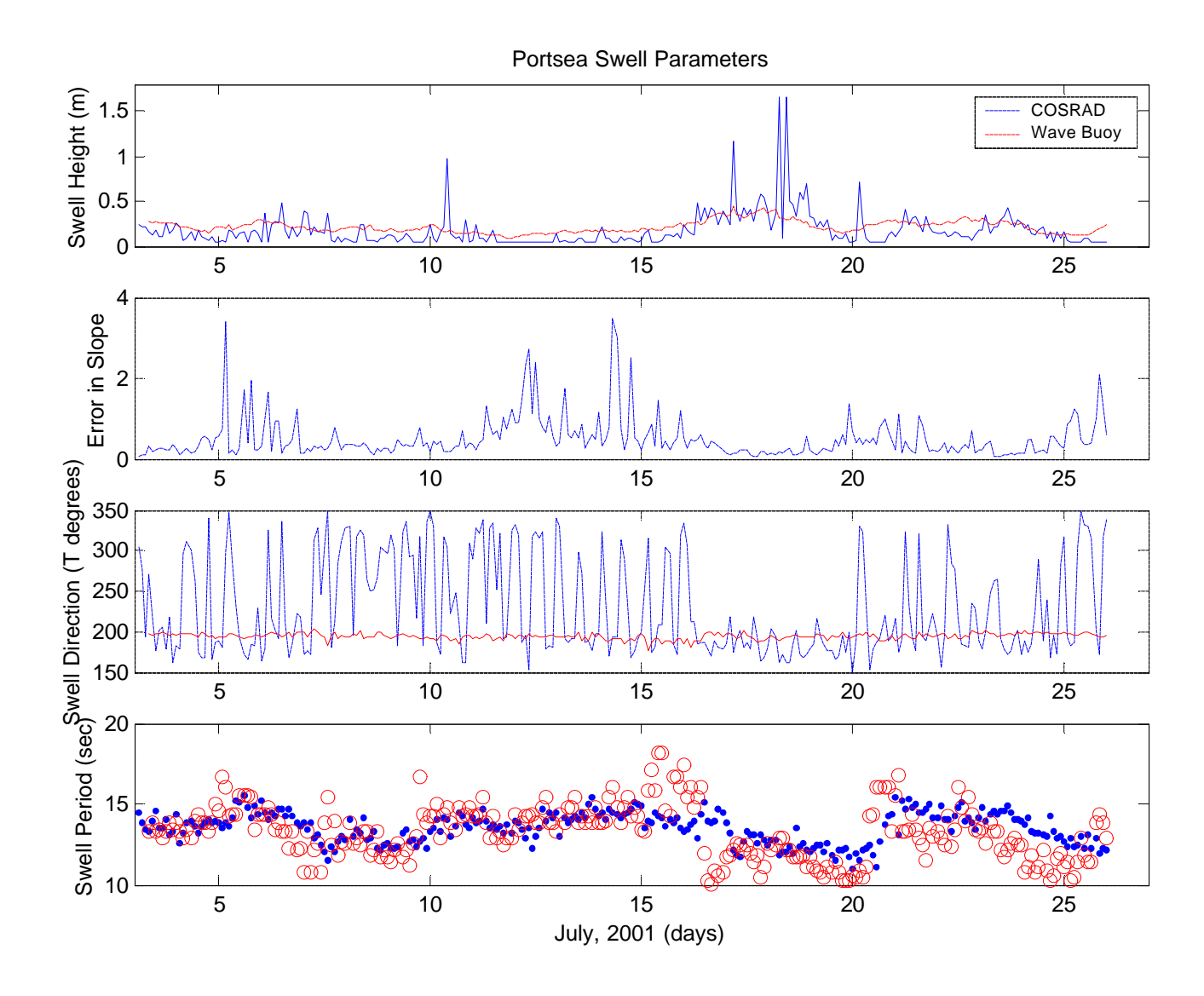


Figure 45: Comparison of swell parameters extracted from COSRAD data at Portsea and Waverider Buoy. The quality of fit parameter is shown in order to compare this with the wave height and accuracy in results. The parameters were calculated from averaged COSRAD data at pixel ranges 3 to 6. In each case the dashed line and oindicates wave buoy data and the solid lines and circles represent COSRAD data.

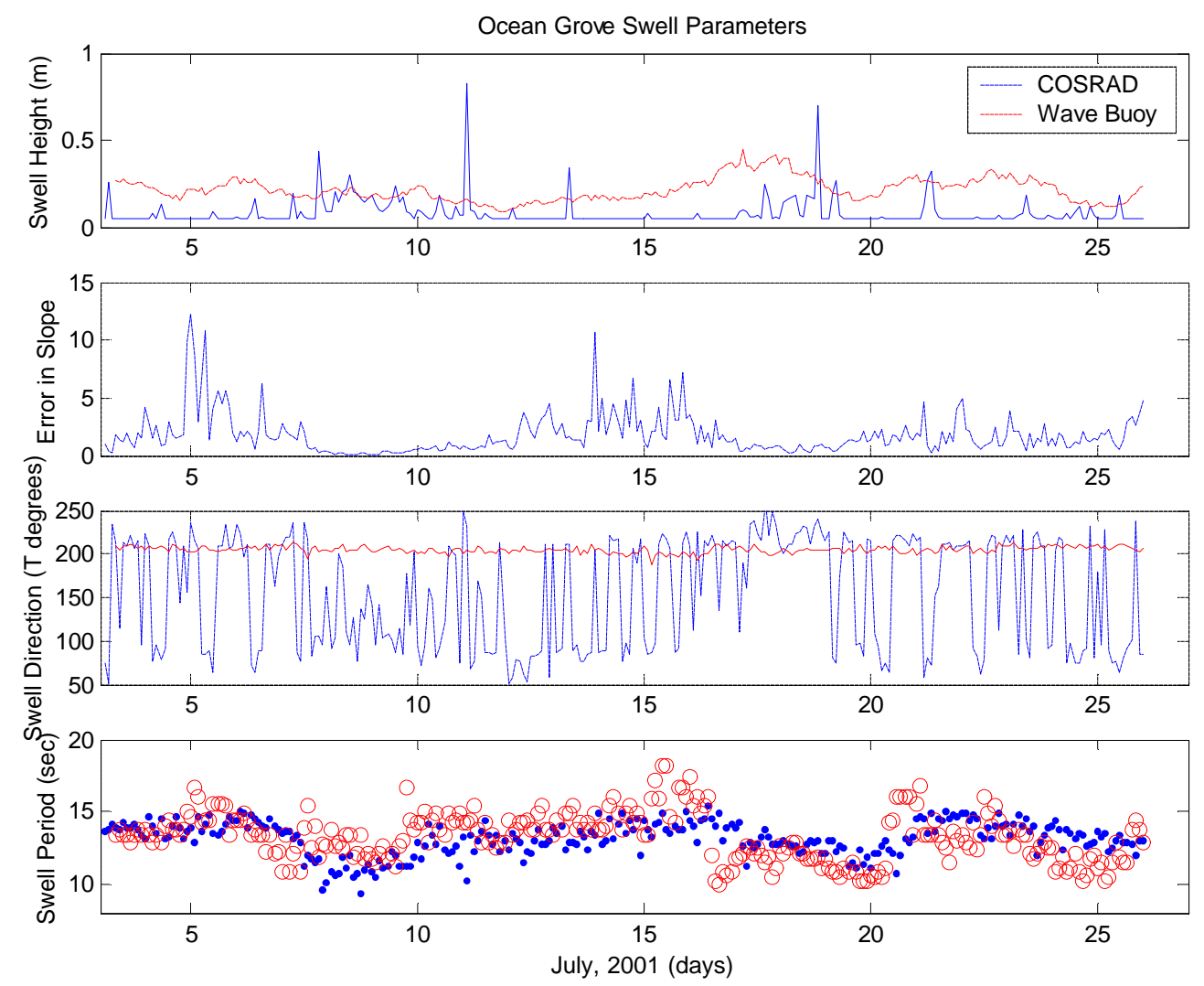


Figure 46: Swell parameters extracted from COSRAD data at Ocean Grove. Due to the positioning of the radar the Ocean Grove station provides less accurate results. Note the increased scale of the error in slope parameter. These parameters are calculated from data averaged COSRAD data over pixel ranges 3 to 6.

An error cut-off value of 0.1 was chosen with consultation with Figure 44 in order to remove swell directions and heights that appear to be the result of data extracted from noisy Doppler spectra. This cut-off value removes the majority of erroneous values form the directional record, many of which were in excess of 100 degrees from the wave buoy measurement. A distinct data gap can be seen between July 10 and 16 where the error values were too high due to the weak swell conditions at that time (Figure 47). However, the spread of the COSRAD values is now approximately ±20 degrees about the wave buoy measurements as opposed to ±10 degrees that was achieved in the test earlier (Figure 42b). This reduction in accuracy is the result of the inclusion of measurements with error values close to the cut-off mark. Some overlap around the cut-off value is unavoidable, allowing some unwanted values to be accepted. Reducing the cut-off value further would remove these values, although it would be at the expense of some legitimate results.

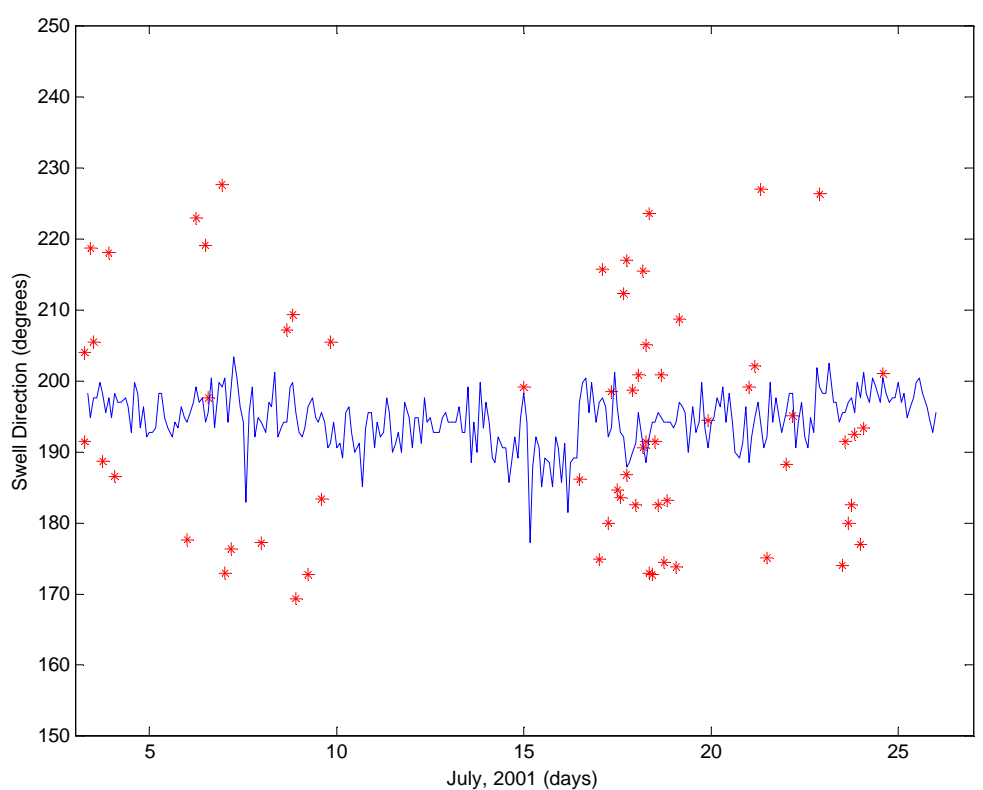


Figure 47: Swell direction as measured by COSRAD (\*) within the designated error cut-off value of 0.1. The cut-off value was found using error values from Portsea. These results are compared to the directional wave buoy (solid line).

Similar results are achieved when the cut-off routine is applied to the swell height data (Figure 48). The gap in the data between July 10 and 16 is again evident and a small increase in the spread of the results about the wave buoy is noticeable when compared to Figure 42(a). Due to the overlap around the cut-off value the spread has increased from 0.1 m during strong swell conditions, to approximately 0.15 m. This is still a good result, particularly when the swell height is close to only 0.2 m in height.

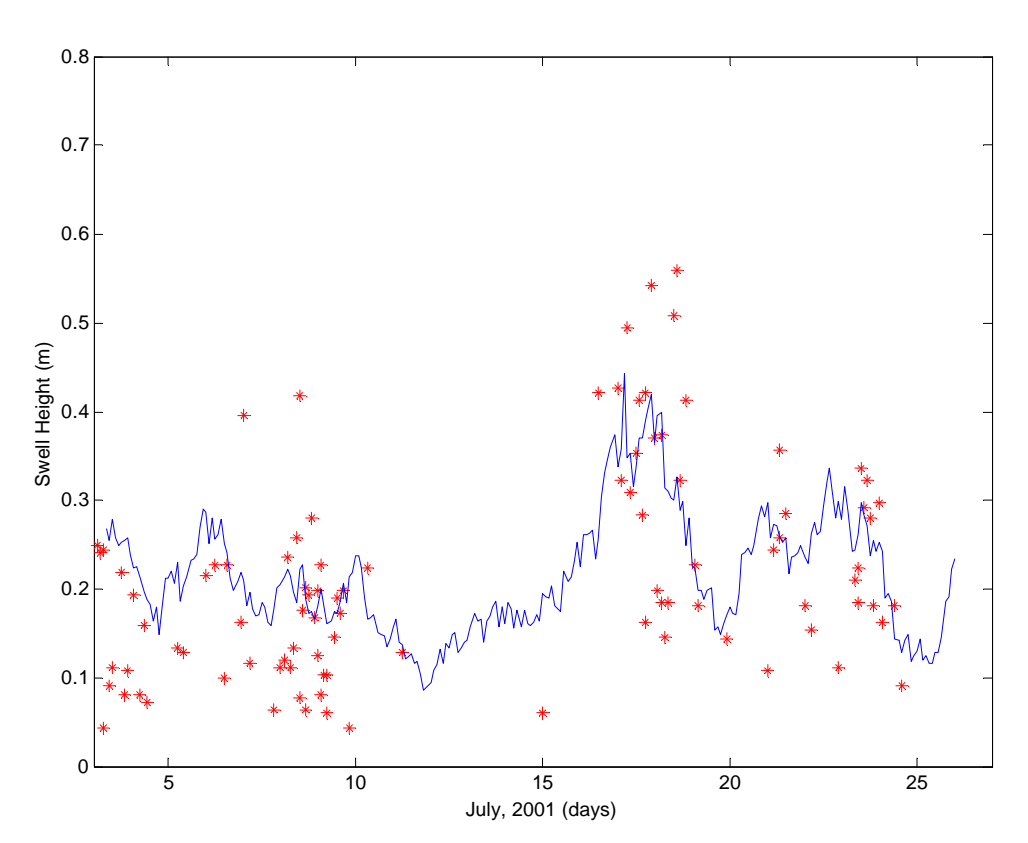


Figure 48: Swell wave heights as measured by COSRAD (\*) within the cut-off value of 0.1 as was used for swell direction. The wave buoy is represented as the solid line.

## **6.4** Range Limits

The limits of the algorithm in terms of minimum and maximum swell height,  $Hs_{\min}$  and  $h_{sat}$  respectively, have already been discussed and evaluated. The remaining possible limitation is the maximum range at which quality parameters can still be extracted. This can be evaluated by finding the error in the slope of  $R_{swell}$  values at increasing range bands until it exceeds the level from which reliable information is currently being extracted at near shore ranges. This maximum range may be dependent upon each station's viewing angle. It has been noted that there is more noise present in the directional parameters extracted from Ocean Grove data than Portsea, primarily due to poor viewing angle. If a station has a higher level of noise at near shore ranges then any addition to this noise level by propagation loss as the range increases may result in one station having a shorter working range than the other.

This was tested by evaluating the swell parameters from July 3 to 26 at increasing ranges. Parameters from pixels 3 to 6 have already been measured and will be used as the benchmark for more distant pixel bands. The COSRAD system at Bass Strait was configured to measure up to 12 pixels per sector. Therefore, averages of pixels 6 to 9 and 9 to 12 were processed by the algorithm to extract parameters including the quality of data, swell height, direction and period. These ranges were then compared to the parameters extracted from pixels 3 to 6.

### 6.4.1 Portsea Range Limit

If the increasing range affects the quality of the data to the extent that the second-order peaks become confused by noise, the error in the  $R_{swell}$  values should increase. This is not the case with the data from Portsea. The error lines for data collected by the COSRAD station at Portsea are shown in Figure 49 for the three consecutive pixel bands mentioned above. To simplify the comparison of the three ranges the error has been arranged in descending order for each range band. If the error has increased with range we would expect to see the lowest error at a higher value for the more distant ranges. Figure 49 shows the errors in the three tested range bands are all relatively

consistent with each other across the deployment. In fact the data from the most extreme range, pixels 9 to 12, performs as well as near shore bands and lacks the high error peaks seen at numerous stages throughout the deployment in the 6 to 9 band. Most importantly, all three range bands reach the same minimum error value which indicates that the increase in range does not affect the performance of the algorithm. This is at least true for ranges up to 12 pixels (36 km) with this swell observation angle.

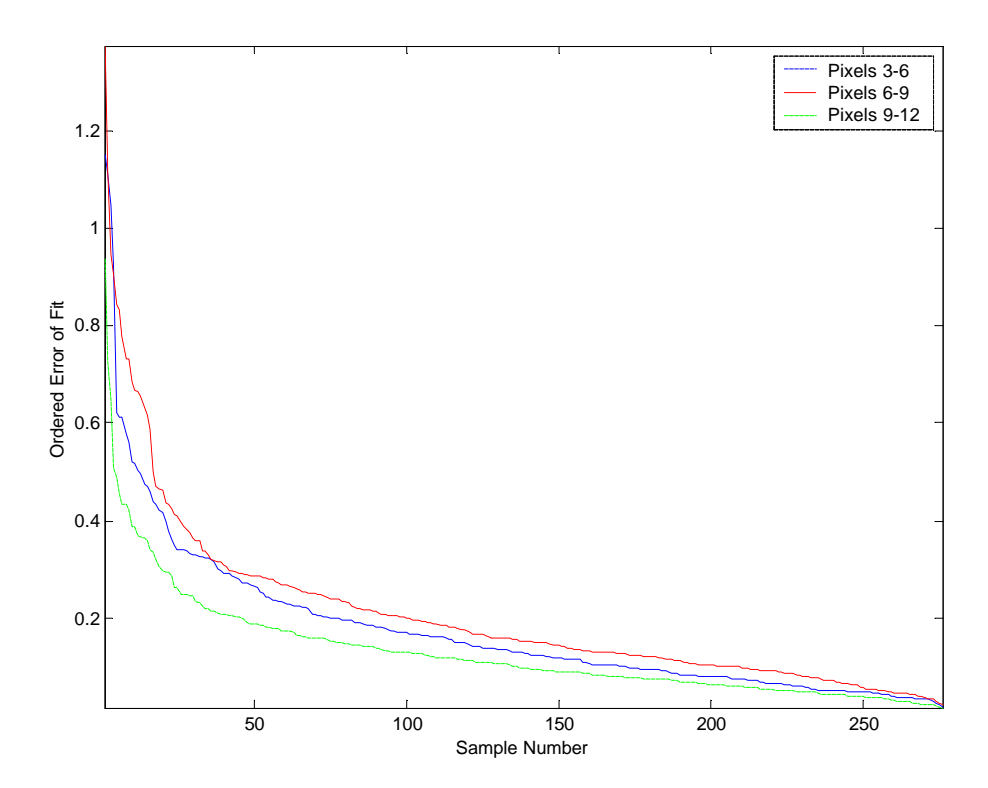


Figure 49: Comparison of the error in the fit of a straight line through  $R_{swell}$  values at increasing range. The error at each range has been ordered from highest to lowest for ease of comparison. Data shown is from the Portsea station.

### 6.5 Discussion

The swell conditions during the deployments at Tweed Heads and Bass Strait are classified as low (Table 2). With the available data swell heights between 0.2 m to 0.96 m have been accurately measured. The accuracy of the algorithm is reliant on its ability to identify the swell peaks in the spectrum which are more prominent when the swell is stronger. Therefore, it is reasonable to assume that the algorithm would continue to accurately measure swell up to the saturation point ( $h_{\rm sat}$ ) of 3.18 m. We can measure swell categorised as low to moderate (Table 1), which covers the most common range of swell heights in these regions. At present there is debate as to the major cause of coastal erosion. It is already known that extreme events involving heavy swells produced by storms are responsible for much coastal damage however, the constant action of low to moderate swell may have a greater impact in the long term. This algorithm in conjunction with COSRAD system could be used to aid in the quantification of impact by lower energy swell waves. It would be also be desirable to monitor waves in the heavy category as they are capable of causing much damage to shipping, particularly in the coastal zone; however, it is possible to use this algorithm in the future to predict imminent heavy swells by issuing a warning once the wave height has exceeded the saturation limit of the spectrum.

Limits to measurement including minimum swell height and maximum range, related to scattering strength and propagation losses were evaluated for both deployments. Swell height is the dominant factor in achieving reliable signal strength. The swell angle in relation to the bore sight of the radar can alter the  $Hs_{\min}$  value. Weaker swell may produce reliable information if the radar is in a favourable position or conversely the value of  $Hs_{\min}$  may increase with poor radar positioning.

A dual radar system with an orthogonally intersecting configuration is not optimal for monitoring swell with this algorithm. However, as shown here, information can still be extracted if the swell is propagating in a favourable direction. If the beam to swell angle is appropriate, only one station is required to produce information on swell waves. This algorithm was developed to work with a system configuration optimized for the

measurement of surface currents. In this way the amount of information collected on the sea surface at any point in time is maximised and is therefore more cost effective. If the sole purpose of a deployment was for swell wave monitoring the radar geometry would be different. To maximise the accuracy and recovery of swell information using this method, multiple radars would be positioned so that each sweep does not overlap but run consecutively to increase surface coverage. If it was feasible to run three COSRAD systems simultaneously, a full 180 degrees of ocean surface could be monitored (Figure 50). The diagram assumes a straight coastline with three COSRAD systems at the same location with differing bore sights.  $q_{B2}$  is directed perpendicular to the coastline and therefore  $q_{B1}$  and  $q_{B3}$  are directed at  $\pm$  60 degrees from  $q_{B2}$ . The extreme beams of each radar sweep are then aligned without overlapping and ocean coverage is maximized. This would prevent the problems encountered with the radar configuration used in the deployments at Tweed Heads and Bass Strait. When the swell is propagating from a direction that positions  $R_{swell}$  values on the cusps of the stylised FM curve, data from an adjacent station would provide reliable results.

An automation process to determine which radar is in the best position to observe the swell at any given time needs development for a system such as this to work without user input. In the case of this project where the algorithm was not running in real-time it is simple to calculate which station is favourably positioned and likely to produce the most reliable parameters. A real-time method may rely on constant feedback from the algorithm providing information on the position of the  $R_{swell}$  values on the FM curve. After a nominated number of occurrences where the  $R_{swell}$  values are positioned on the cusps of the curve the next, adjacent, station can provide parameters for real-time examination.

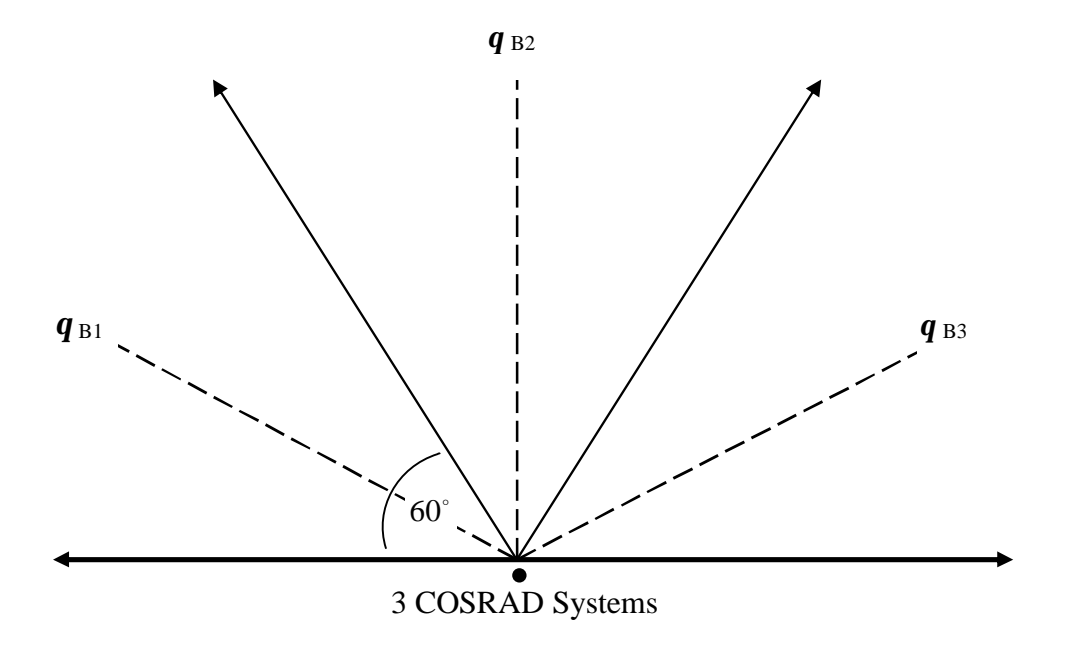


Figure 50: Diagram showing the optimal radar configuration for swell wave measurement using the frequency modulation method.  $\boldsymbol{q}_{B1}$ ,  $\boldsymbol{q}_{B2}$  and  $\boldsymbol{q}_{B3}$  represent the bore sight direction for each of the three COSRAD systems. The solid lines represent the extreme beams of each radar.

# **Chapter 7: Further Extensions to the HF COSRAD System**

Although the main focus of this thesis is the extraction of swell wave parameters, other extensions that can be made to the COSRAD system by utilizing the considerable data sets collected during the deployments at Tweed Heads and Bass Strait were explored. These include the development of a new technique to resolve an inherent ambiguity involved in the calculation of wind direction from HF radar spectra. The extraction of wind direction is calculated using the ratio of energy in the first-order Bragg peaks. The resonant 5 m Bragg waves that produce the first-order peaks in the Doppler spectrum quickly align themselves with the local wind conditions. We can therefore use the information carried by these peaks to find the wind direction in the area covered by the radar. The strength of a Bragg line is dependent upon the component of wind in the particular direction of the radar beam. For example, if we have a Doppler spectrum with a strong Bragg line in the positive half of the spectrum and a weaker Bragg line in the negative half, then we know there is a component of the wind propagating towards the radar. To resolve this component completely, consultation with spectra from the second HF radar is needed. This has become a fairly routine application for HF radar systems (Long and Trizna, 1973, Stewart and Barnum, 1975, Fernandez et al., 1997) however there are areas in which the extraction methodology can be improved.

The new methods presented here rely on established theory from Heron and Rose (1986) to extract wind direction from HF radar spectra and are concerned mainly with an alternate and robust way of resolving an ambiguity inherent in those solutions. These methods are basically a means of comparing data acquired by the two stations and resolving the ambiguity through a test of maximum likelihood. Recent work in determining wind directions and rms wave heights using the COSRAD system by Heron and Prytz, (2002) and by Huang et al. (2003), found a method of removing the ambiguity using data from a single radar station. They also presented methods for the evaluation of the spreading function. The spreading parameter, S, (Longuet-Higgins *et al.*, 1963) was not initially taken in to consideration in the development of the methods here and was given a nominal value for the evaluation of the algorithm. A more accurate estimation of the spreading parameter was found later by statistical means.

For the Tweed Heads deployment, wind speed and directional data was collected from anemometers at three locations. Anemometers at Coolangatta Airport and the Gold Coast Seaway logged both wind speed and direction at half hourly intervals throughout the duration of the deployment. Observational data was also collected from the Kingscliff Volunteer Coast Guard. Wind speed and direction was recorded 4 times daily at this site which is situated less than 100 m from the Kingscliff COSRAD station. Synoptic weather charts were also consulted as a means of describing the meteorological conditions at the time of deployment.

## 7.1 Wind Direction Algorithm

The difference in methodology here compared to existing models lies in the management of the inherent ambiguity in the angle resulting from individual radar spectra. Given that f is the direction of wind with respect to the azimuth of the radar beam,

$$\mathbf{f} = \left| 2 \arctan \left( R^{\frac{1}{2}S} \right) \right| \tag{36}$$

where R is the ratio of the two first-order Bragg peaks and S is the spreading factor (Longuet-Higgins *et al.*, 1963). Therefore, from a single spectrum there is an uncertainty as to which side of the radar beam f should lie. This is shown graphically below (Figure 51). It is not possible to solve this ambiguity for  $q_w$ , where  $q_w = \pm f$ , using a single beam azimuth. This can be resolved by utilizing information from the second COSRAD station. The COSRAD system is usually deployed in pairs and positioned so that their beam intersections are close to orthogonal in order to resolve surface current parameters. This ambiguity can only be resolved and thus directions can only be found where there is an overlap in coverage between the two stations. Note that all wind directions in this chapter are given in vector notation.

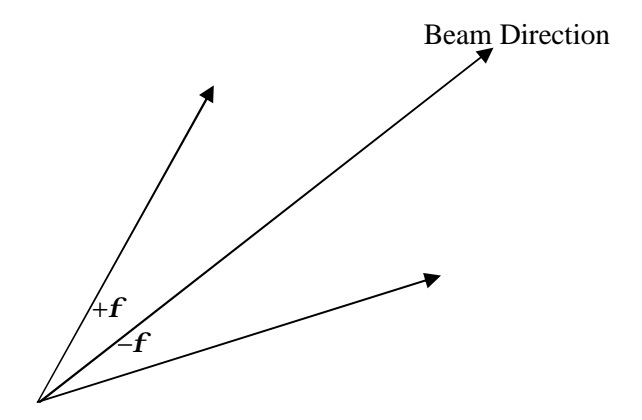


Figure 51: Graphically shows the inherent ambiguity in the calculation of wind direction from a single spectrum.

To resolve the ambiguity it is necessary to know exactly which pixels from each station illuminate the same part of the ocean surface. This was done accurately using spherical geometry to calculate the range and angle, in degrees East of North, from each station.

Angle A, in Figure 52, can also be defined by,

$$A = Long_{P} - Long_{S} \tag{37}$$

where  $Long_P$  and  $Long_S$  are the longitude of the pixel and the longitude of the station respectively. From spherical trigonometry it is given that,

$$\cos a = \cos b \cos c + \sin b \sin c \cos A \tag{38}$$

and substituting in the known values from Figure 52 this becomes,

$$\cos(Range) = \sin(Lat_p)\sin(Lat_s) + \cos(Lat_p)\cos(Lat_s)\sin(Long_p - Long_s)$$
(39)

Given this it is possible to calculate the distance (range) in kilometres by,

$$Range \_km = R_{\scriptscriptstyle P} \times Range \tag{40}$$

where  $R_{\rm e}$  is the radius of the earth which is 6378.137 km (International Union of Geodesy and Geophysics, 2002). The angle of the range line in degrees East of North can be calculated using,

$$\sin B = \frac{\sin b}{\sin a} \sin A \,, \tag{41}$$

and substituting in the known values from Figure 52 this becomes,

$$\sin B = \frac{\cos(Lat_p)}{\sin(Range)}\sin(Long_p - Long_s) \tag{42}$$

This angle can be used in conjunction with the bore sight for each station to determine the sector in which this pixel is situated. The calculated range value can be used to identify a pixel in that sector, given that the spatial resolution of the COSRAD system for the Tweed Heads and Port Phillip Bay were designated at 3 km. Therefore this method can utilize a grid of points in the coverage area and determine the corresponding sector number and pixel number for each station at that point. The spectra from each station can then be examined and equation (36) can be applied to find the wind direction relative to the radar beam at that location in the grid.

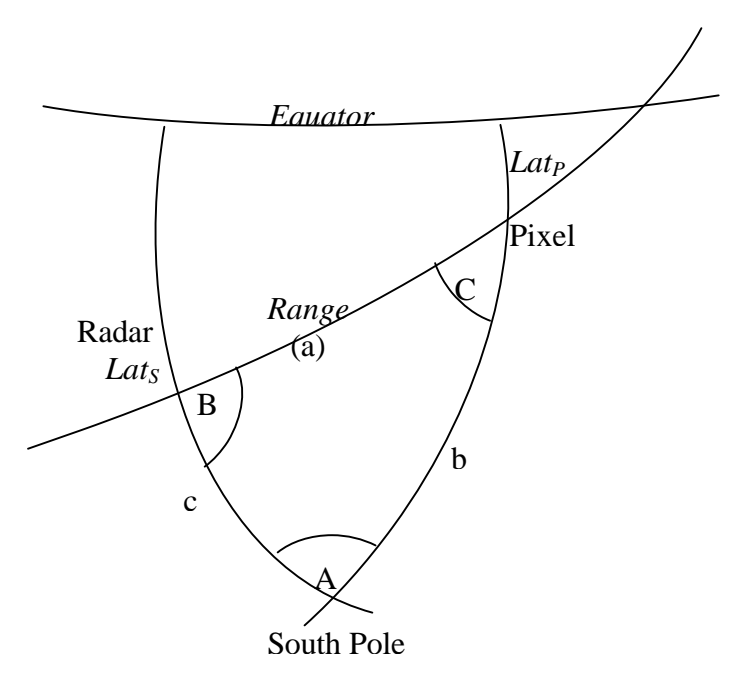


Figure 52: Spherical system with labelled sides and angles used to calculate the range from a station to a particular pixel and the angle of that range line with respect to North. Where Lat<sub>S</sub> is the latitude of the station and Lat<sub>P</sub> is the latitude of the pixel.

Previous models have used statistical methods to resolve the ambiguity with mixed results. A more robust selection routine presented here uses the positive and negative wind directions as calculated from each station to determine the most likely pair of directions. The routine compares the positive and negative directional values from both

stations by finding the absolute difference between all possible combinations which results in an array of 4 values, as shown in Table 1 below, of which the minimum will relate to the most likely pair of correct directions.

$$\frac{\left| (+S1) - (+S2) \right|^{\text{(a)}} \left| (+S1) - (-S2) \right|^{\text{(b)}}}{\left| (-S1) - (+S2) \right|^{\text{(c)}} \left| (-S1) - (-S2) \right|^{\text{(d)}}}$$

Table 1: Shows the possible combinations of station comparisons. Where S1 is Station #1 and S2 is Station #2.

For example if cell (b) in Table 1 was the minimum then the chosen directional pair would be the positive direction from Station 1 and the negative direction from Station 2. On most occasions this method chooses the correct pair and a single value is then calculated from the average of the two selected directions. However, if two combinations in Table 1 happen to be very similar then the incorrect pair may be selected. As a precaution, a quality factor is assigned to each decision as an indication of confidence. This quality value is calculated as the ratio of the two smallest differences. Therefore if the chosen difference is half that of the next closest difference the quality value is 2. If this was the case then we would be reasonably confident that the correct pair had been chosen. If the quality value is less than 2 then a second routine is used to check if the decision is reasonable by comparing it with accepted values immediately preceding it in the grid.

## 7.2 Algorithm Validation

Once wind directions have been resolved for the entire grid and any quality concerns have been addressed, the values in the grid can be displayed graphically, as shown in Figure 53. This map of wind directions can then be compared with directional data available from the validation sites mentioned previously. As an example, the directional map produced by COSRAD on March 5, 2001 at Tweed Heads will be validated. This date corresponds to the 22<sup>nd</sup> day of the deployment. Data from Coolangatta Airport (28.17° S, 153.50° E) and the QBPA wave buoy will be used to show the agreement in

wind direction at this time. Although figures from Coolangatta Airport only are shown here, data from the Gold Coast Seaway (27.94° S, 153.43° E) also support the findings extracted from the HF radar and could also be used to further validate the results. March 5 was chosen as a day of interest not particularly because of the wind conditions but for the strong swell conditions. For this reason, this day was examined closely and the data used repeatedly to refine new developments to the COSRAD system.

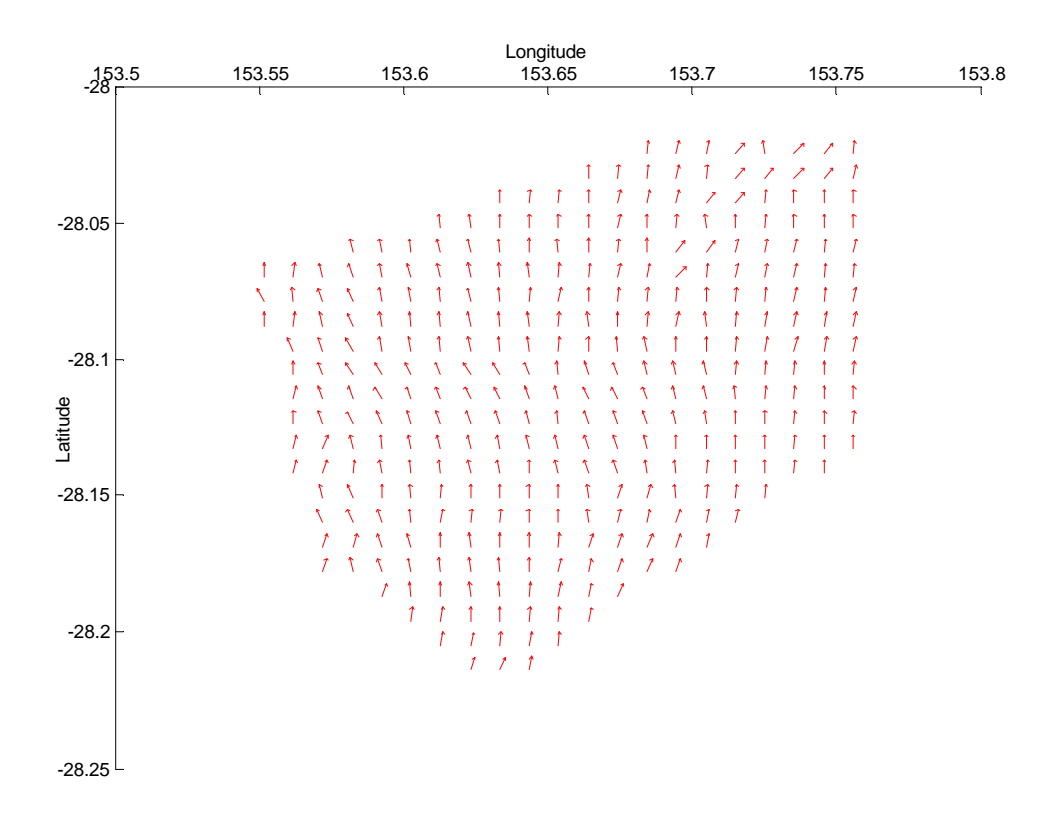


Figure 53: Average of 4 directional wind maps as measured by COSRAD between 10am and 12pm on March 5. A nominal value for S was used to produce this (S=2). The dominant wind direction at this time was towards the North.

The deployment began with relatively calm wind conditions that rarely exceeded wind speeds of 5 m/s. Much stronger wind conditions were observed on two occasions, between the 5<sup>th</sup> to 10<sup>th</sup> day of the deployment and again from the 20<sup>th</sup> to the 25<sup>th</sup> day. During these periods wind speeds reached up to 13 m/s and are generally in excess of 10 m/s. These periods can be seen in Figure 54 as seen from Coolangatta airport.

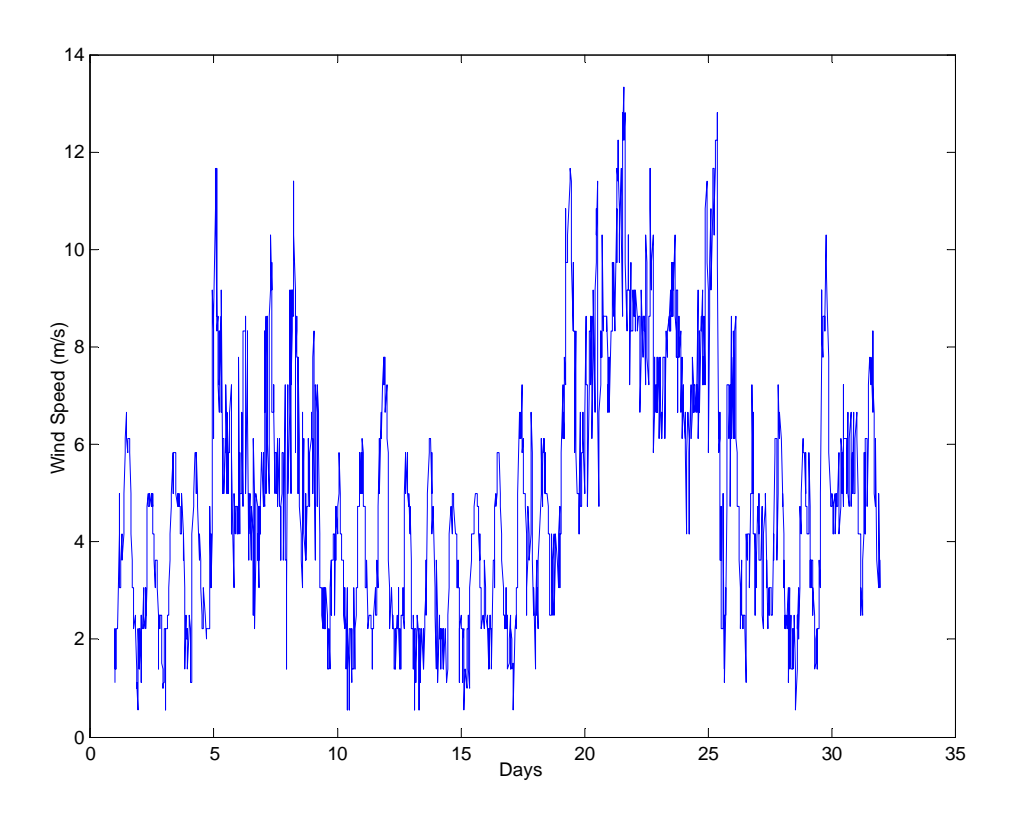


Figure 54: Variations in wind speed at Coolangatta airport over the duration of the COSRAD deployment at Tweed Heads.

By considering directional information in conjunction with the information on wind speed, it becomes easier to understand the conditions and distinguish between the two distinct periods of strong wind and the background weaker periods. The two figures below (Figure 55(a) and (b)) display the calculated Eastward and Northward components of the wind speed. The weaker conditions, less than 5 m/s, now stand out as simple diurnal variations in wind conditions, such as on-shore breezes. The stronger wind speeds noted in Figure 54 match periods of high wind speed in Figure 55(b) showing the Northward component of wind speed at Coolangatta Airport. On day 22 of the deployment, high wind speeds in the Northward direction correspond to and agree with the directional map produced by COSRAD at that time. This corresponds to a synoptic scale weather system positioned off the northern NSW coast (Figure 56). This low pressure system is producing the Northward winds that are seen at this time by the radar and validating data sets.

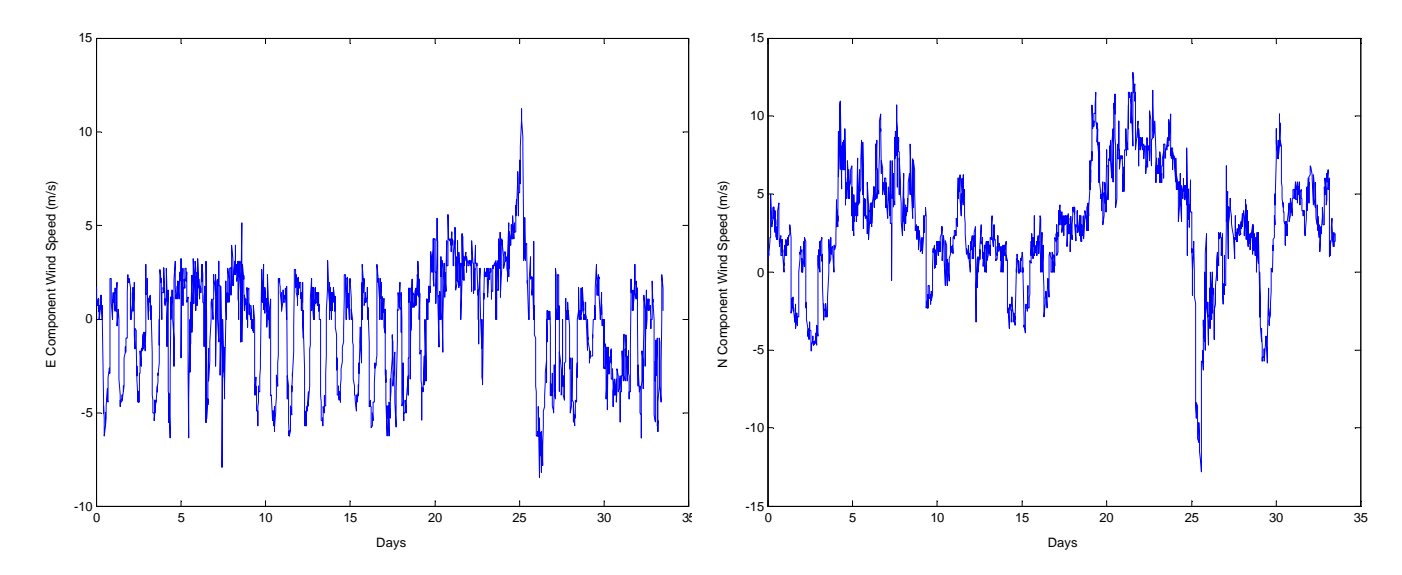


Figure 55: (a) Displays the Eastward component of wind speed, (b) Displays the Northward component of wind speed at Coolangatta Airport.

Further validation of this model can be inferred from the directional variation of wind waves as measured by the QBPA directional wave buoy. As the name suggests, waves of such a short period quickly align themselves with the wind direction and this wave buoy is positioned in the area covered by the overlapping sweeps of the two COSRAD systems. HF radar does not measure the wind parameters, or any other meteorological effects, directly. However, it utilizes the relationship with small 5 m Bragg waves (at 30 MHz transmit frequency) which respond rapidly to the wind conditions. Figure 57 shows the directional variation of wind waves throughout the deployment and with an initial inspection it appears that the wave buoy agrees with the radar measurements. Day 22 is marked to show that the wind waves at that time are moving in a Northward direction.

THE IMAGES ON THIS PAGE HAVE BEEN REMOVED DUE TO COPYRIGHT RESTRICTIONS

Figure 56: Synoptic weather charts, provided by the Bureau of Meteorology – Monthly Weather Review, for March 5, 6 and 7, 2001. The maps show a low pressure system off the northern NSW coast generating winds in a Northward direction.

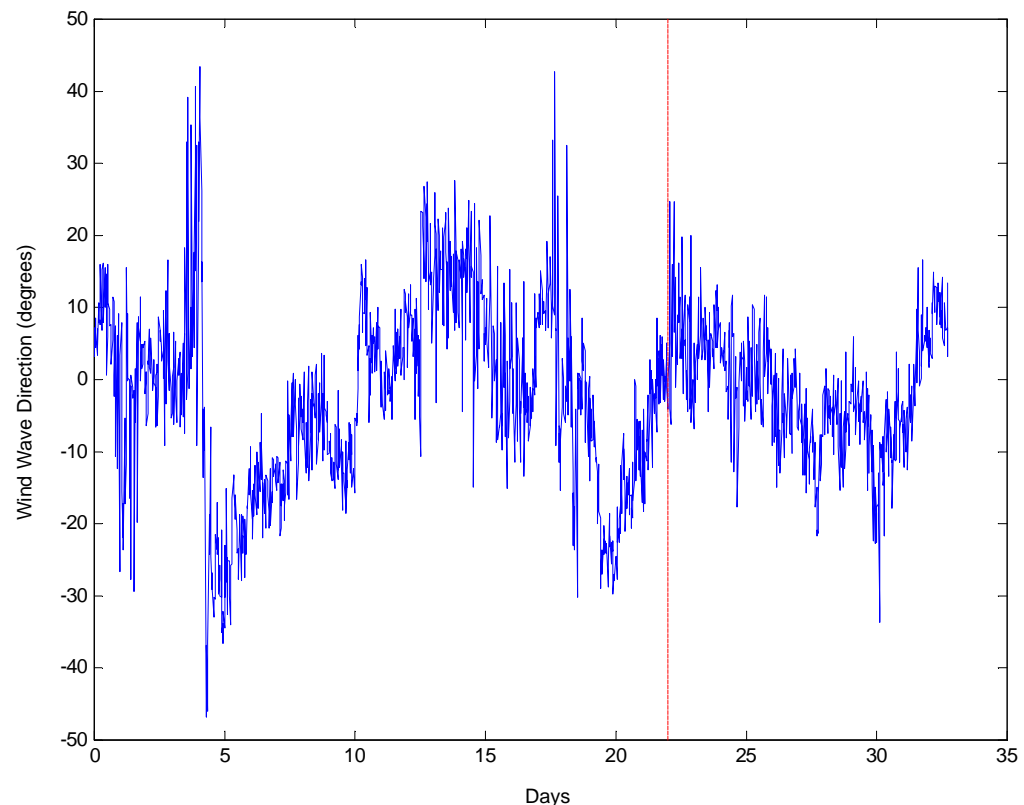


Figure 57: Directional variation of wind waves as measured by the QBPA Waverider directional wave buoy. The dashed line marks day 22 of the deployment.

In a more detailed validation, the algorithm was used to extract wind direction over a 5 day period, from March 3 to March 8 and compared directly to wind wave measurements collected by the wave buoy (Figure 58). The algorithm measurements being compared to the wave buoy are the closest intersecting pair of radar positions to the location of the wave buoy. The comparison shows the resolved wind direction from the algorithm and wind-wave directions from the Waverider buoy at hourly intervals. Agreement between the measurements is reasonable. At most times the accuracy is to within ±10 degrees however, slightly less accurate results occur during periods of transition in the wind direction such as the change from -5 degrees East on March 3 to -25 degrees East by the beginning of March 4. This is a common problem in determining wind direction from wave motion. The short waves may react quickly to changes in wind conditions however, transitional periods are usually accompanied by a lull in the wind speed and thus less accuracy is expected at these times. It is possible to improve

accuracy at this stage by finding the best possible spreading parameter value for the conditions over this time period. The following procedure for the determination of the spreading parameter was detailed by Heron and Prytz (2002). The method is simply to repeat the calculation of wind direction over the same period for different spreading values and find the mean and standard deviation of wind direction for each one. The standard deviation should reach a minimum at the best possible S value. This procedure was followed for S values of 0.5, 1, 2 and 3 with the results shown in Figure 59. A polynomial of degree 3 was found to be the best fit to the data and a distinct minimum at approximately S=1.4 can be seen.

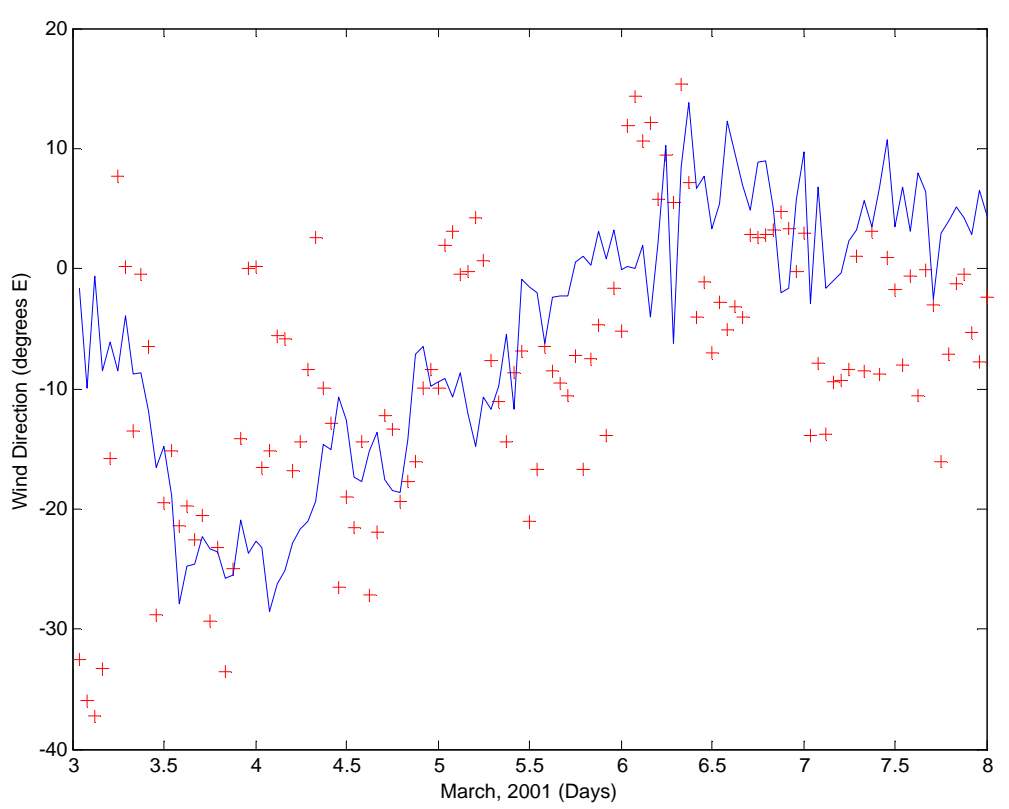


Figure 58: Wind direction as measured by the COSRAD system (+) and compared to the direction of wind waves as measured by the wave buoy. These measurements were calculated using S=2.

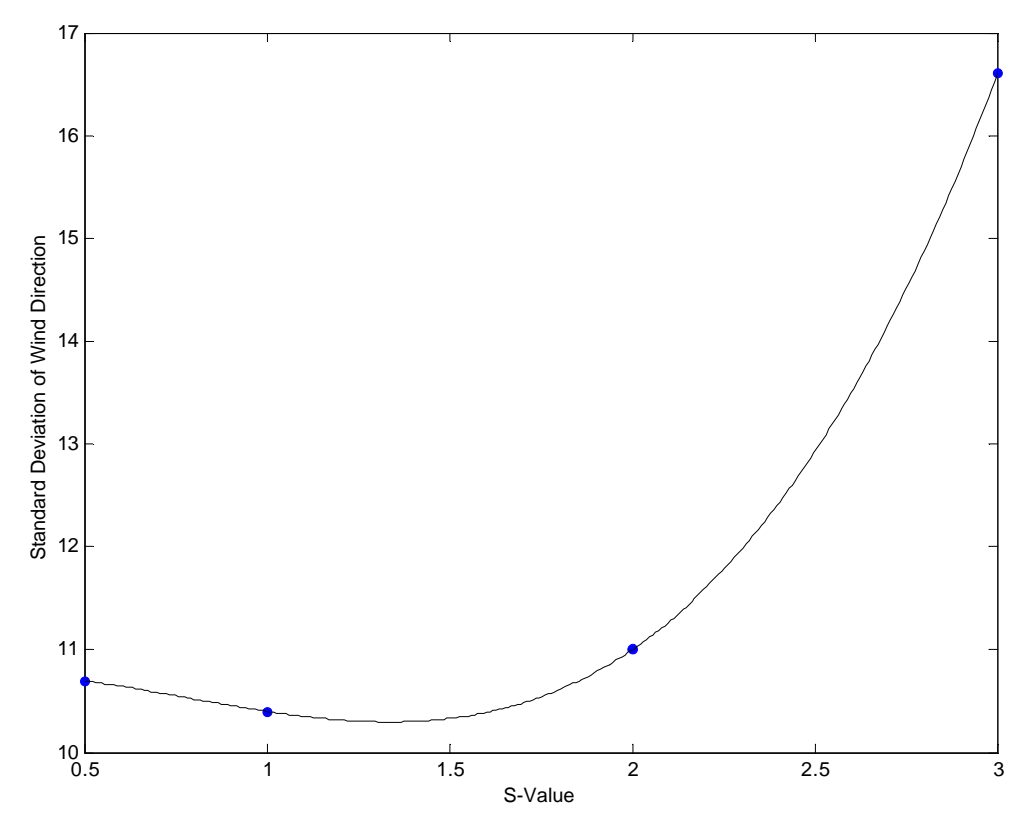


Figure 59: Standard deviations of wind direction over the period between March 3 and March 7 with changing values of S. A polynomial of degree 3 was fitted to the data and a minimum can be found at S=1.4.

The comparison of wind directions as found by the algorithm with an S value of 1.4 and the wind wave directions from the Waverider buoy can be seen in Figure 60. The comparison is an improvement over the results with S=2 (Figure 58). Better agreement at most stages of the test data set is found however, the algorithm still provides less accurate results during the changing wind conditions over the first two days of the test set in comparison with the following days. The change to -25 degrees East is still detected although a slightly higher degree of noise accompanies the results at this time.

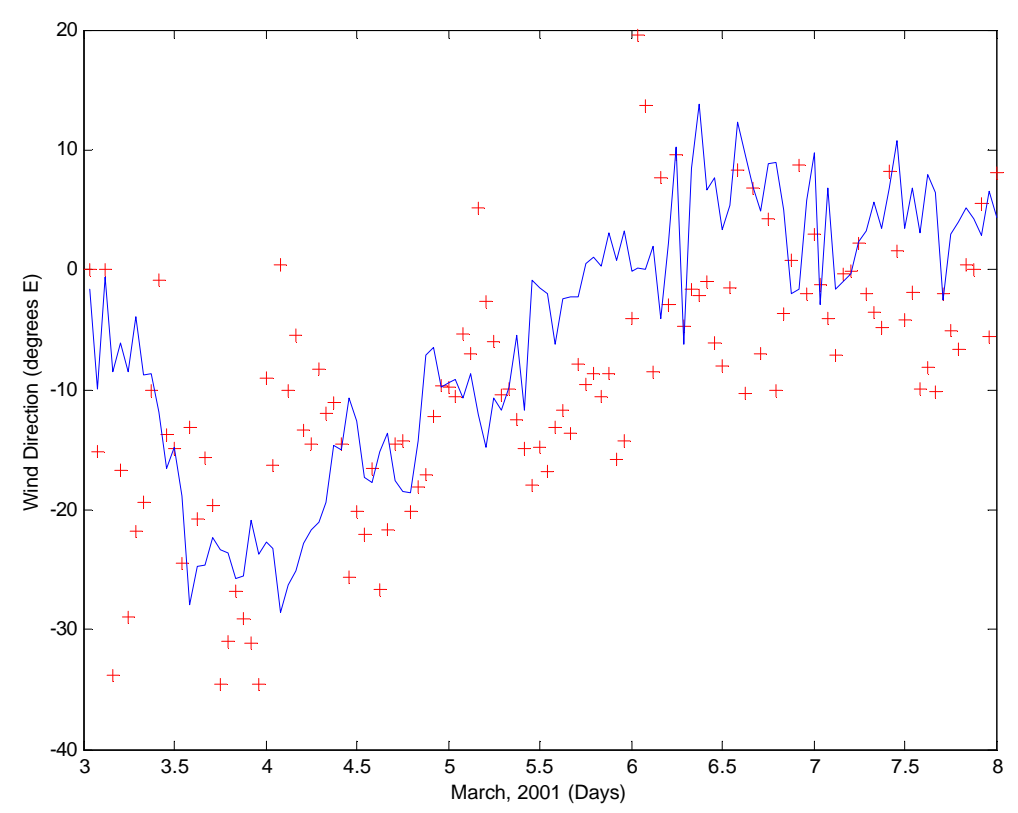


Figure 60: Wind direction as measured by the COSRAD system (+) and compared to the direction of wind waves as measured by the wave buoy. These measurements were calculated using optimum value for S (S=1.4) found in Figure 59.

### 7.3 Discussion

The algorithm presented here is simply an alternate method for the extraction of wind direction from HF Doppler spectra. The theory derived by Longuet-Higgins *et al.* (1963) is used in this algorithm as it is used in the extraction of wind parameters by other radio oceanographers however the difference in methods lies in the resolution of the ambiguity inherent in this solution. The use of two HF radars to determine directional vectors for surface currents is unavoidable and therefore the information required to resolve wind directions is already available. It is this requirement that lead to the development of an accurate geometric system that allows the individual pixels from each station to be assigned geometric coordinates. Each pixel from the first station can then be matched to a corresponding pixel from the second station if they overlap. The

wind direction can then be resolved using the information contained in these, matched, pixels and subsequently placed on a map at the correct position.

This method provides a robust algorithm for wind direction measurement. Utilizing information contained in the first-order spectral lines makes the algorithm very reliable and accurate. It is also computationally simple and is therefore capable of operating in near real-time. The method for finding an accurate value for the spreading function (S), as shown above, could be easily implemented in an automated routine and still be capable of providing near real-time information. Wind direction, in conjunction with the other available products on a real-time basis would be a valuable safety measure for ocean going vessels.

# **Chapter 8: Discussion and Conclusions**

HF radar systems are enjoying growing popularity due to greater acceptance and understanding of the applications it can potentially deliver. With increased scientific awareness of the oceans role in atmospheric processes such as El Nino, and catastrophic events such as the tsunami that struck south-east Asia, demand for improved ocean monitoring systems are rising. The HF radar community feel that this technology can be utilized to fill an important role in expanding global ocean monitoring systems in a combined effort to assist in the forecasting of such events. The work presented in this thesis adds an extra product that has previously been unavailable as a reliable automated monitoring tool. With additions of this nature it is foreseeable that HF radar systems will become an indispensable tool in modern coastal monitoring programs.

The added feature of swell measurement provokes renewed interest from a variety of sources. A diverse range of HF radar users already include coastal defence, navigation and safety, port and harbour operations, dredging support, fishery management, environmental regulation and management, offshore oil and gas exploration, and, drilling and production (Guddal, 1999). Each of these fields could utilize the added information provided by the measurement of swell wave parameters. For coastal management, for example, this information is invaluable in the prediction of coastal response to storm induced wave events (Ruggiero et al., 1997). In a study of beach erosion and recovery, Terwindt et al., (1984) found swell waves to be extremely destructive to coastal areas even when the initiating storm or hurricane does not intersect the coast. This still holds true for common background swell that does not originate from particularly severe storm events. The long duration of swell wave events commonly causes the erosion of coastal foundations and structures. Recent studies (Janssen-Stelder, 2000, Pritchard and Hogg, 2003) found that waves contribute to sediment transport in various ways. They increase the bed shear stresses and therefore the rate at which sediment is suspended into the water column; mixing and transporting of already suspended sediment; and breaking up muddy sea beds so that they flow seawards under gravity as a fluid. The immense energy involved with continuous impacting swell will, over time, be a considerable contributor to a changing coastline.

For the development of more complete sediment transport models, swell wave parameters as measured by an HF radar system, as shown in this thesis, could then be used as an additional parameter to calculate the real impact these waves have on the coastline. Providing the initial direction and height of swell waves when they encounter the seabed would enhance the accuracy of the numerical models being developed in these studies.

#### 8.1 Wave Measurement with HF Radar

A number of ocean monitoring tools already produce wave parameters on a consistent basis. These range from highly advanced technological devices to traditional in-situ single point measuring instruments. Krogstad et al., (1999) lists these to include: synthetic aperture radar (SAR), scatterometers, altimeters, acoustic Doppler current profilers (ADCP), accelerometers, pressure sensors and X-band marine radar. In such a competitive field HF radar is required to prove its potential to secure a place amongst these other systems. However, it does posses a number of advantages over this competition. Satellite based systems offer quality wave information on an extremely large scale however, this type of monitoring is comparatively expensive and coverage can be infrequent (Krogstad and Barstow, 1999). Data on this scale is commonly used for long-term climatic models and does not provide much detail in the coastal regions which is often of most concern. HF Radar is relatively cost effective and provides uninterrupted coverage of the same ocean surface parameters in the coastal zone. ADCPs and Directional Waverider buoys provide accurate wave and current information at a single point. These instruments have proven to be extremely accurate and robust devices that are an excellent source of validation data for HF radar. Being capable of producing maps of surface parameters over much larger areas provides HF radar with a distinct advantage over single point measuring tools.

SAR measurement of waves is still experimental and requires constant validation and calibration. Satellite based radar altimeters measure the range to the sea surface very accurately and then relate the backscatter spread to the roughness of the surface and the significant wave height. Although these methods are proving to provide useful ocean

surface parameters they are very complicated and still subject to development. As an example, it has been found (Essen, 2000) that estimation of wind direction from scatterometer models are adversely affected in the presence of swell. These models account for the wind-sea but not the swell which is, by definition, independent of local wind conditions. The error is caused by the hydrodynamic modulation imposed on the scattering wavelengths by the swell. This is the same effect that is exploited by the algorithm in this thesis to measure the swell parameters. Although scatterometers are not used in coastal regions, HF radar measurements could be used in a supporting role. Swell wave measurements from HF radar could have applications in areas such as calibration and correction for such effects on other instrumentation. The recent improvements in HF radar measurement of ocean waves (Wyatt et al., 1999, Wyatt et al., 2003), including the new swell algorithm, could become an important part of a coastal wave monitoring and forecasting system. In a supporting role to other ocean monitoring devices such as, SAR, scatterometers and altimeters, HF radar data would be utilized in numerical models to provide wave forecasting in the coastal zone (Guddal, 1999, Krogstad and Barstow, 1999).

At present there are three HF radar systems other than COSRAD consistently used to monitor the ocean surface. These include the OSCR (Ocean Surface Current Radar), CODAR (Coastal Radar) and WERA (Wellen Radar) systems. Each system is technically different and possesses strengths in different areas of ocean surface monitoring. They are all capable of mapping surface currents and wind fields from the first-order spectral lines however; the OSCR and WERA systems are better equipped to extract information from the second-order spectrum. The CODAR is a direction finding radar which requires minimal space requirements for installation, however, the downside to this is that it is incapable of providing access to the second-order spectrum (Gurgel *et al.*, 1999). The WERA system was built at the University of Hamburg with specifications capable of a combination of array sizes with both direction finding and beam forming for azimuthal resolution. This system shows a marked increase in performance over older phased array systems like COSRAD and OSCR.

Improved accuracy in HF radar measurements of ocean surface parameters to this point have been mainly due to advances in computational power, monitoring technology and

systems and scientific understanding and numerical methods i.e. modelling and These advancements, particularly in technology and systems, will assimilation. continue to improve in the near future. A good example of these technological advancements is highlighted in a comparison between the older HF COSRAD system and the new WERA system. The signal to noise ratio of the WERA is far superior to that of COSRAD's. This is mainly due to the advancements in technology over the past two decades. The COSRAD system is extremely noisy by today's standards due to the electrical switching mechanisms for the steering of the antenna array. The WERA system has the Bragg peaks positioned up to 90 dB above the noise floor. When using the COSRAD system this difference is only 40 dB. This is not necessarily of importance for parameters extracted from the first-order echo, however, this does become important for the extraction of second-order information. With an improved signal to noise ratio it would be possible to apply the swell algorithm developed in this thesis to greater ranges before the second-order was corrupted by noise. It is likely that the measurements presented in Chapter 6 for swell wave height and direction would noticeably improve running on data with a signal to noise ratio similar to that of the WERA system. This may even include a lower value for  $Hs_{\min}$  than the values found for data collected by the COSRAD system. For low amplitude swell the signal to noise ratio becomes more important because the second-order peaks are weaker and more difficult to identify. With a signal to noise ratio equivalent to a 90 dB range from Bragg peak to noise floor, swell conditions weaker than the minimum of 0.3 m measured in this project may be resolved.

## 8.2 The Automated Swell Wave Algorithm

As a working simplification to the solutions derived by Barrick (1972b), the automated swell algorithm presented here satisfies a long desired objective in remote sensing of the ocean surface by HF radar. The algorithm presents a single-scatter, hydrodynamic solution to overcome the complexities and difficulties associated with the application of double-scatter solutions. Simplifying the method of extraction also improves the speed of the calculation and reduces the demands on hardware. The algorithm has the potential to allow swell wave parameters to be measured in near real-time. It is this aspect of the algorithm that could be particularly useful for permanent radar installations whose primary concern is the safety of shipping. Commercial ports and harbours would find up to date swell information useful for scheduling arrivals and departures, navigation and general safety messages for departing vessels regarding the sea state outside the heads. When used in conjunction with other parameters including surface currents and wind, a clear picture of the ocean surface can be interpreted and potential hazards avoided.

## **8.2.1** Radar Configuration

Compatibility with the radar configuration for surface current data collection is also an important advantage for the algorithm. Although this configuration is not the optimal formation, it is certainly capable of providing reliable information simultaneously with currents and wind parameters. This is demonstrated with the results of swell height and direction in this thesis. The radar configuration is entirely dependent upon the objectives of the deployment. If the full assemblage of ocean surface parameters is required then a dual deployment of orthogonally facing radars is the best solution. However, if the only concern is for swell monitoring then the optimal configuration is a deployment of three radars positioned adjacently so that the ocean surface coverage is 180 degrees. Of course this relies on the ability to secure a suitable area to position three antenna arrays. In the majority of cases a coverage angle of 180 degrees ensures that swell waves approaching from all possible directions can be measured. With this configuration, loss of information in areas where swell waves intersect the radar beams orthogonally is no longer a concern. It may be a desirable option for permanent

installations as discussed above. For a permanent installation that is concerned mainly with swell wave conditions, as in the Bass Strait area, this three system configuration would provide good coverage and very little ongoing cost after the initial purchase.

A three radar adjacent installation however, may not be feasible for many locations due to the large space requirements for three adjacent arrays. It is also less economical than a dual overlapping configuration in terms of the number of ocean surface parameters that are extracted. However, should there be a requirement for uninterrupted swell measurement then this system would fulfil that objective with very little ongoing cost to the user.

Employing this configuration at Bass Strait to monitor swell activity impacting shipping traffic passing through Port Phillip Heads would result in a coverage map as shown in Figure 61. In this case the Portsea station was chosen as the base site for the new configuration. It is clear in this case that there is a large portion of the south easterly facing station that is not directed out to sea due to the curved geography of the entrance to Port Phillip Bay. It may be possible at this location to achieve adequate coverage with just two adjacent radar systems. Three radar system positioned at Kingscliff in Tweed Heads provides excellent ocean coverage (Figure 62). Swell approaching from any direction would be captured by at least one of the radars and can be validated by the Waverider buoy in the vicinity.

#### 8.2.2 Limitations

It was found earlier that the limitations of the algorithm are directly related to the ability of the algorithm to consistently identify the swell peaks in the Doppler spectrum. Circumstances that cause the algorithm to fail to do this include very low swell heights, swell heights that exceed the saturation limit (>3.16 m), bimodal swell, poor signal to noise ratio at long ranges and near orthogonal angles of incidence between the radar beam and the swell. Some of these limitations were reached when analysing the data collected during the two deployments at Tweed Heads and Bass Strait.

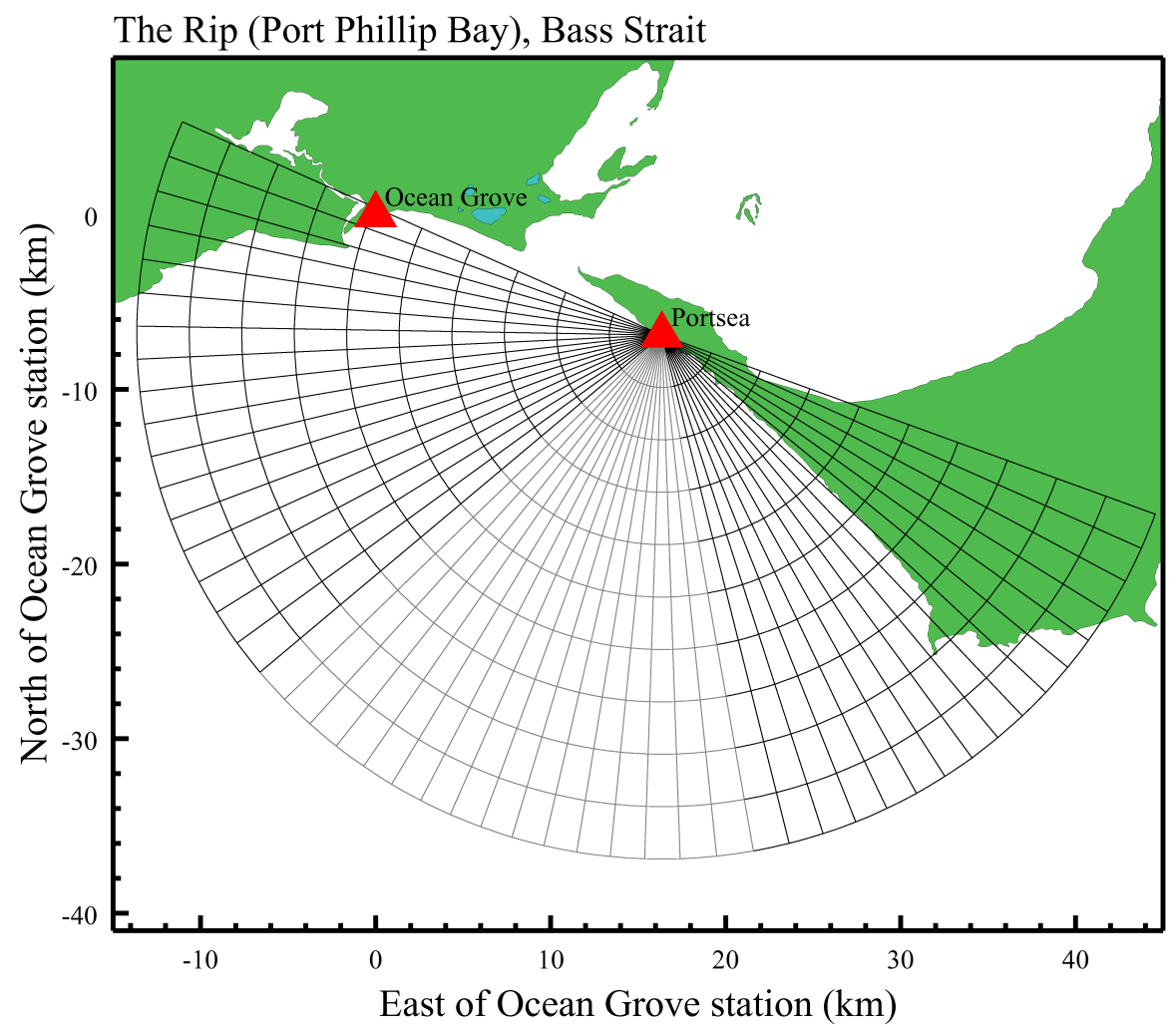
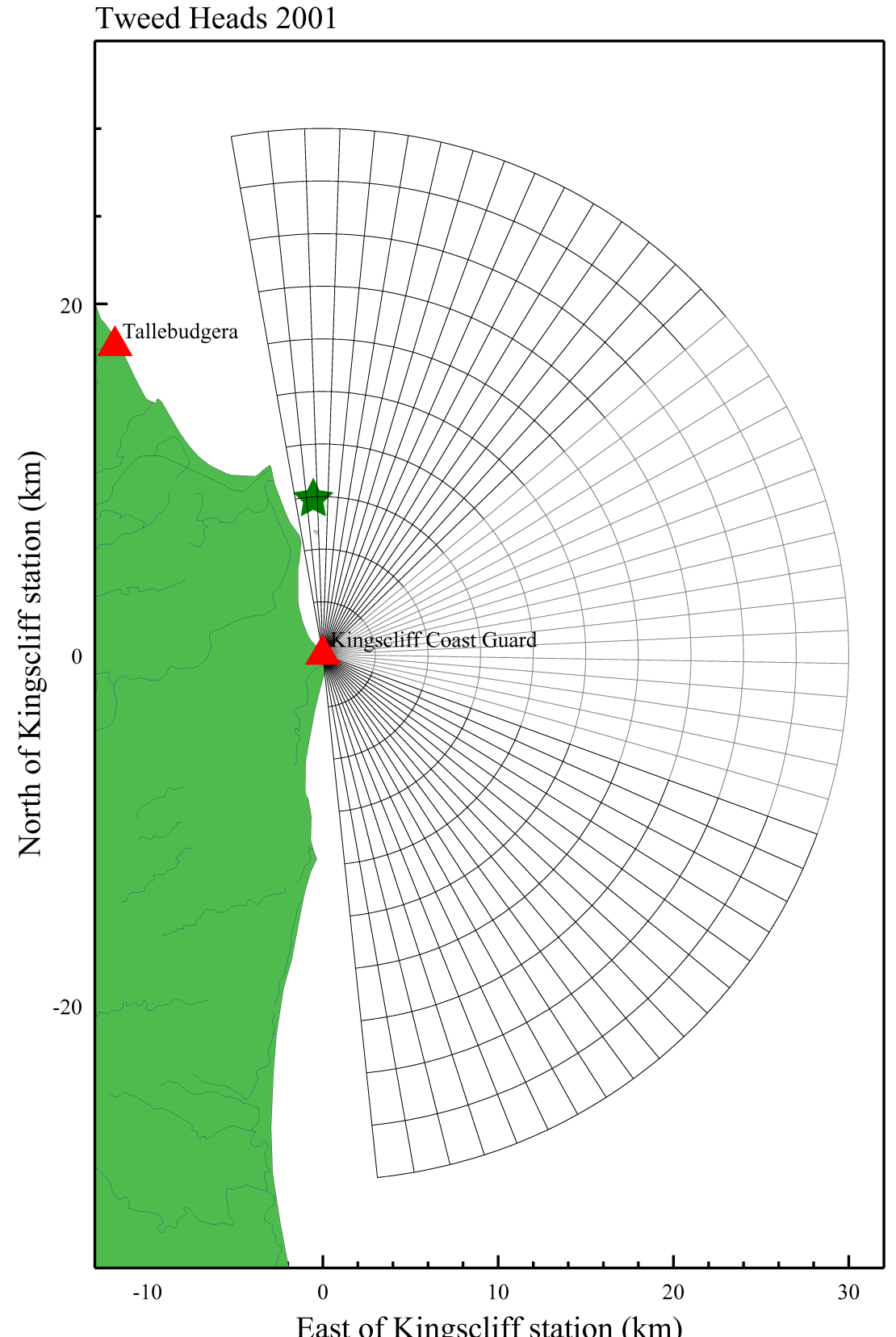


Figure 61: The optimal radar configuration for the extraction of swell parameters at Port Phillip Heads using the algorithm developed in this thesis. This consists of 3 radars positioned adjacently each consisting of a 60 degree sweep. A full 180 degrees is then covered to enable swell measurement from any direction.



East of Kingscliff station (km)
Figure 62: Optimal radar configuration for swell wave measurement at
Tweed Heads. The radar coverage here will ensure swell arriving from
nearly all directions can be measure using the swell algorithm.

The limitation encountered in weak swell conditions was evaluated ( $Hs_{min}$ ) individually for both deployments. This value was minimized for the analysis of the Bass Strait data to be 0.3 m. Swell levels of this magnitude are generally inconsequential for most interests as it is the strong swell waves that cause most concern. However, it is important that the algorithm is capable of recognising this and responding accordingly to swell levels that fall below the lowest measurable height. At present the algorithm does this by calculating an error value that reflects the condition of the second-order spectrum and the confidence in result. In the meantime the system would continue to measure surface currents, wind and rms wave heights. When the swell is below the  $Hs_{min}$  value, a result stating that the swell is less than 0.3 m is sufficient for most applications of the data. This is also true at the opposite end of the scale if the spectrum should saturate due to swell heights in excess of  $h_{sat}$  (3.18 m). An automated algorithm would be capable of issuing a warning of caution that states that the swell has reached levels greater than 3 m. This again is often sufficient for many applications of the algorithm.

Bimodal seas will also cause deterioration in accuracy due to bifurcations or broadening of the second-order peaks. Multiple swells with similar amplitudes but different propagation directions will result in swell peaks with slight variations in frequency that cannot be consistently resolved with this algorithm. It may be possible to develop a more sophisticated peak selection routine that can reliably detect multiple swell peaks due to bimodality in the future. At present the algorithm is measuring the dominant swell wave on the ocean surface at that particular point in time.

In the studies at Tweed Heads and Bass Strait, reliable swell measurements were being collected up to the final bracket of incoherently averaged pixels. This gives the algorithm an effective working range of 30 km. As mentioned earlier, this range may be increased if the algorithm were to be applied to data collected by a radar system with a superior signal to noise ratio. With an improved signal to noise ratio the level of incoherent averaging may be reduced allowing a better spatial or temporal resolution and for swell parameters to be calculated to greater ranges.

#### 8.3 Future Work

Further work in the development of swell wave measurement by HF radar involves the testing of the algorithm on data collected by more advanced radar systems. This should result in improved accuracy for the reasons addressed above, mainly superior signal to noise ratios, and prove the algorithm as an adaptable tool for ocean surface mapping. The algorithm was created using Matlab<sup>®</sup> 6.1 which is a widely used and extremely flexible programming platform that would allow for relatively simple adaptation to the various systems in use today.

Another area for future interest and advancement of radio oceanography involves the ability to directly compare or merge HF radar data with other various remote sensing tools. The ability of HF radar users to integrate the data with that from other sources has been recognised as an important area of research and work on developing methods to merge data from various sources has been carried out by Krogstad *et al.*, (1999). These initial studies attempted to merge HF radar data from OSCR and WERA systems, with Directional Waverider buoys. They cite the major problems with merging data from various ocean monitoring sources as:

- Difference in measurement principles
- Systematic off-sets due to calibration differences
- Sampling variabilities
- Temporal and/or spatial off-sets

These issues do not only apply to comparisons with wave buoy data but also satellite based remote sensing systems. Continued work in this area will see these issues resolved and the increased use of HF radar as an ocean surface monitoring device.

Additional technical improvements that can be made to the algorithm include bimodal swell wave detection and shallow water swell measurement. Both of these additions present challenges in various ways. The algorithm presented here calculates parameters for the dominant swell wave at any point in time. The problem of bimodal wave detection lies in the reliability of automating an algorithm to consistently decipher

between two second-order peaks that are very close in frequency due to two independent swell waves. It is also important that the algorithm does not mistake peaks in the second-order due to noise as a bimodal swell. Development of sophisticated peak selection routines requires data in which the user is aware of a bimodal swell situation in order to become familiar with the manifestation of bimodal swell in the Doppler spectrum.

Shallow water considerations have proven to be challenging in many oceanographical applications including HF radar (Holden and Wyatt, 1992). Most ranges achieved by HF radar systems can safely assume deep water conditions, however, measurements from near shore pixels of long ocean wave parameters such as swell may interact with the seafloor. For applications such as coastal engineering, wave parameters as they impact the coast are useful and therefore shallow water effects need consideration. For example, swell waves with a period of 14 seconds are 300 m long and will begin to feel the ocean floor when the water depth is less than ½ of the wavelength. Therefore, allowances for shallow water conditions must begin at 75 m water depth. In many locations this depth may be quite a distance from shore.

## 8.4 Conclusions

The main achievements presented in this thesis are:

- 1. Development of a routine algorithm for spectral processing of HF radar Doppler spectra. This includes the removal of the Doppler shift due to surface currents, power level normalization and incoherent averaging of spectra both spatially and temporally.
- Development of a new swell wave parameter extraction method from HF radar spectra after the application of existing second-order solutions for long ocean wave measurement (Barrick, 1972b) proved too sensitive to minor variations in second-order features to be useful.

- 3. The new method is a simplified single-scatter technique that provides a good approximation of the hydrodynamic interaction between swell waves and the Bragg waves that are resonant with the transmitted radar wave. Through a numerical model it was shown that the electromagnetic component (Equation 7) of the coupling coefficient (Equation 9) could be effectively removed by calculating the mean swell peak power. This method produces results equivalent to measurements made utilizing the hydrodynamic interaction only.
- 4. Accurate measurement of swell height to within ±0.1 m for waves greater than 0.3 m in height.
- 5. Measurement of mean swell wave propagation direction to within  $\pm 10$  degrees for waves greater than 0.3 m in height.
- Measurement of mean swell wave period to within ±1 second by taking into account the frequency displacement of all available swell peaks from the first-order line.
- 7. Capable of making all measurements in near real-time from data collected by a single HF radar station.
- 8. Alternate method of resolving the ambiguity inherent in the calculation of wind direction. This method requires data from two orthogonally facing radars, as is the case with surface currents, and is also capable of near real-time operation.

This unique algorithm for the extraction of swell wave parameters from HF radar spectra is capable of providing information with accuracies that would be useful for many operational coastal monitoring programs. Increasing the capabilities of HF radar systems with algorithms such as this provides consumers with additional reasons to consider HF radar as a contender to replace traditional monitoring tools for currents, wind and wave measurement.

# References

Anderson, D. J., I. L. Turner, A. Dyson, S. Lawson, and S. Victory, 2003: Tweed River Entrance Sand Bypassing Project: 'Real Time' Beach Monitoring and Analysis System via the World-Wide-Web. *Proceedings*, 16th Australasian Coastal and Ocean Engineering Conference ('Coasts and Ports 2003'), 2.

Barnum, J. R., 1971: Private correspondence.

Barrick, D. E., 1971: Theory of HF and VHF propagation across the rough sea, 1, The effective surface impedance for a slightly rough highly conducting medium at grazing incidence. *Radio Science*, **6**, 517-526.

Barrick, D. E., 1972a: First-order theory and analysis of MF/HF/VHF scatter from the sea. *IEEE Transactions on Antennas and Propagation*. **AP-20**, 2-10.

Barrick, D. E., 1972b, Remote sensing of sea state by radar, in *Remote Sensing of the Troposphere*, edited by V. E. Derr, 12-1 – 12-46, NOAA/Environmental Research Laboratories, Boulder, Colorado. US Government Printing Office, Washington, D. C.

Barrick, D. E., 1977: Extraction of wave parameters from measured HF radar sea-echo Doppler spectra. *Radio Science*, **12**, 415-424.

Barrick, D. E., 1980, Accuracy of parameter extraction from sample-averaged sea-echo Doppler spectra. *IEEE Transactions on Antennas and Propagation*. **AP-28**, 1-10.

Bureau of Meteorology, 1991. Observing the weather: The Australian co-operative observers guide. *AusInfo* cat. no. 987 3272 1

Bureau of Meteorology, 2001: Monthly Weather Review (February, 2001)

Bureau of Meteorology, 2001: Monthly Weather Review (March, 2001)

Bureau of Meteorology, 2001: Monthly Weather Review (July, 2001)

Callaghan, D. P. and P. Nielson, 2003: Morphological Modelling of the Tweed River Tidal Entrance. *Proceedings, 16th Australasian Coastal and Ocean Engineering Conference ('Coasts and Ports 2003')*, **No. 22**.

Crombie, D. D., 1955: Doppler spectrum of sea echo at 13.56Mc/s. *Nature*, **175**, 681-682.

Dyson, A., S. Victory, and T. Connor, 2001: Sand Bypassing the Tweed River Entrance: An Overview. *Proceedings, 15th Australasian Coastal and Ocean Engineering Conference ('Coasts and Ports 2001')*, 310-315.

Essen, H. H., 2000, Theoretical investigation on the impact of long surface waves on empirical ERS-1/2 scatterometer models, *International Journal of Remote Sensing*, **21**, 1633-1656.

Falconer, R. L. and D. J. Linforth, 1972, Winds and waves in Bass Strait, Meteorological Summary, Bureau of Meteorology – Department of the Interior, April 1972.

Fernandez, D. M., H. C. Graber, J. D. Paduan and D. E. Barrick, 1997: Mapping wind direction with HF radar, *Oceanography*, **10**, 93-95.

Georges, T. M., J. W. Maresca, C. T. Carlson, J. P. Riley, R. M. Jones, and D. E. Westover, 1981: Recovering ocean waveheight form HF radar sea echoes distorted by imperfect ionospheric reflection. *NOAA Technical Memorandum* ERL WPL-73.

Guddal, J., 1999: Application of wave spectral information in marine forecasting. *Coastal Engineering*, **37**, 369-377.

Gurgel, K. W., H. H. Essen, and S. P. Kingsley, 1999: High-frequency radars: physical limitations and recent developments. *Coastal Engineering*, **37**, 201-218.

Gurgel, K. W., G. Antonischki, H. H. Essen, and T. Schlick, 1999: Wellen Radar (WERA): a new ground-wave HF radar for ocean remote sensing. *Coastal Engineering*, **37**, 219-234.

Gush, J. 2003, Crossing Bass Strait, Ocean Navigator Magazine, 130.

Harris, G. P. and C. J. Crossland, 1999: Introduction to the Port Phillip Bay Environmental Study. *Marine and Freshwater Research*, **50**, iii-iv.

Hasselmann, K. 1971: Determination of ocean-wave spectra from Doppler radio return from the sea surface. *Nature Physical Science*, **229**, 16-17.

Heron, M. L., P. E. Dexter, and B. T. McGann, 1985: Parameters of the air-sea interface by high-frequency ground-wave Doppler radar. *Australian Journal of Marine Freshwater Research*, **36**, 655-670.

Heron, M. L. and R. J. Rose, 1986: On the application of HF ocean radar to the observation of temporal and spatial changes in wind direction. *IEEE Journal of Oceanic Engineering*, **OE-11**, 210-218.

Heron, M. L. and S. F. Heron, 2001: Cumulative probability noise analysis in geophysical spectral records, *International Journal of Remote Sensing*, **22**, 2537-2544.

Heron, M. L. and A. Prytz, 2002: Wave height and wind direction from the HF coastal ocean surface radar. *Canadian Journal of Remote Sensing*, **28**, 385-393.

Heron, M. L., 2005: The role of HF ocean surface radar in Australia as a long-term coastal ocean monitoring facility, *Australasian Coastal and Ocean Engineering Conference (Coasts and Ports 2005)*. (In review)

Hisaki, Y., 1999: Correction of amplitudes of Bragg lines in the sea echo Doppler spectrum of an ocean radar. *Journal of Atmospheric and Oceanic Technology*, **16**, 1416-1433.

Holden G. J. and L. R. Wyatt, 1992: The extraction of sea-state in shallow water using HF radar, *IEE Proceedings Part F*, **139**, 175-181.

Huang, W., E. Gill, S. Wu, B. Wen, Z. Yang, and J. Hou, 2003: Measuring surface wind direction by monostatic HF ground-wave radar at the Eastern China Sea. *IEEE Journal of Oceanic Engineering*, **29**, 1032-1037.

Janssen-Stelder, B., 2000: The effect of different hydrodynamic conditions on the morphodynamics of a tidal mud flat in the Dutch Wadden Sea. *Continental Self Research*, **20**, 1461-1478.

Kinsman, B., 1965: Wind Waves, Prentice-Hall, Englewood Cliffs, N. J.

Krogstad, H. E. and S. F. Barstow, 1999: Satellite wave measurements for coastal engineering applications. *Coastal Engineering*, **37**, 283-307.

Krogstad, H. E., J. Wolf, S. P. Thompson, and L. R. Wyatt, 1999: Methods for Intercomparison of Wave Measurements. *Coastal Engineering*, **37**, 235-257

Lipa, B. J., 1978, Inversion of second-order radar echoes from the sea. *Journal of Geophysical Research*, **83**, 959-962.

Lipa, B. J. and D. E. Barrick, 1980, Methods for the extraction of long-period ocean-wave parameters from narrow-beam HF radar sea echo, *Radio Sci.*, vol. **15**, pp. 843-853.

Lipa, B. J. and B. Nyden, In Press: Directional Wave Information from the SeaSonde. IEEE Journal of Oceanic Engineering.

Lipa, B. J., D. E. Barrick, and J. W. Maresca, 1981: HF radar measurements of long ocean waves. *Journal of Geophysical Research*, **86**, 4089-4102.

Lipa, B. J. and D. E. Barrick, 1986, Extraction of sea state from HF radar sea echo: Mathematical theory and modelling. *Radio Science*, Volume **21**, No. 1, 81-100.

Long, A. E., and D. B. Trizna, 1973, Mapping of North Atlantic winds by HF radar backscatter interpretation, *IEEE Transactions on Antennas and Propagaion*, **AP-21**, 680-685.

Longuet-Higgins, M. S., D. E. Cartwright, and N. D. Smith, 1963: Observations of the directional spectrum of sea waves using the motion of a floatation buoy. *Proceedings of the Conference on Ocean Wave Spectra, Prentice-Hall Inc., Englewood Cliffs, N.J.*, 111-136.

Oltman-Shay, J. and K. K. Hathaway, 1989: Infragravity energy and its implications in nearshore sediment transport and sandbar dynamics. *Technical Report CERC-TR-89-8*.

Phillips, O. M., 1977: Dynamics of the upper ocean. 2nd ed. Cambridge University Press.

Pierson, W. J. Jr, and L. Moskowitz, 1964. A proposed spectral form for fully developed wind seas based on a similarity method of S. A. Kitaigordskii. *Journal of Geophysical Research*, **69**, 5181-5190.

Prandle, D. and L. R. Wyatt, 1999: Editorial: Introduction to this special issue. *Coastal Engineering*, **37**, 193-199.

Pritchard, D. and A. J. Hogg, 2003: On fine sediment transport by long waves in the swash zone of a plane beach. *Journal of Fluid Mechanics*, **493**, 255-275.

Provis, D. G., 2004: At the Planning Panel Inquiry: In the matter of the channel deepening project environment effects statement. *Port of Melbourne Corporation Report* No. RM2085/J5372.

Prytz, A. and M. L. Heron, 1999: On the flushing of Port Phillip Bay: an application of HF ocean radar. *Marine and Freshwater Research*, **50**, 483-492.

Prytz, A. and M. L. Heron, 1995: HF radar measurements of surface currents in southern Port Phillip Bay. CSIRO Institute for Natural Resources and Environment - Port Phillip Bay Environmental Study. iii, 18 pp.

Ruggiero, P., G. M. Kaminsky, P. D. Komar, and W. G. McDougal, 1997: Extreme waves and coastal erosion in the Pacific Northwest. *Ocean Wave Measurement and Analysis, Proceedings of the 3<sup>rd</sup> International Symposium, Waves '97*, 947-961.

Sevgi, L., A. Ponsford, and H. C. Chan, 2001: An integrated maritime surveillance system based on High-Frequency surface-wave radars, Part 1: Theoretical background and numerical simulations. *IEEE Antennas and Propagation Magazine*, **43**, 28-43.

Spillane, K. T., R. L. Falconer and D. S. Wright, 1972: Deep water waves and swell state in Bass Strait. *Bureau of Meteorology, Department of the Interior – Meteorological Summary* 

Stewart, R. H., 1971: Higher order scattering of radio waves from the sea. *IEEE G-AP International Symposium Digest*, 190-193

Stewart, R. H. and J. W. Joy, 1974: HF radio measurements of surface currents. *Deep Sea Research*, **21**, 1039-1049.

Stewart, D. J and J. R. Barnum, 1975: Radio measurements of oceanic winds at long ranges: An evaluation. *Radio Science*, **10**, 853-857.

Terwindt, J. H. J., C. H. Hulsbergen, and L. H. M. Kohsiek, 1984: Structures in deposits from beach recovery, after erosion by swell waves around the southwestern coast of Aruba (Netherlands Antilles). *Marine Geology*, **60**, 283-311.

van der Molen, W., H. Ligteringen, J. C. van der Lem, and J. C. M. de Waal, 2003: Behaviour of a Moored LNG Ship in Swell Waves. *Journal of Waterway, Port, Coastal and Ocean Engineering*, **129**, 15-21.

Wait, J. R., 1966: Theory of HF ground wave backscatter from sea waves. *Journal of Geophysical Research*, **71**, 4839-4842.

Wyatt, L. C., S. P. Thompson and R. R. Burton, 1999: Evaluation of HF radar wave measurements. *Coastal Engineering*, **37**, 259-282.

Wyatt, L. R., J. J. Green, K -W. Gurgel, J. C. Nieto Borge, K. Reichert, K. Hessner, H. Günther, W. Rosenthal, O. Saetra and M. Reistad, 2003: Validation and intercomparisons of of wave measurements and models during the EuroROSE experiments. *Coastal Engineering*, **48**, 1-28.